

DYNAMIC TRANSPORT MEASUREMENTS
OF VO₂ THIN FILMS THROUGH
THE METAL-TO-INSULATOR
TRANSITION

by

JOSHUA MICHAEL JONES

PATRICK LECLAIR, COMMITTEE CHAIR
ARUNAVA GUPTA
TIM MEWES
CLAUDIA MEWES
DEAN TOWNSLEY

A DISSERTATION

Submitted in partial fulfillment of the requirements
for the degree of Doctor of Philosophy
in the Department of Physics and Astronomy
in the Graduate School of
The University of Alabama

TUSCALOOSA, ALABAMA

2018

ABSTRACT

VO₂ is a transition metal oxide material well known for its high magnitude metal-to-insulator transition (MIT) with a corresponding change in crystal structure [1]. At room temperature, VO₂ is found in an insulating monoclinic phase (P2₁/c) that upon heating through the transition temperature (T_c, ~341 K in bulk material) changes to a metallic rutile phase (P4₂/mnm) [2]. The MIT can be activated thermally by heating or cooling through T_c, but has also been shown to be sensitive to electric field [3], infrared radiation [4], pressure [5], and strain [6]. The value of T_c is also highly tunable through doping [7] and growth of strained epitaxial thin films [8]. The massive 3-4 order of magnitude change in electrical resistivity (ρ) has drawn interest for possible device level applications. The transition is characterized by the coexistence of rutile metallic domains and a monoclinic insulating matrix that results in a smooth progression of the DC transport and dielectric properties as the MIT is induced.

In this thesis, we present an overview of three novel transport experiments all of which involve epitaxial TiO₂/VO₂ films grown in a home-built low-pressure chemical vapor deposition system. The first experiment looks at the time evolution of the film resistance and capacitance as it settles for an extended period very near T_c. We report evidence that this settling process is characterized by at least two underlying relaxation processes.

The second experiment involves the deposition and ferromagnetic resonance (FMR) characterization of TiO₂/VO₂/Ru/Py heterostructures. Our analysis indicates enhanced spin pumping into the VO₂ layer when in the metallic state that is associated with an increase in the effective Gilbert damping parameter.

Finally, we discuss the results of $1/f$ noise spectroscopy measurements collected on Hall-bar patterned $\text{VO}_2(100)$ films. We show that the processes governing noise along both crystallographic axes are identical and, in the metallic rutile state, follows a unique R^{-3} scaling behavior.

DEDICATION

For Liz,

As this could not have been written without you.

LIST OF ABBEVIATIONS AND SYMBOLS

(100)	A TiO ₂ substrate with the (100) crystal plane on the surface
(001)	A TiO ₂ substrate with the (001) crystal plane on the surface
(110)	A TiO ₂ substrate with the (110) crystal plane on the surface
2θ	Angle between incident and diffracted waves in an X-ray measurement
a.u.	Arbitrary units
a_r	The rutile a-axis, a crystallographic direction in the TiO ₂ crystal
AC	Alternating current
AFM	Atomic Force Microscope (Microscopy)
α	Gilbert damping parameter in magnetic relaxation
β	Back reflection parameter in spin pumping
C	Capacitance
c_r	The rutile c-axis, a crystallographic direction in the TiO ₂ crystal
CPW	Co-planar waveguide
CVD	Chemical vapor deposition
DAQ	Data acquisition
DC	Direct current
ΔH	FMR linewidth
ΔH_0	Inhomogenous linewidth
DUT	Device under test
f	frequency (Hz)
f_c	Cutoff frequency

FM	Ferromagnetic
FMR	Ferromagnetic resonance
FWHM	Full width half max
γ	Gyromagnetic ratio
I	Current
IR	Infrared
K	1/f noise factor
λ	Wavelength
λ_{SD}	Spin diffusion length
M_s	Saturation magnetization
M_{eff}	Effective magnetization
MIT	Metal-to-insulator transition
Ω	Ohms, the unit of resistance
ω	In X-ray measurements, the angle between the incident beam and the substrate tangent vector
ω	In impedance measurements, the angular frequency (rads)
ρ	Electrical resistivity
PCI	Peripheral Component Interconnect, a computer bus standard for attaching hardware like data acquisition cards
PID	Proportional Integral Derivative
PPMS	Physical Property Measurements System
PSD	Power spectral density
PV	Process variable
Py	Permalloy ($Ni_{80}Fe_{20}$)
R	Resistance
RF	Radio frequency

rms	Root mean square
sccm	Standard cubic centimeters per minute
σ	Electrical conductivity
SP	Setpoint variable
t	Thickness
T	Temperature
T_c	Transition temperature
T_p	Precursor temperature
T_s	Substrate temperature
τ	Exponential decay time constant
USB	Universal serial bus
UV	Ultraviolet
V	Voltage
X	Reactance
XRD	X-ray diffraction
XRR	X-ray reflectivity
Z	Impedance

ACKNOWLEDGEMENTS

Firstly, to my advisor, Patrick LeClair, I thank you for your many years of guidance and teaching. I have learned more from you in the past 8 years than I can possibly mention here. You were the person who first suggested this field to me, and for that I will be forever grateful.

To my committee members:

Arun Gupta who has advised me on CVD and VO_2 characterization,

Tim Mewes who introduced me to LabView and FMR measurements,

Claudia Mewes who instructed me on condensed matter theory,

Dean Townsley who helped me navigate the jungles of the graduate school and provided many interesting discussions,

I thank all of you for your time and willingness to pass on your knowledge to me.

To my friends, colleagues, and instructors throughout my many years in Tuscaloosa, I could not have completed these projects without your network of support and care, and I give my deepest gratitude.

To my parents and family in Birmingham, for always having an open door for me, I love you all greatly.

And to Liz, for believing in me at every step and sticking with me to the end, your love and kindness has kept me sane through this process.

CONTENTS

ABSTRACT.....	ii
DEDICATION.....	iv
LIST OF ABBEVIATIONS AND SYMBOLS.....	v
ACKNOWLEDGEMENTS.....	viii
LIST OF TABLES.....	xii
LIST OF FIGURES.....	xiii
CHAPTER 1: INTRODUCTION.....	1
CHAPTER 2: DEVICE FABRICATION AND CHARACTERIZATION TECHNIQUES.....	7
2.1. Introduction.....	7
2.2. Film Preparation and Patterning Techniques.....	8
2.2.1. LPCVD.....	8
2.2.2. RASCAL Magnetron Sputtering System.....	11
2.2.3. Photolithography and Hall Bar Preparation.....	13
2.3. Low-Overshoot Temperature Controller.....	18
2.4. Device Quality Characterization.....	22
2.4.1. X-Ray Techniques.....	22
2.4.2. Atomic Force Microscopy.....	23
2.4.3. Resistivity Measurements.....	24
CHAPTER 3: SUMMARY OF STRUCTURAL AND TRANSPORT CHARACTERIZATION.....	28

3.1. X-ray Diffractometry and Resistance Results.....	29
3.2. AFM Topology and Roughness Optimization.....	34
CHAPTER 4: LONG TIMESCALE RELAXATION OF VO ₂ THIN FILMS ANALYZED WITH IMPEDANCE SPECTROSCOPY	39
4.1. Impedance Spectroscopy	41
4.2. Impedance Model for VO ₂ (001) Thin Films	43
4.3. Measurement System and Error Estimation	46
4.4. Methodology	49
4.5. Impedance Analysis of VO ₂ (001).....	52
4.6. Discussion	62
CHAPTER 5: HIGH TEMPERATURE FERROMAGNETIC RESONANCE STUDIES OF VO ₂ (110)/NI ₈₀ FE ₂₀ HETEROSTRUCTURES	65
5.1. FMR Technique	66
5.2. Spin Pumping.....	68
5.3. FMR System Description.....	70
5.4. Sample Preparation and Methodology.....	72
5.5. Analysis.....	73
5.6. Summary	82
CHAPTER 6: LOW FREQUENCY NOISE SPECTROSCOPY OF THE METAL-TO-INSULATOR TRANSITION OF PATTERNED VO ₂ THIN FILMS	83
6.1. System Description	84
6.2. Methodology	87
6.3. Analysis Method of 1/f Noise Parameters	88
6.4. Noise Factors and Scaling.....	89
CHAPTER 7: SUMMARY.....	95

REFERENCES	97
APPENDIX.....	105

LIST OF TABLES

Table 3.1: The a_r and c_r lattice constants extracted from XRD measurements, along with the associated strain due to lattice mismatch from TiO_2	31
Table 3.2: Summary of DC resistance measurements	34

LIST OF FIGURES

1.1: a) The crystal structure of VO ₂ in the high temperature, rutile metallic (P4 ₂ /mnm) phase. b) The corresponding rutile band plot. c) The crystal structure of low temperature, monoclinic (M1) insulating phase. d) The corresponding band plot showing a 0.6 eV charge gap associated with the V-V dimerization	2
1.2: s-SNIM imaging of bulk VO ₂ at temperatures very near T _c	3
1.3: a) LEED and b) XPEEM imaging of the MIT in epitaxially strained VO ₂ films grown on TiO ₂ substrates	4
2.1: The home-built LPCVD system with components labeled.	9
2.2: The vacuum schematics of the in-house RASCAL magnetron sputtering system.	12
2.3: An external image of the RASCAL magnetron sputtering system.....	12
2.4: The standard photolithographic patterning procedure.	15
2.5: The internal schematics of an ion milling system.....	16
2.6: Hall bar patterns on a TiO ₂ /VO ₂ (110) film.....	17
2.7: The final version of the software control scheme utilized in our low-overshoot temperature controller.....	20
2.8: a) The time dependent temperature profile of a calibration sample when controlled with a typical PID feedback loop. b) Temperature settling profiles implemented with the heater model assisted PID controller	20
2.9: The custom designed sample holder showing a mounted Hall bar patterned VO ₂ sample ...	21
2.10: The standard X-ray diffractometer configuration	22
2.11: Working principles of an AFM measurement tool	24
2.12: A sample bonding diagram for a 4-point probe measurement in the Van der Pauw configuration.	26
2.13: 4-point probe configuration for Hall bar patterned thin films.	27
3.1: Results of θ -2 θ and rocking curve measurements for VO ₂ (100), (110), and (001) films.....	30

3.2: The system geometry utilized during a ϕ scan, where the sample stage is rotated about its normal while probing an off-axis plane family.....	31
3.3: ϕ scan results show a clear two-fold symmetry in VO ₂ matching that of the substrate peaks indicating high quality epitaxy.....	32
3.4: Reciprocal space mapping of the off-axis (301) peak in a VO ₂ (100) film	32
3.5: Temperature dependent 4-point resistance measurements	33
3.6: 12 nm (001) oriented film exhibiting microcracking features.....	35
3.7: An 80 nm (001) oriented film.....	36
3.8: 13 nm (110) film with 1.6 nm rms roughness.....	37
3.9: 11 nm (110) film with 0.48 nm rms roughness.....	38
4.1: The basic characteristics of an AC impedance measurement.....	42
4.2: A representation of impedance on the complex plane.....	43
4.3: A simulated impedance spectrum for an example parallel RC circuit ($R = 1\text{ M}\Omega$ and $C = 1\text{ pF}$) of similar component values to a VO ₂ thin film.....	46
4.4: The sensitivity profile of the HP4284A LCR meter	48
4.5: The equivalent circuit model of the system and cabling contribution to the impedance response	50
4.6: A Bode plot of several impedance spectrums taken before, during, and after the MIT	52
4.7: Nyquist plots of the same measurements.....	53
4.8: Fitted DC resistance drift plotted as a function of the settling time.	54
4.9: Resistance drift magnitude (at 2.5 hrs) plotted vs settling temperature.....	55
4.10: Temperature dependence of the fitted values of C	56
4.11: The time dependence of the normalized resistance for several temperatures.....	57
4.12: Time dependent resistance for the 337 K settling temperature fit with single and double exponential decay functions.....	58
4.13: Extracted capacitances of the 335 K settling temperature overlaid with the fitting error margins for measurement accuracy.	59
4.14: The same C data overlaid with the estimated fit precision	60

4.15: Time dependent capacitance of the 323 K settling temperature measurement fit to a single exponential decay function.	61
4.16: The fitted values for the R and C decay time constants for all settling temperatures.	62
5.1: A schematic of a spin pumping experiment, where the precession of the FM layer injects spin polarized current into neighboring metallic layers.....	68
5.2: The components and basic design of the FMR system.....	71
5.3: Temperature dependent resistance of Py(6)/Ru(2.3)/VO ₂ through the MIT	74
5.4: Raw resonance curves from the series A sample.....	75
5.5: Series A effective damping parameters above and below the MIT	75
5.6: Series B, 4 nm effective damping parameters	77
5.7: Series B, 6 nm effective damping parameters	78
5.8: Series B, 20 nm effective damping parameters	78
5.9: Bulk damping parameters in Py exhibit a nearly linear dependence on temperature approaching room temperature	79
5.10: Series C, 6 nm effective damping parameters	80
5.11: Series C, 20 nm effective damping parameters	81
5.12: A summary of the damping results from series B and C	81
6.1: The hardware components of the home-built 1/f noise spectroscopy system.	85
6.2: Modifications made to the controller computer to limit noise contributed by the internal switched-mode power supply	87
6.3: Raw output data from the noise spectroscopy system in the full frequency measurement range.	90
6.4: Processed 1/f noise profiles for a wide range of measurement temperatures	90
6.5: The temperature dependence of the noise factor for (001), (100), and (110) films.....	91
6.6: R(T) data for patterned (100) VO ₂ exhibits a clear transport anisotropy, with the T _c of the c _r axis shifted to higher temperature in both heating and cooling cycles.	92
6.7: The ratio of log(K/R) shows nearly identical values in the metallic and insulating states for both axes	93

CHAPTER 1: INTRODUCTION

VO_2 is a transition metal oxide material well known for its high magnitude metal-to-insulator transition (MIT) with a corresponding change in crystal structure [1]. At room temperature, VO_2 is found in an insulating monoclinic phase ($\text{P}2_1/c$) that upon heating through the transition temperature (T_c , which is 341 K in bulk material) changes to a metallic rutile phase ($\text{P}4_2/mnm$) (Figure 1.1) [2]. The room temperature monoclinic phase is associated with V-V dimers tilted along the rutile (110) orientation. [9] The dimerization results in a splitting of the d_{\parallel} band into filled bonding and anti-bonding states and a concurrent upward shift in the π^* bands above the Fermi level, resulting in a 0.6 eV band gap. [10] The transition to the rutile crystal structure is associated with the breaking of the V-V dimers and a corresponding closing of the gap as the π^* and d_{\parallel} bands overlap at the Fermi level.

The MIT can be activated thermally by heating or cooling through T_c , but has also been shown to be sensitive to electric field [3], infrared radiation [4], pressure [5], and strain [6]. The value of T_c is also highly tunable through doping [7] and growth of strained epitaxial thin films [8]. The massive 3-4 order of magnitude change in electrical resistivity (ρ) has drawn interest for possible device level applications such as memristors [11], field effect transistors (FET) [4], and strain sensors [6] and has already found use in on-the-market products like bolometers [12](seen in smartphone based IR cameras) and energy efficient window coatings [13].

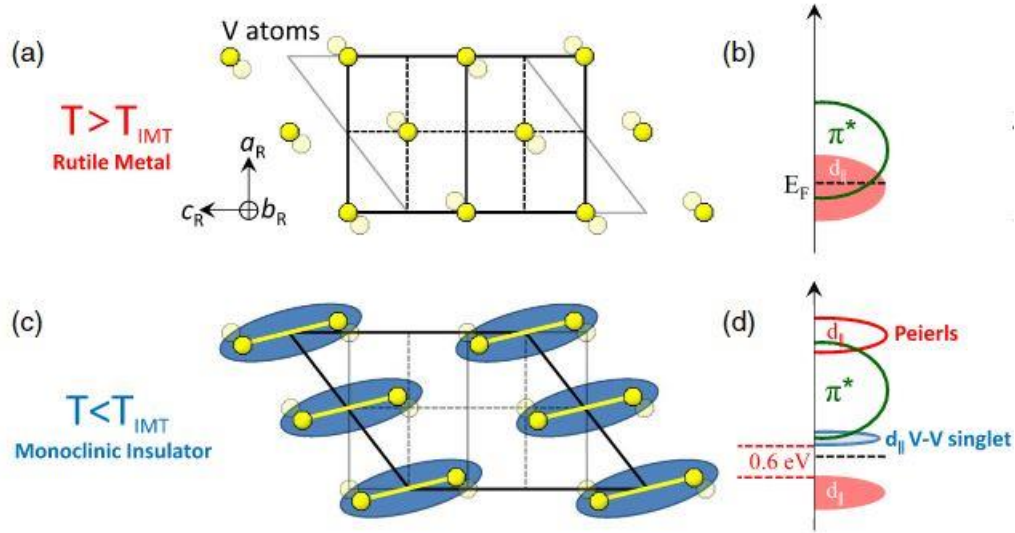


Figure 1.1: a) The crystal structure of VO₂ in the high temperature, rutile metallic (P4₂/mnm) phase. b) The corresponding rutile band plot. The π^* and $d_{||}$ bands of V 3d states overlap at the Fermi energy, allowing conduction. c) The crystal structure of low temperature, monoclinic (M1, P21/c) insulating phase. V-V localize 3d electrons inhibiting conduction. d) The corresponding band plot showing a 0.6 eV charge gap associated with the V-V dimerization. [2]

This system has also drawn interest from theorists, as the complex nature of this strongly-correlated electron system leads to challenges in producing models that capture all observed experimental phenomena. Many physical interpretations have been proposed that capture at least some elements of the MIT, and can broadly be placed in two categories where Peierls or Mott-Hubbard [14] like mechanisms dominate. Peierls [14] models stress electron-phonon interactions while Mott-Hubbard [15] models argue for the dominance of electron-electron correlations.

An important aspect of the MIT relevant to this work is the phase coexistence of the monoclinic and rutile state within the transitional regions. This phase coexistence has long been suggested to provide a phenomenological description of transition features such as temperature-dependent infrared properties [16], but more recently was directly characterized in the bulk and epitaxial films through techniques including scattering scanning near-field infrared microscopy (s-SNIM) [17], low-energy electron diffraction (LEED), x-ray photoemission electron

microscopy (XPEEM) [18], and direct optical imaging [19]. Figure 1.2 shows the phase coexistence in bulk VO_2 near T_c with s-SNIM. The transition progresses first with the formation of sparsely populated nanoscale metallic domains, eventually coalescing into larger metallic island like regions. As T increases, these island regions grow and form a complex network through the sample volume. The seemingly random domain formation and path building is described by percolation models that have been reasonably successful in describing transition characteristics such as the DC resistivity.

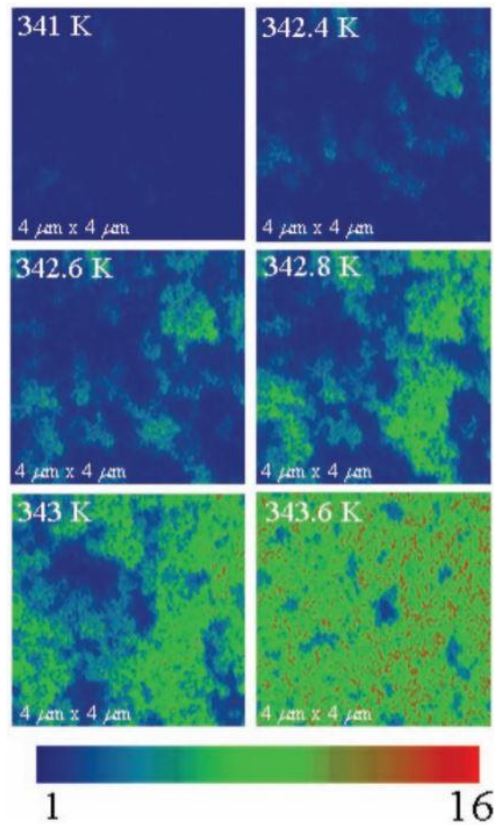


Figure 1.2: s-SNIM imaging of bulk VO_2 at temperatures very near T_c . The green and red regions represent increased IR scattering and are associated with the rutile metallic phase. The percolation like transition mechanism is clearly visible. [17]

Interestingly, in epitaxial thin films this phase coexistence no longer progresses straightforwardly as random metallic domain formation, but often includes the formation of long

nanoscale metallic filaments [20]. This has been detailed extensively in VO₂ films grown onto rutile TiO₂ substrates, the primary material system discussed in this text. Figure 1.3 presents LEED and XPEEM images of this stripe domain formation along the rutile (110) direction. In epitaxially strained films the MIT seems to proceed through a three-stage process, initially characterized by sparsely populated domain growth as in the bulk. At a critical density, these domains stabilize into the metallic stripe networks seen in the image. At higher temperatures additional domain formation within the monoclinic channels cause filament interconnection and finally the transformation to a fully rutile metallic film. [18]

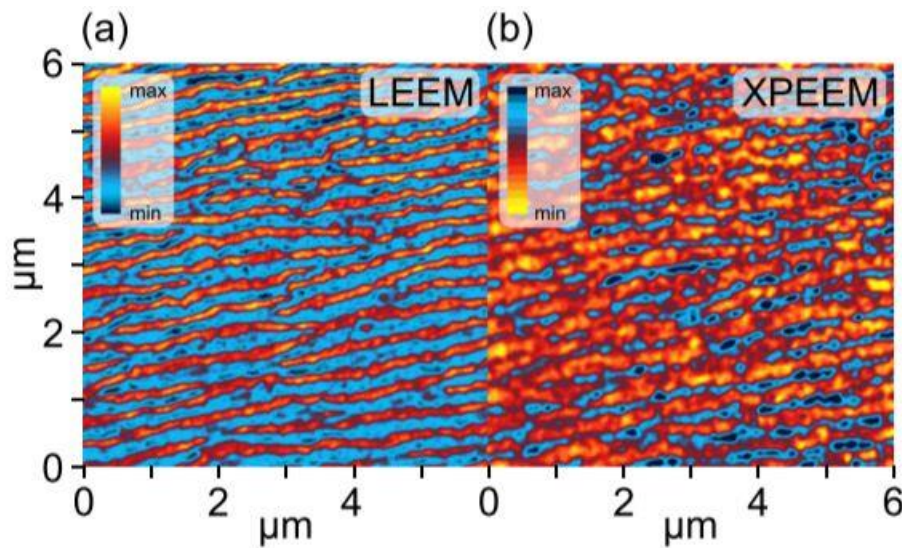


Figure 1.3: a) LEEM and b) XPEEM imaging of the MIT in epitaxially strained VO₂ films grown on TiO₂ substrates. A corrugated stripe patterning is seen along the rutile (110) crystal direction. This metallic filament formation is one origin of the anisotropic resistivity seen in axis isolated transport measurements where the $c_r T_c$ is seen to be higher than that of a_r . [18]

The complexity of this phase transformation makes VO₂ an interesting candidate for dynamic transport characterization experiments. This thesis summarizes the experimental details and findings of three projects centered around the MIT of VO₂ thin films:

1. Characterization of long timescale relaxation effects with impedance spectroscopy: It has recently been shown that VO₂ exhibits a long timescale relaxation effect when settling at temperatures in proximity of T_c. This is characterized by a resistance drift with a magnitude as high as 20% over 5 hours of settling time. This drift is likely caused by the continued formation and stabilization of metallic domains due to thermal fluctuations in the sample. As this formation effectively follows the behavior of random percolation in bulk, with additional metallic filament formation in epitaxial films, this process could reasonably be modeled as a random resistor-capacitor network. In this chapter, we probe VO₂ films with impedance spectroscopy to track the time evolution of the equivalent capacitance and resistance and analyze these results in regards to the percolation network model of the MIT.
2. High Temperature Ferromagnetic Resonance Studies of VO₂(110)/Ni₈₀Fe₂₀(Py) Heterostructures: In this study, we explore spin pumping in heterostructures of VO₂/Ru/Py. Spin pumping is a magnetic relaxation process with an interfacial origin, where an oscillating ferromagnetic (FM) film pumps spin polarized current into neighboring metallic layers. As VO₂ shows a dramatic increase in conductivity (10⁻¹ to 10³ Ω⁻¹cm⁻¹) through the MIT, as well as sharp increase in the magnetic susceptibility [21] at T_c, we propose VO₂/Ru/Py structures as a candidate system for modifiable spin pumping applications. As the spin pumping contribution should be directly proportional to the spin mixing conductivity, which should be enhanced dramatically upon the MIT, it could be reasonably predicted that the effective damping parameter should be modified upon the MIT. Here we present results of a series of temperature dependent FMR studies

extracting the change in effective damping associated with increased spin pumping into the metallic VO₂ layer post transition.

3. Low frequency noise spectroscopy of the metal-to-insulator transition of patterned VO₂ thin films: In this chapter, we study the temperature dependence of the low-frequency noise parameter through a wide range of temperatures below, within, and above the transitional range. We make use of Hall bar patterned films to isolate transport characteristics along the (100) a_r and c_r axes to study anisotropic noise profiles. We present evidence that the 1/f noise prior to the fully metallic transition is dominated by thermal fluctuations in the isolated metallic domains. We also suggest that the noise profile seen in the fully metallic film follows a unique scaling with film resistance (R⁻³) that is likely arising from the bad-metal nature of rutile VO₂.

Additionally, the appendix to this thesis contains a United States patent (#9,842,615) [22] issued for a TMR magnetic reader stack modification that was designed and characterized while working as an intern at the Western Digital Corporation in Fremont, CA within their Reader Design group. The reader stacks were characterized on a home-built CPW based FMR system (similar in design to the system utilized in Chapter 5) for which I wrote both the controller software and MATLAB based analysis tools. Due to limitations on data publication, the specific details of this project cannot be included in this document, but as the patent includes a mostly comprehensive description of the reader design and working principles, it is included in the appendix in its entirety.

CHAPTER 2:

DEVICE FABRICATION AND CHARACTERIZATION TECHNIQUES

2.1. Introduction

In this chapter, we will summarize the techniques used in the fabrication and characterization of the VO₂ films described in Chapters 3-6. In the first section we describe the design and operation of the homemade low-pressure chemical vapor deposition system (LPCVD, or for our purposes simply CVD) used to grow our VO₂ thin films. For samples in Chapter 5, additional deposition steps were performed using the RASCAL magnetron sputtering system to produce magnetic bilayers and trilayers for FMR experiments. We also summarize the photolithography techniques implemented to produce Hall bar patterned films isolating the transport characteristics of the a_r and c_r axes, utilized in the noise spectroscopy experiment in Chapter 6. The photolithography steps were completed at the Microfabrication Facility located in the North Engineering Research center on the University of Alabama campus.

The second section details the build of a high-stability, low-overshoot temperature controller, implemented in LabView. The code base from this controller was utilized in the noise, impedance, and FMR measurements and is capable of standalone operation for use with third-party measurement devices missing temperature control capabilities.

Next, we will cover the structural, surface morphology, and DC transport characterization techniques used to probe VO₂ film quality. X-ray diffraction (XRD) was used to confirm the growth of pure-phase VO₂ as well as determine the epitaxial nature of the films. X-ray

reflectivity (XRR) is utilized for thickness measurements. Atomic force microscopy (AFM) images the surface roughness making it an essential tool in optimizing the deposition of high the quality permalloy layers discussed in Chapter 5. Finally, we describe 4-point probe resistivity techniques as conducted with the Quantum Design “Dynacool” Physical Properties Measurement System (PPMS).

2.2. Film Preparation and Patterning Techniques

2.2.1. LPCVD

The VO₂ films utilized in this work were deposited with the use of a home-built LPCVD system. The low-pressure method was chosen over the simpler atmospheric pressure (APCVD) technique as the minimum roughness obtained via APCVD (~ 3nm) significantly exceeds that of the LPCVD method (~ 0.5nm).

Figure 2.1 depicts the LPCVD system components which are labelled as follows:

- A. Digital chamber pressure monitor
- B. Custom DC+AC modulation controller (for high temperature deposition)
- C. mV range multimeter for substrate thermocouple monitoring
- D. Digital mass flow controller hardware
- E. DC power supplies for precursor chamber and substrate heating
- F. Variable AC power supplies for main chamber heating and high temperature substrate mode
- G. PC with custom LabView control software
- H. Precursor chamber and heating tape

- I. Main deposition chamber
- J. Pirani gauge for deposition pressure monitoring
- K. Substrate holder tool with internal 50 Ohm joule heaters and thermocouple
- L. Mass flow controllers for main chamber buffer line and precursor flow rate control
- M. Outlet to the Welsch Duo-Seal Vacuum Pump capable of 1e-3 Torr base pressure



Figure 2.1: The home-built LPCVD system with components labeled.

The precursor used in deposition was Vanadyl(IV) acetylacetonate (V-acac) 99% from Acros Organics and the carrier gas was high purity (99%) O₂. We chose rutile-TiO₂ substrates from CrysTek with crystallographic orientations of (100), (001), and (110) and dimensions of 5x5 mm. The substrates were bonded to the holder with a silver conductive adhesive from Electron

Microscopy Sciences the ensure good thermal contact; a baking cycle of 15 min at 100 °C was performed between sample mounting and deposition to set the adhesive.

The deposition procedure was fully automated by the LabView controller and proceeded as follows:

1. The substrate, main chamber, and precursor chamber temperatures are set to 480-500 °C, 175 °C, and 135-142 °C respectively. The growth rate and roughness of the resulting films has been shown to be sensitive to the substrate and precursor temperatures and can therefore be reduced for applications where low roughness is necessary at the expense of deposition speed. This initial heating cycle lasts for 1.5 hours to allow stabilization of the main chamber temperature. During this period the oxygen buffer gas flows in the main chamber at a rate of 63 SCCM, resulting in a base oxygen pressure of 5×10^{-1} Torr.
2. At 1.5 hours the deposition cycle begins when oxygen is flowed through the precursor chamber at 25 SCCM. The O₂ flow carries evaporated precursor to the substrate surface where it reacts with the carrier gas and deposits VO₂. During this cycle, the buffer line flowrate is reduced with a PID controller to maintain the 5×10^{-1} Torr deposition pressure. The film thickness is mainly controlled by the length of the deposition cycle, which is generally set between 5 and 30 minutes producing films ranging in thickness from 5 to 150 nm depending on the temperature parameters and substrate orientation.
3. The substrate holder and chamber heaters are turned off and the sample returns to room temperature. Oxygen continue to flow from the buffer line to the main chamber during this cooling cycle to reduce oxygen vacancies.

2.2.2. RASCAL Magnetron Sputtering System

The trilayer samples of composition $\text{TiO}_2(110)/\text{VO}_2/\text{Ru}(t)/\text{Py}(t)/\text{Al}(3\text{nm})$, as described in Chapter 5, were deposited with the in house RASCAL magnetron sputtering system. The general magnetron sputtering technique begins by placing the substrate or film into ultra-high vacuum (10^{-8} - 10^{-10} torr base pressure) to ensure minimal contamination and allow for the unencumbered ballistic flow of the targeted atoms. An inert gas, usually Ar, flows into the chamber, reaching a desired pressure ($\sim 10^{-3}$ torr). The target material is connected to high negative voltage. Placed behind the target is a series of cylindrical magnets configured with alternating pole directions to produce strong magnetic fields that trap the resulting free electrons very near the target in a high-density plasma. When a neutral Ar atom enters the plasma, it will collide with a free electron and become ionized. The Ar^+ ion will then rapidly accelerate towards the negatively charged target material, colliding with the surface and ejecting atoms of the target material. These high energy ejected atoms will traverse to the substrate surface where they are deposited.

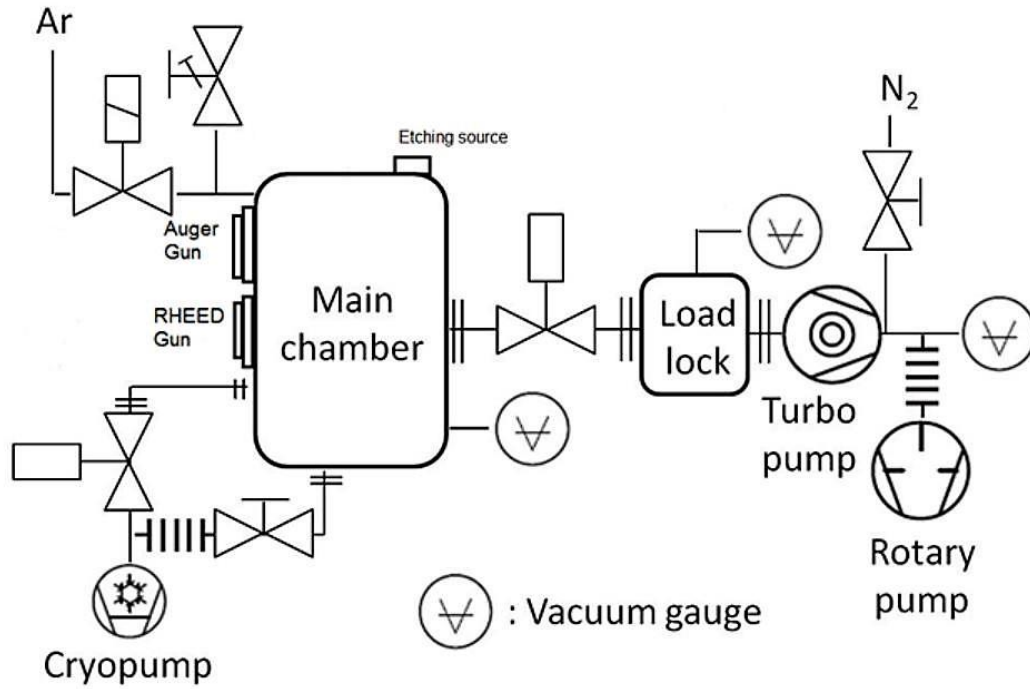


Figure 2.2: The vacuum schematics of the in-house RASCAL magnetron sputtering system.

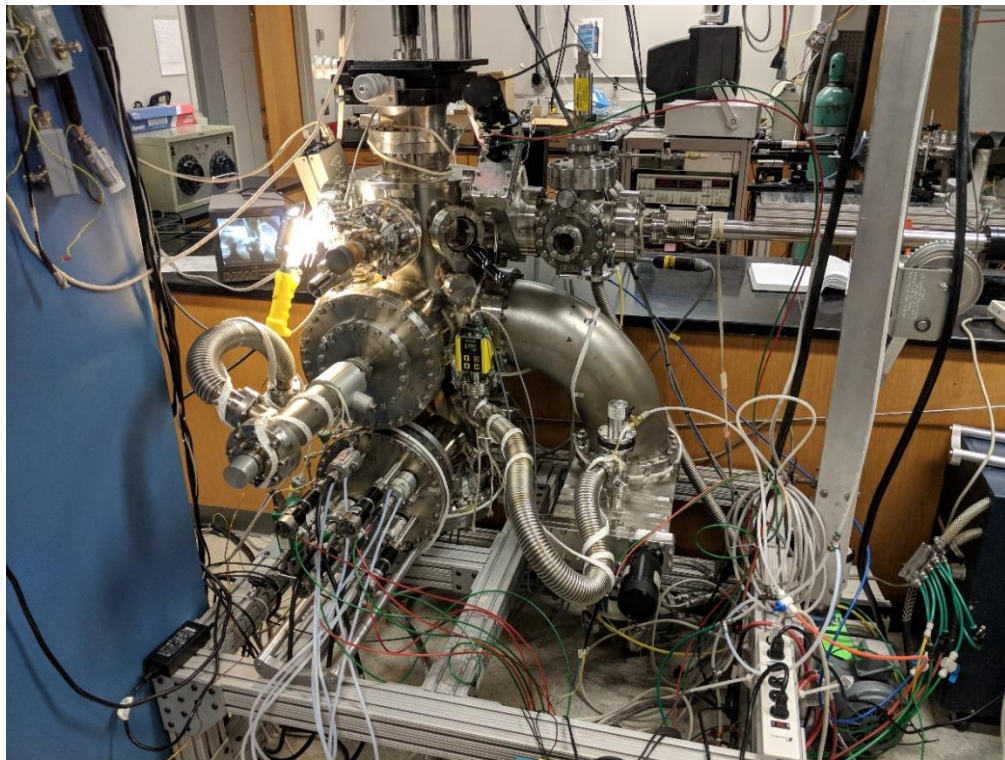


Figure 2.3: An external image of the RASCAL magnetron sputtering system.

The RASCAL sputter system has multiple sputter gun configuration allowing simultaneous deposition of up to 4 target materials. The substrate is inserted into the chamber using a load-lock mechanism that allows reduced pump down times as compared to exposing the main chamber to atmosphere. The load lock chamber is pumped down by a turbopump and rotary backing pump for a minimum of 30 minutes before the load lock valve is reopened. The sample is loaded to the main chamber via a manually operated loading arm which latches the sample to a powered vertical transport tool. After a pre-sputtering procedure is completed to eliminate surface contamination of the target, the transport tool lowers the sample to the sputtering position. The very low system base pressure of $\sim 10^{-9}$ is maintained with a cryopump.

The sputtering times are initially estimated through the use of an Inficon quartz crystal microbalance tool, though this calibration procedure can have a high error margin in certain cases and proved to underestimate the layer thicknesses in our measurements. For our samples, the required sputtering periods were determined by growing several calibration films of Ru, Py, and Al onto SiO₂ substrates for 5 minutes and then directly measuring the layer thickness with XRR (discussed below). As the growth rate is approximately linear for magnetron sputtering applications, these results could be used to determine the sputtering periods for all desired film thicknesses.

2.2.3. Photolithography and Hall Bar Preparation

A subset of our films was patterned into Hall bars (see Figure 2.5) in order to isolate transport along particular crystallographic axes. A Hall bar is a crossed shaped pattern with two, very thin orthogonal channels intersecting at the mid-point. At the ends of the channels are pad like areas used for wire-bonding. The very narrow widths of the channels approximate a 1-D

path for conduction. This patterning is usually intended for Hall conductivity measurements for the purpose of determining the carrier concentration (n) and mobility (μ) but is also effective for determining transport anisotropy [23] when the bars are aligned along the sample crystallographic axes.

Photolithography is a very common technique for circuit fabrication and is widely used in the semiconductor industry for producing circuit features as low as 5nm. The photolithography procedure is mostly consistent among many device types, and only needs minimal optimization when patterning features in our desired range of a few microns. The basic procedure is detailed in Figure 2.4.

Our patterning process was conducted with the following steps. Due to the small sample size, we attached our substrate to a larger SiO₂ wafer using double sided tape. This minimized the difficulty in handling the small sample during the exposure procedure. The sample was coated with S1818 photoresist from MicroChem. This is a positive type photoresist, meaning the regions of resist not exposed to UV during the exposure will remain at the conclusion of the patterning process. The resist was spin coated with the Laurell 650mz Spinner using a multistage procedure: an initial 3s 400 RPM spin up cycle, followed by 30s at 2500 RPM. This spin speed was chosen as it limited the pooling of resist at the corners of the sample which leads to non-uniform etching in later stages.

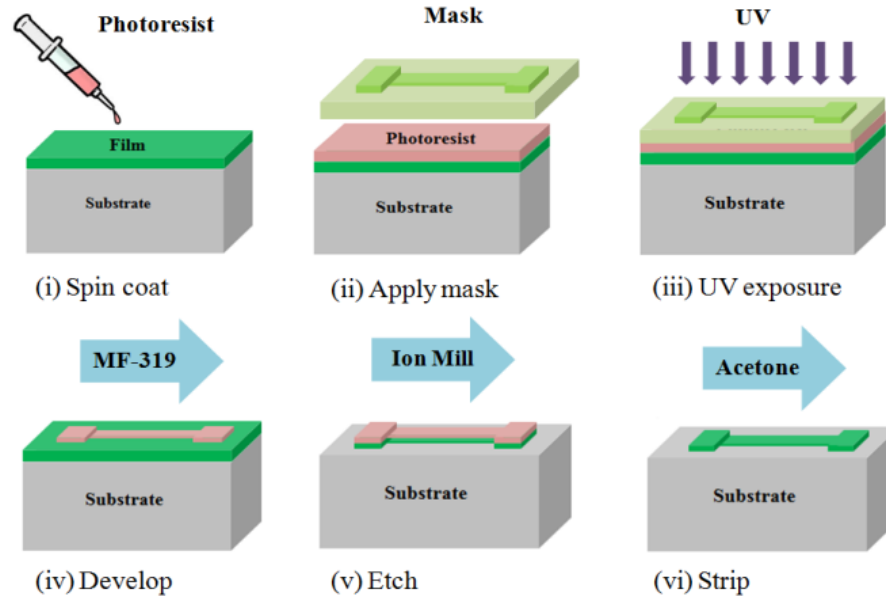


Figure 2.4: The standard photolithographic patterning procedure.

After spin coating a “soft bake” procedure was performed by placing the sample on a hot plate at 115 °C for 60s in order to set the resist in place for exposure. The sample was then placed in a Karl Suss MA6/BA6 mask aligner. Before alignment, the Hall bar mask was carefully cleaned with acetone and isopropanol. The mask alignment was carefully chosen to ensure the maximum number of Hall bar features within the small sample region. As described above, even with the optimized spinning speed some edge pooling is unavoidable so careful consideration was taken to ensure the majority of the Hall bar features remained far from the sample edges. This system utilizes a 900W UV source which was applied for 9 seconds in the soft contact mode. This exposure period is slightly longer than normal (6-7s) to increase the depth of the exposure as the expense of feature resolution. As our features are on the order of microns, there is little impact to the quality of the patterning. The exposure stage is followed by a bath of MP319 developer for 90 seconds followed by an additional bath of de-ionized water for another 90 seconds.

The development was followed by a “hard-bake” at 115 °C for 5 minutes to further harden the unexposed resist areas. We then performed a plasma ash (descum) procedure to enhance the etching performance. This step removes any undeveloped photoresist from the unmasked areas as well as cleans any organic contaminants originating from device handling between patterning stages. The plasma ash tool was set to 250 W at 1 Torr O₂ pressure; prior to the ashing step a two minute O₂ purge cycle was performed. This system showed a base pressure of approximately 100 mTorr.

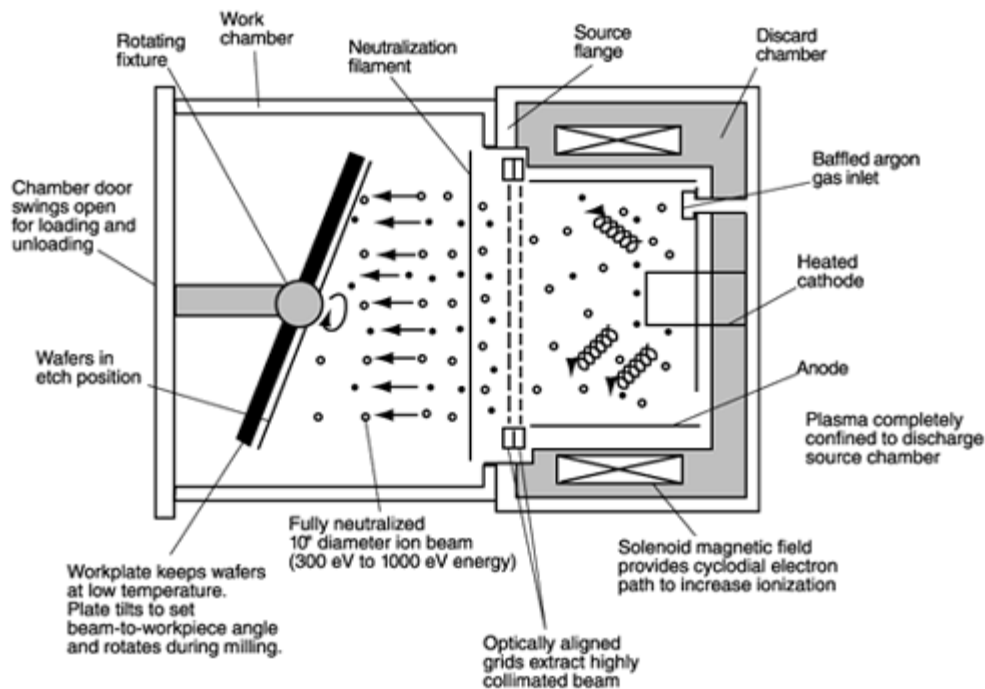


Figure 2.5: The internal schematics of an ion milling system. Not pictured is a wafer cooling system that maintains a constant 5° C sample temperature throughout the milling procedure. [24]

Etching was completed using an ion milling procedure with the Intelvac milling system. The schematics of a comparable ion mill system are presented in Figure 2.5. The ion mill behaves in a similar manner to the sputtering system described above. The sample is placed in the main chamber and pumped to a high vacuum ($\sim 10^{-7}$ torr). Ar atoms are ionized via a charged filament. The Ar⁺ ions are accelerated towards a metallic mesh that is kept at a high negative

voltage. Most pass through due to their high momentum, at which point they are deionized by a neutralization filament. As with the magnetron sputtering system, these Ar atoms then impact the sample surface which ejects material through momentum transfer. The ion milling time must be optimized for the sample thickness to avoid etching into the substrate.

Etching was performed at a 45° etch angle with a 200 V beam voltage and 64 mA beam current. The state is rotated during milling to ensure etching uniformity. The stage is water cooled to 5 °C to avoid heat generation due to the Ar bombardment. The ion milling is followed by an acetone wash to remove the remaining hardened resist above the unetched VO₂ layer. The results of the photolithography process are shown in the optical microscope image in Figure 2.5. The high-quality features and limited edge pooling effects are noticeable in this example.

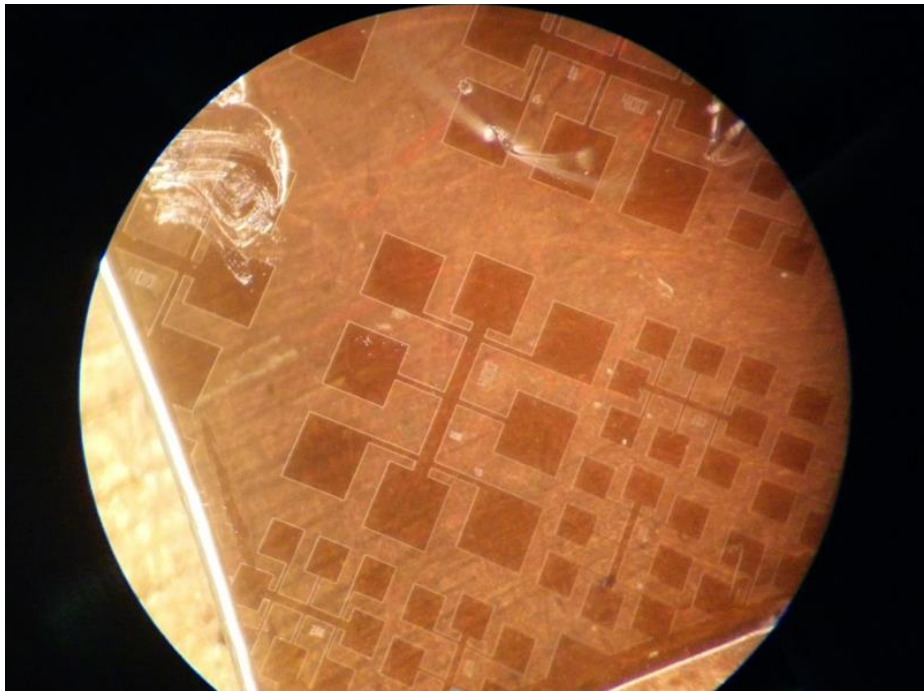


Figure 2.6: Hall bar patterns on a TiO₂/VO₂ (110) film. The optimized spin coating speed and exposure time enhanced the quality of features at the edges of the sample.

2.3. Low-Overshoot Temperature Controller

As previously mentioned, the MIT is highly sensitive to temperature with even small thermal fluctuations inducing relatively large changes in the resistance state. As the MIT is also hysteretic in nature, an overshoot (or undershoot, in cooling cycles) of the setpoint temperature will result in an undesired and nonreversible system state. As such, temperature dependent measurements of VO₂ based material systems requires a highly accurate temperature controller with minimal overshoot/undershoot and low temperature deviation during the measurement period.

The temperature controller is built around a PID (Proportional-Integral-Derivative) based feedback scheme defined by the following function [25]

$$P(t) = K_p e(t) + K_i \int_0^t e(\tau) d\tau + K_d \frac{d}{dt} e(t)$$

where $P(t)$ is the time dependent output power of the heater current source, K_p is the proportional scaling term, K_i is the integral term, K_d is the derivative term, and $e(t)$ is the time dependent error function as defined by

$$e(t) = SP - PV$$

where SP is the setpoint and PV is the process variable. In our case the setpoint and process variables are the desired temperature and current temperature in units Kelvin, though in general these may represent any system variable needed to be controlled. The proportional term contributes to $P(t)$ only when there is some offset between the current and desired setpoint, and linearly reduces its contribution as the process variable nears the setpoint value. The integral term captures the long-timescale behavior of the error function and will increase or decrease the output over time if system state is not nearing the expected setpoint value. The derivative term

corrects for rapid changes in the error function and can help minimize spikes in output power due to fluctuations in the ambient temperature.

This standard PID control scheme proved insufficient for our applications, even after multiple tuning procedures, as the overshoot generally exceeded 1 K near T_c (Figure 2.7, a). To further limit temperature overshoot, we added a heater model to the PID algorithm. The heater model was created by recording the steady state output of the power supply as a function of the set point temperature after a settling time of 1 hr. This model provided a bias to the heat output upon a user controlled change in the setpoint variable, upon which the PID could further refine $P(t)$. Overshoot was further limited by controlling the maximum power adjustment from the PID algorithm, which was generally set to $\pm 10\%$, but was increased slightly for the modified FMR heater controller described in chapter 4. The output limiter can be deactivated to increase the settling speed (at the cost of overshoot) for samples where overshoot is not an important consideration. The schematics of the controller software are presented in Figure 2.6. The improved temperature control performance near T_c is seen in Figure 2.7b.

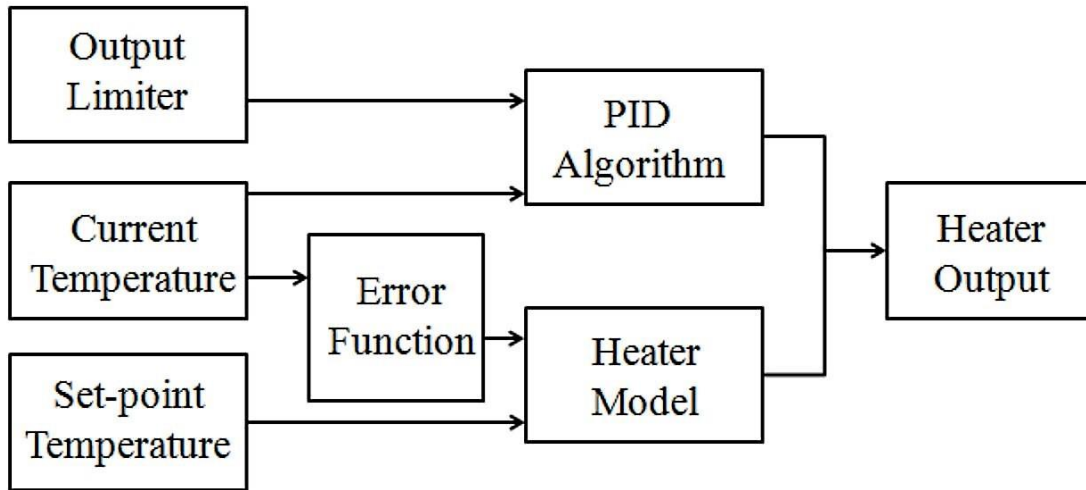


Figure 2.7: The final version of the software control scheme utilized in our low-overshoot temperature controller. In this example, the heater model VI strongly biases the output value while the PID algorithm modulates this value within a limited range ($\pm 10\%$).

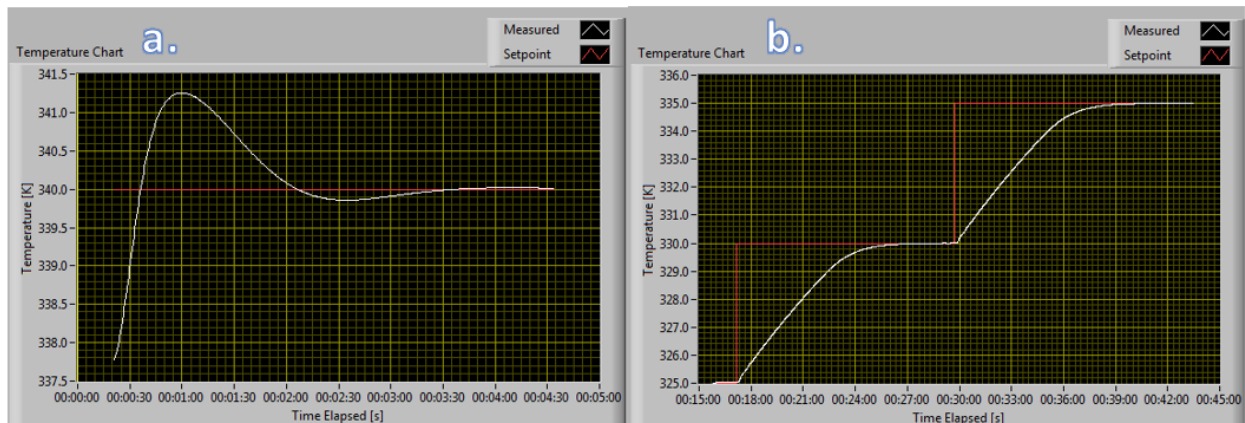


Figure 2.8: a) The time dependent temperature profile of a calibration sample when controlled with a typical PID feedback loop. Overshoot of ~ 1.25 K is seen with an additional ~ 0.25 K undershoot before the oscillation settles. b) Temperature settling profiles implemented with the heater model assisted PID controller. Overshoot of less than 0.05 K is seen in all temperature ranges.

The heater hardware is shown in Figure 2.8. The base was taken from a Quantum Design PPMS breakout box to match its pinout configuration for increased interoperability with other prebuilt measurement systems and tools available in the lab. The sample is mounted to a copper heating block that sits on a 50 W, 25 Ω Joule heating element. The power source was a GPIB

controlled HP-6654A DC power supply. For the experiments described in Chapters 4 and 6 the sample temperature was monitored with a Lakeshore DT-600 diode temperature sensor, chosen for its high temperature sensitivity (0.01 K). For the FMR experiments described in Chapter 5 this was replaced with a standard K type thermocouple due to sample mounting limitations with the coplanar-waveguide.

The final controller configuration showed a high temperature stability of less than 0.01 K upon stabilizing at the setpoint temperature. Overshoot was limited to 0.05 K across the entire operable range. The maximum setpoint temperature was capped at 400 K which allowed for temperature dependent measurement deep into the metallic state of VO_2 .

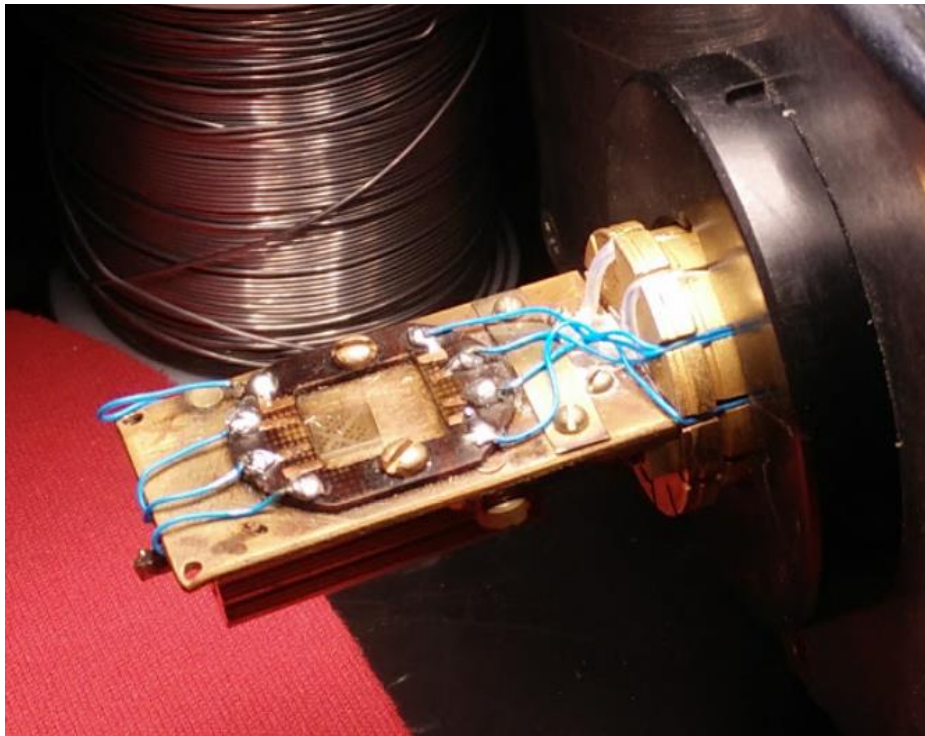


Figure 2.9: The custom designed sample holder showing a mounted Hall bar patterned VO_2 sample. The 1 cm^2 staging area and 8 signal wires allowed for two simultaneous 4-point probe measurements.

2.4. Device Quality Characterization

2.4.1. X-Ray Techniques

After CVD deposition, all samples were systematically probed with a Philips Xpert X-ray diffractometer system. X-ray characterization is a powerful tool for structural characterization of thin films that can provide details on sample thickness, surface roughness, composition, lattice mismatch, strain, and inhomogeneity. The basic schematic of an X-ray diffractometer system is presented in Figure 2.9. All systems will include an X-ray source, detector, and sample mounting stage. The angle between the X-ray source and sample plane is usually defined as ω while the detector angle, which is referenced from the incident beam path vector, is defined as 2θ . Multiple measurement modes are available in most systems, but the basic principle is the same in all variations in that the detector measures the scattered X-ray intensities as a function of ω or 2θ while the sample is kept stationary in the beam center.

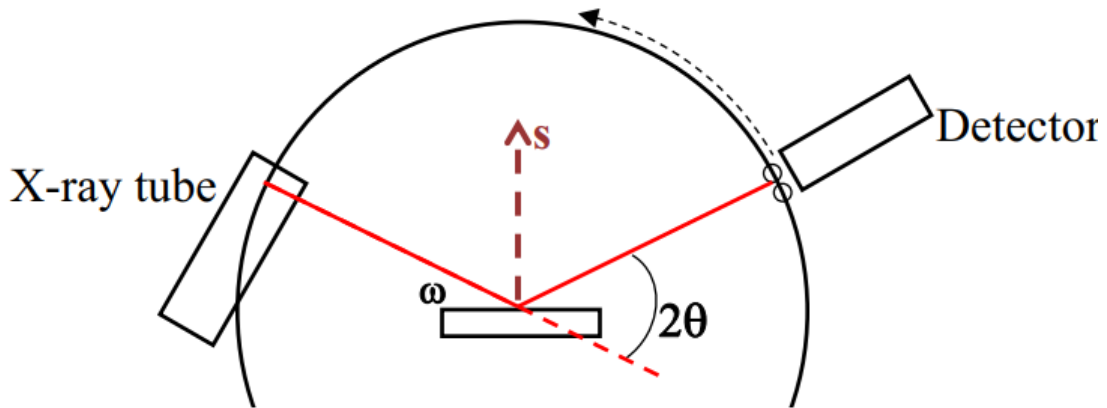


Figure 2.10: The standard X-ray diffractometer configuration. ω is defined as the angle between the film tangent the incident X-ray beam path. 2θ is angle between the incident and diffracted beam paths. [26]

The technique is derived from the well-known Bragg condition

$$n\lambda = 2d_{hkl}\sin(\theta)$$

where λ is the X-ray wavelength and d_{hkl} is the crystal plane spacing. The Bragg condition is only met for a single angle θ for each family of crystal planes. Due to this relation, by performing a coupled θ - 2θ scan one can confirm sample structure by comparing the measured Bragg peak location and line shape to the known peak angle for a given material and crystal structure.

We can also measure a rocking curve, where ω is swept through the Bragg angle by tilting the sample in relation to the X-ray source. The FWHM of this curve is indicative of the epitaxial quality and strain due to lattice mismatch.

The same system can be used to perform X-ray reflectivity (XRR) measurements where we can examine the angular dependence on the interference between the reflected waves from the film surface and substrate-film interface. This is performed by setting 2θ initially to 0 degrees and sweeping upwards through the critical angle. The periodicity of the interference fringes can be used to determine the film thickness. Usually XRR fitting software (such as GenX [27]) is used to accurately determine the thickness.

2.4.2. Atomic Force Microscopy

The surface topography was probed with the Asylum Research (now Oxford Instruments) MFP-3D Stand Alone AFM tool. This tool can image surfaces with a maximum area of $90\mu\text{m}^2$ and depth features as low as 0.02 nm. The general AFM schematics are presented in Figure 2.10. An atomically sharp cantilever is scanned across the sample surface which is mounted to a computer controlled piezoelectric scanner. The cantilever tip interacts with the sample surface through attractive Van de Waals and repulsive Coulomb forces to maintain a nearly stable distance from the sample surface. As the tip moves across surface features of varying topologies,

the cantilever is deflected. A laser is reflected from the back of the cantilever and is detected by a four-sectional photodiode to track both vertical and horizontal deviations. The deflection data is used to build 2D or 3D mapping of the sample surface. For our purposes, the system was set to a tapping mode, where the tip is oscillated near the sample surface and the tip-to-surface distance is tracked by monitoring changes in the cantilever resonance frequency.

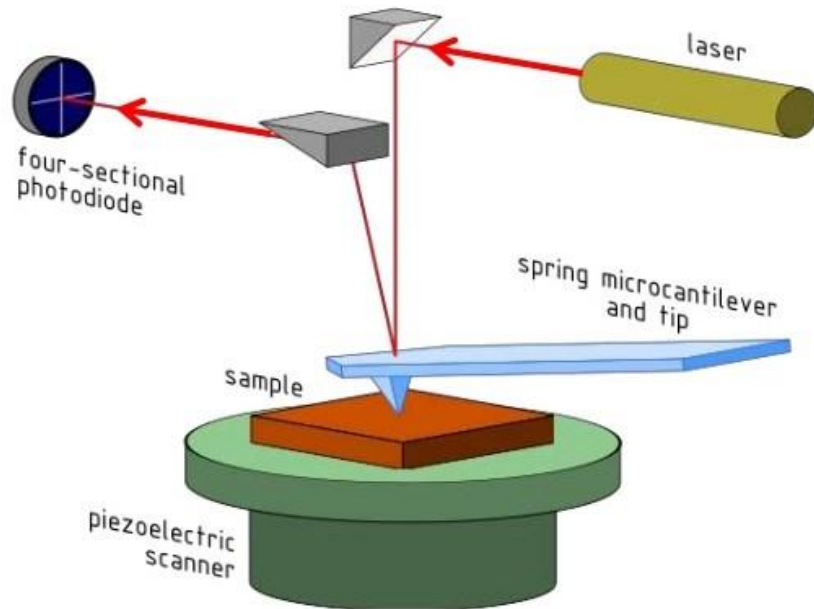


Figure 2.11: Working principles of an AFM measurement tool. [28]

2.4.3. Resistivity Measurements

Resistivity measurements were used to determine the magnitude of the MIT, the transitional width, and transport anisotropy in patterned Hall bar samples. This was generally the final step in our sample characterization, as another rough indicator of high quality VO_2 is a transition magnitude on the order of 10^3 or larger. Measurements were performed with both a custom LabView based resistivity tool and with the Quantum Design Dynacool PPMS system.

The self-written resistivity measurement system utilized a HP (now Keysight) 4778A digital multimeter via GPIB. The system featured the same temperature control scheme as described above. The benefit of this system over commercial products was the easy customizability of the measurement type, which could be modified by the user by adjusting an automation sequencer running in parallel with the measurement software. Automated sequences were implemented for standard hysteresis loops, time dependent resistance tracking, and first-order reversal curves (FORC).

Resistivity measurements were also collected with the Dynacool PPMS. This system has broad characterization capabilities including vibrating sample magnetometry (VSM), torque magnetometry, Hall effect, DC transport, and many others through the use of easily interchangeable measurement accessories. The system has a temperature range of 1.8 K – 400 K that is achieved with a ^4He based gas flow controller. The temperature controller allows a low-overshoot mode that is ideal for the purposes of VO_2 resistivity measurements. The system also features a 9T superconductor based magnet for field dependent measurements.

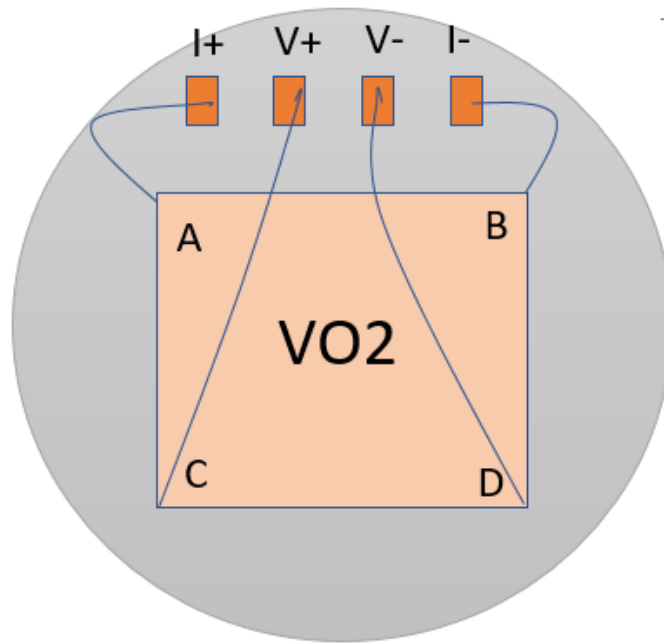


Figure 2.12: A sample bonding diagram for a 4-point probe measurement in the Van der Pauw configuration. The bonding pad configuration used is standard for Quantum Design measurement pucks and related accessories.

Samples were bonded using a 4-point probe technique in the Van der Pauw configuration (Figure 2.11). The 4-point configuration improves upon the standard 2-point method by injecting current through two of the leads while independently monitoring the resulting voltage between the other two leads. This allows the exclusion of extrinsic contributions like contact and lead resistance that would be included in series with the intrinsic sample resistance in a 2-point configuration.

The Van der Pauw method is most accurate in homogenous samples that are square in shape. The leads are bonded to the corners of the square as close to the edge as possible. The cross-sectional area of the leads should be small in relation to the sample dimensions. A pair of four-point resistance measurements are collected: once with current flowing from site A to site B with the voltage measured between C and D (R_{ABCD}) and then again with the current flowing from B to C

with voltage measured between D and A (R_{BCDA}). The resistivity can then be extracted by fitting to the Van de Pauw formula

$$e^{-\frac{\pi t R_{ABCD}}{\rho}} + e^{-\frac{\pi t R_{BCDA}}{\rho}} = 1$$

where t is the sample thickness. [29] [30]

The resistivity calculation is simplified when probing Hall bar patterned samples as the sample conduction is isolated down a narrow path with a clearly defined rectangular geometry (Figure 2.12). In this configuration, the current is applied at sites A and B and the voltage is read across sites C and D. The resistivity is calculated as

$$\rho = \frac{wtV}{L I}$$

where w is the width of the Hall bar path between A and B, L is the bar spacing between sites C and D, and t is the sample thickness.

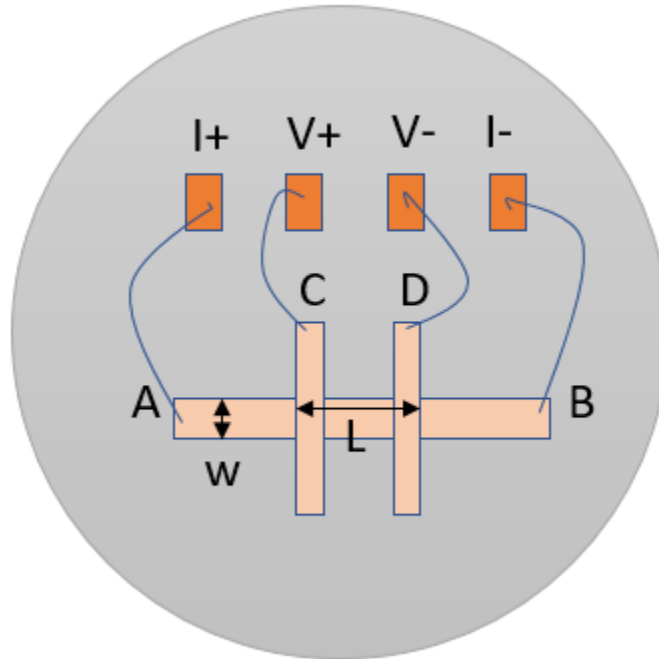


Figure 2.13: 4-point probe configuration for Hall bar patterned thin films.

CHAPTER 3: SUMMARY OF STRUCTURAL AND TRANSPORT CHARACTERIZATION

In this chapter, we will present a brief summary of the structural, topographical, and DC resistivity characterization of VO₂ thin film samples grown on rutile-TiO₂ (100), (001), and (110) substrates using the home built LPCVD system described in Chapter 2.

The first section provides crystallographic and transport characterization of the films that is relevant to all the experiments discussed in this text. Specifically, this summary is derived from the characterization data presented in the publication [31] which covers low frequency noise spectroscopy experiments of patterned VO₂ thin films. This publication is also the topic of Chapter 6 in this thesis. Due to the high cost of the TiO₂ substrates, when possible the films from previous experiments were reutilized in later work. As such, the VO₂ samples described in Chapter 4 are from the same series as discussed in the characterization below.

The second section describes the topological optimization and AFM roughness measurements of VO₂ (110) and (001) samples utilized in the bilayer and trilayer heterostructures discussed in Chapter 5.

Additional details pertaining to the characterization of films grown in our LPCVD and APCVD systems can be found in [32] [33] [34].

3.1. X-ray Diffractometry and Resistance Results

θ - 2θ scans for the all film orientations are shown in Figure 3.1. The quasi-rutile (200), (002), and (200) peaks for the VO₂ films and TiO₂ substrates are marked in the figure. The peaks for the (100), (110), and (001) films are found at $2\theta = 39.9^\circ$, 27.9° , and 65.3° respectively. These very nearly match the peaks found in the bulk, but the small offset indicates some degree of strain due to a small lattice mismatch between bulk VO₂ and rutile TiO₂. The rocking curve profiles are also presented in Figure 3.1. A FWHM value below 0.5° generally is indicative of high epitaxial quality and is well below this value for all examples. The extracted values for the a_r and c_r lattice constants, along with the calculated strain based on the TiO₂ lattice constants, is summarized in Table 3.1.

Additionally, a ϕ scan was performed to further confirm the quality of the epitaxy. A ϕ scan is an asymmetrical scan type that involves tilting the sample stage (ψ) so that an off-axis crystal plane normal will bisect the incident and diffracted beam angle to allow detection, as depicted in Figure 3.2. Once the stage is aligned for detection of the off-axis plane, in this case the rutile (101) plane, the stage in-plane angle, ϕ , is swept through a full rotation. For both rutile and monoclinic crystal structure we can expect a two-fold symmetry with peaks at $\phi = 0^\circ$ and 180° . The results of this measurement is presented in Figure 3.3. The clear two-fold symmetry and lack of additional peaks indicate high quality epitaxial growth.

Figure 3.4 shows the results of the reciprocal space mapping of a VO₂ (100) film for the off-axis (301) planes. The extracted values for the a_r and c_r lattice constants show close agreement with those found in the θ - 2θ scans. The lattice constant distributions shows a very low (FWHM), another indicator of the highly quality epitaxial nature of these films.

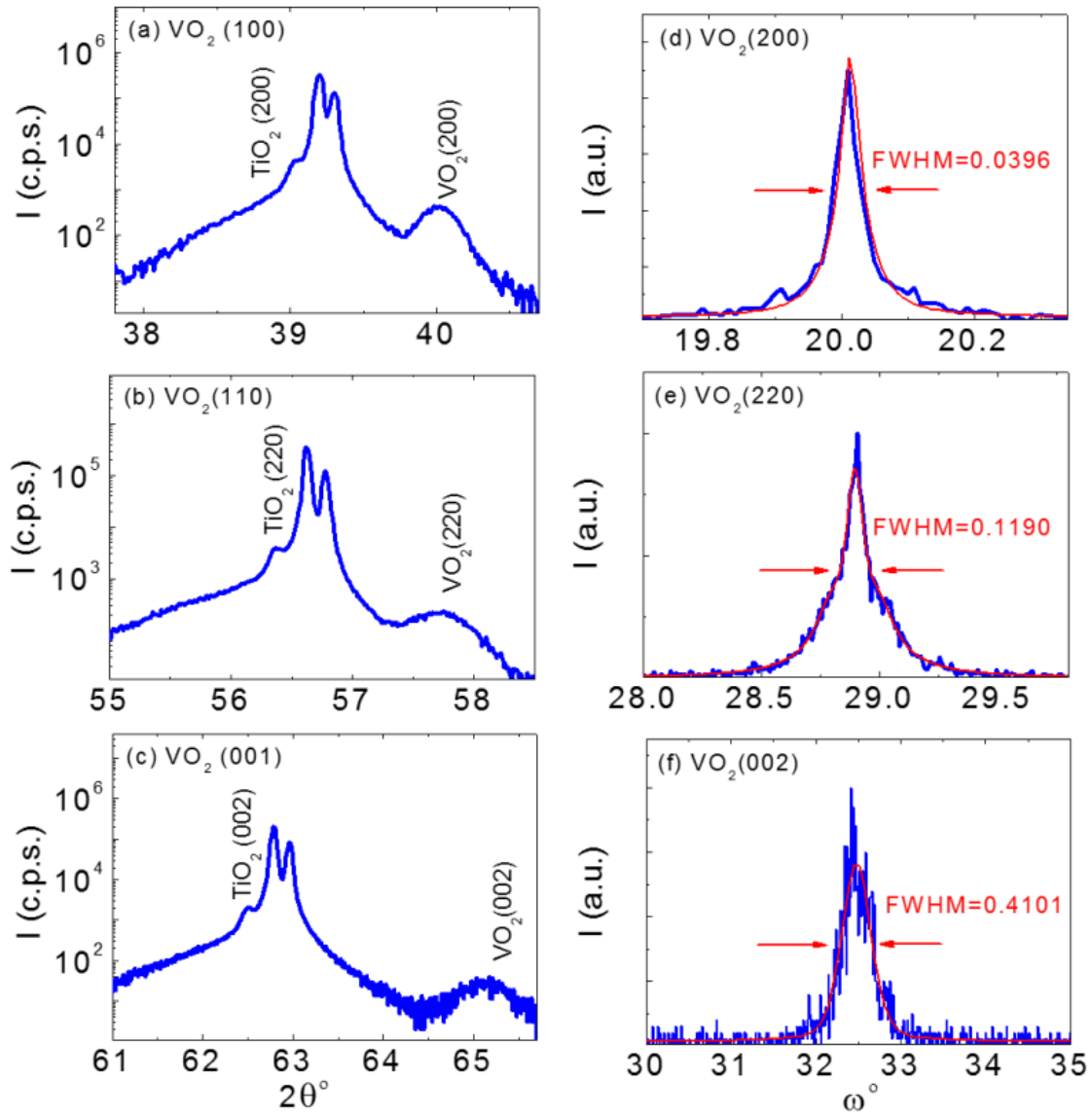


Figure 3.1: Results of θ - 2θ and rocking curve measurements for $\text{VO}_2(100)$, (110) , and (001) films. The narrow FWHM values indicate highly textured films.

Crystallographic

<i>orientation</i>	a_r (nm)	c_r (nm)	a_r strain (%)	c_r strain (%)
(100)	0.451	0.287	-0.830	0.524
(110)	0.452	0.288	-0.615	0.699
(001)	0.453	0.287	0.439	0.314

Table 3.1: The a_r and c_r lattice constants extracted from XRD measurements, along with the associated strain due to lattice mismatch from TiO_2

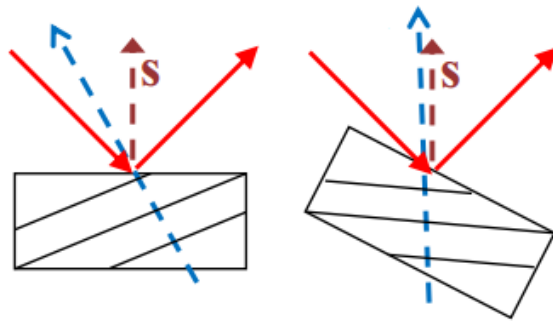


Figure 3.2: The system geometry utilized during a ϕ scan, where the sample stage is rotated about its normal while probing an off-axis plane family.

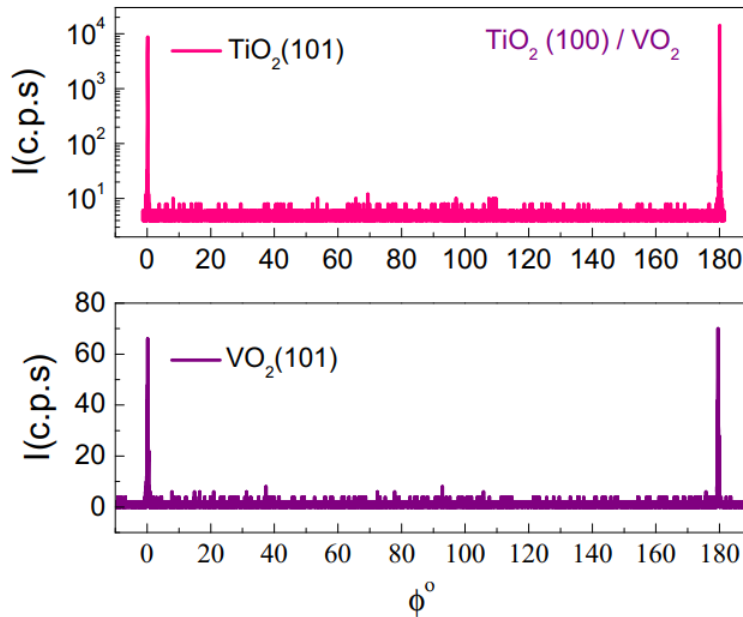


Figure 3.3: ϕ scan results show a clear two-fold symmetry in VO_2 matching that of the substrate peaks indicating high quality epitaxy.

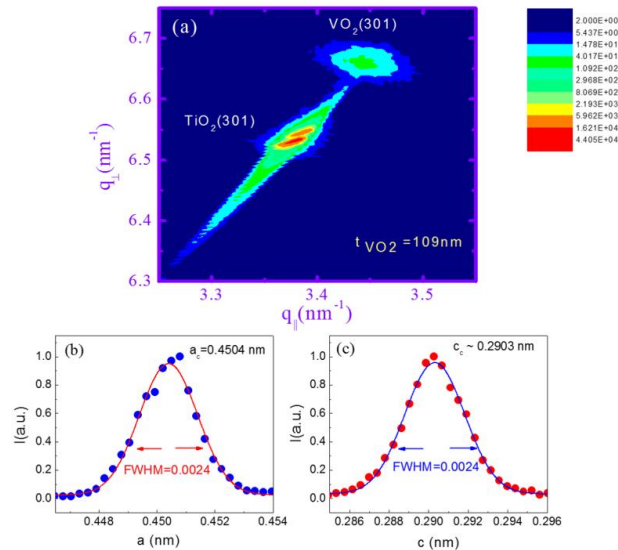


Figure 3.4: Reciprocal space mapping of the off-axis (301) peak in a VO_2 (100) film. The low FWHM in the resulting a_r and c_r lattice constant distributions are another indicator of the high epitaxial quality of these films.

Resistivity measurement results are presented in Figure 3.5 and summarized in Table 3.2.

All film orientations exhibit a clear hysteretic MIT with a large transition magnitude, defined as

a ratio of the 4-point resistance before and after the MIT. The second row of images show the calculation of T_c , which we have previously defined at the temperature where $-\frac{dR}{dT}$ is extremized. For all cases we see T_c is higher during the heating cycle, with the broadest transitional width ($T_{c,heating} - T_{c,cooling}$) seen in the (110) samples. For all orientations the transition shows less sharpness than in the bulk case, as well as an overall decrease in T_c (~ 341 K in bulk), which is likely due to epitaxial strain along the c axis, as has been suggested by previous works [35].

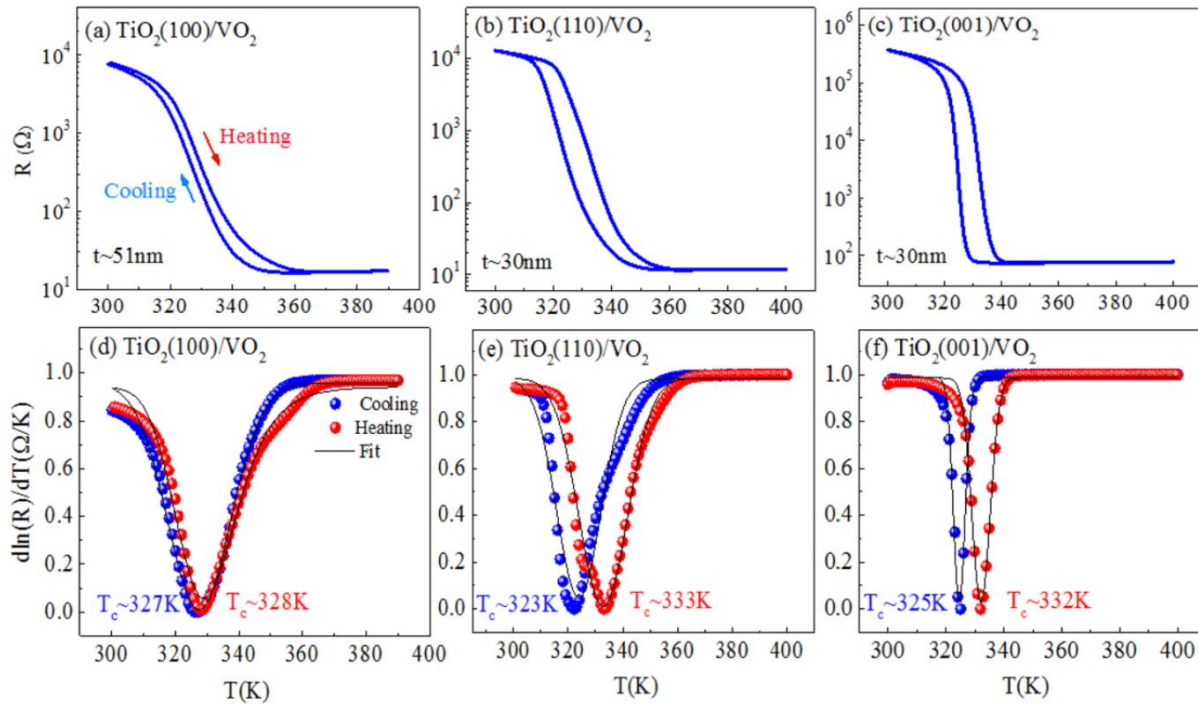


Figure 3.5: Temperature dependent 4-point resistance measurements for both heating and cooling cycles. The hysteretic nature of the MIT upon temperature reversal is clearly seen in (a)-(c). The second row shows the calculations of T_c .

<i>Crystallographic orientation</i>	Transition			Transition width (K)
	magnitude (R_I/R_M)	Cooling cycle T_c (K)	Heating cycle T_c (K)	
(100)	444	327	328	2.8
(110)	1096	323	333	10
(001)	2488	325	332	7.2

Table 3.2: Summary of DC resistance measurements. The transition magnitude is maximum in the (001) oriented films, making them ideal candidates for phase change memory and logic device applications.

3.2. AFM Topology and Roughness Optimization

As will be described in Chapter 5, the growth of high quality VO₂/Ru/Py heterostructures requires a very smooth and homogenous VO₂ film surface. Py deposited onto films with high surface roughness can exhibit overly broad (due to two-magnon scattering contributions) or multiple resonances when conducting FMR experiments that limit applicability in modeling spin transport dynamics. Our initial attempt at sputtering Py layers onto thick VO₂ films exhibited very poor resonance quality, which we attributed high-film roughness [36]. We therefore attempted to deposit a series of very low roughness (sub 1nm rms) VO₂ films for use in ferromagnetic heterostructures.

We initially chose TiO₂ (001) substrates due to the high transition magnitude (Table 3.2) of VO₂ films with this crystal orientation. A VO₂/Py bilayer with a high transition magnitude should in principal more clearly exhibit a change in the spin pumping characteristics of the heterostructure through the MIT. As VO₂ film roughness will usually scale with thickness, we utilized a relatively short deposition period of 5 minutes to minimize growth. This resulted in

films of approximately 12 nm thickness. The AFM scan for this film is presented in Figure 3.6. While the roughness is low at 0.6nm, the film features very clear microcracking defects over the entirety of the surface. While this effect is not uncommon for VO₂ films, it is generally not seen in films of low thickness [37]. Py deposited on this film again showed an overly broadened linewidth characteristic of high two-magnon scattering.

The microcracking features were eventually eliminated by increasing the deposition period to 30 minutes, resulting in films of around 80 nm. This came at the cost of film roughness, which was around 5nm in this sample. Again, the resulting bilayer showed poor magnetic resonance quality.

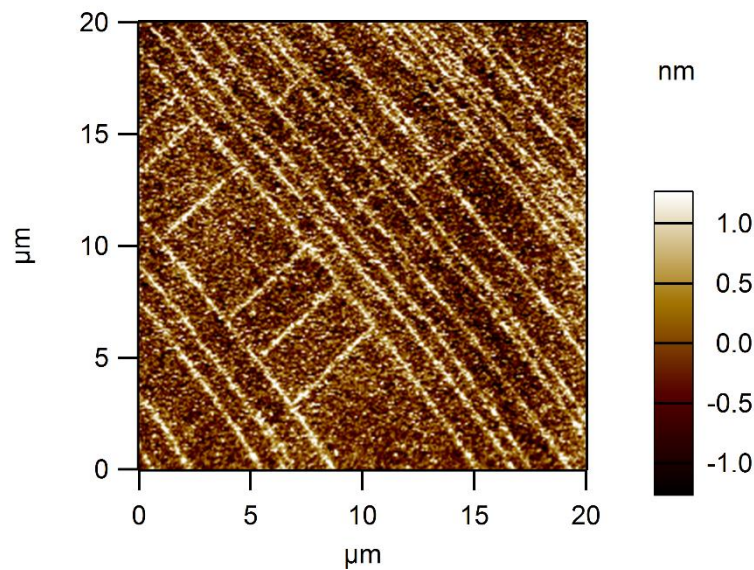


Figure 3.6: 12 nm (001) oriented film exhibiting microcracking features. These inhomogeneities resulted in a poor quality FMR resonance.

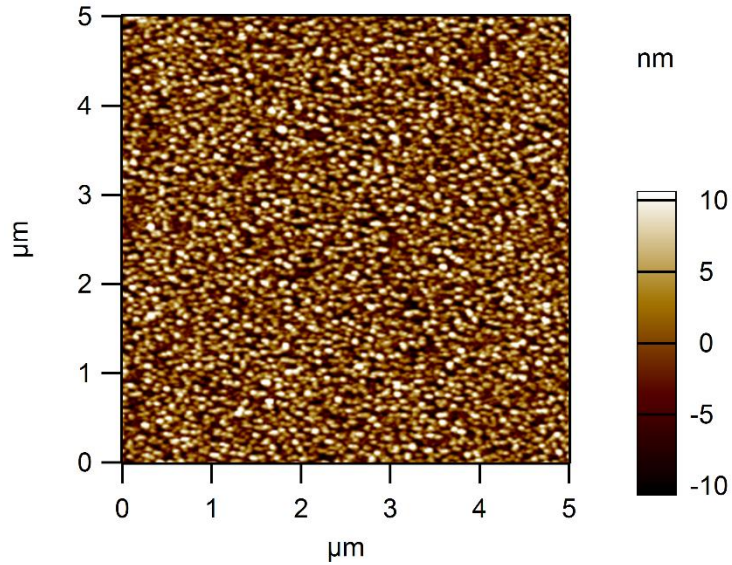


Figure 3.7: An 80 nm (001) oriented film. The microcracking features are eliminated at the cost of increased roughness. These samples also exhibited poor resonance quality due to increased two-magnon scattering at the interface.

We then attempted deposition onto TiO_2 (110) substrates. While the resulting VO_2 (110) films feature a transition magnitude around 40% of that seen for (001) films, (110) substrates have been shown to result in films of minimum roughness as compared to the other crystal orientations. We attempted a 5 minute deposition cycle at the standard deposition temperatures describe in Chapter 2. This resulted in a film of ~ 13 nm thickness with roughness of 1.6 nm. The film was homogenous and exhibited no microcracking features, but the roughness was higher than ideal for Py sputtering. To further reduce film roughness, we implemented a modified CVD deposition cycle where the substrate temperature was reduced to 468°C and the precursor temperature was lowered to 130°C . The reduced precursor flux and reaction rate at the substrate proved to increase film homogeneity and decrease film roughness to 0.48 nm rms, well within our desired range. Repeated depositions showed consistent film thickness of 11-12 nm and low roughness of ~ 0.5 nm.

Py deposited on these reduced roughness VO₂ (110) films showed narrow single resonance with good signal strength, even down to Py thicknesses of 4 nm. The detailed characterization of the spin pumping dynamics of the resulting VO₂/Py heterostructures is the topic of Chapter 5.

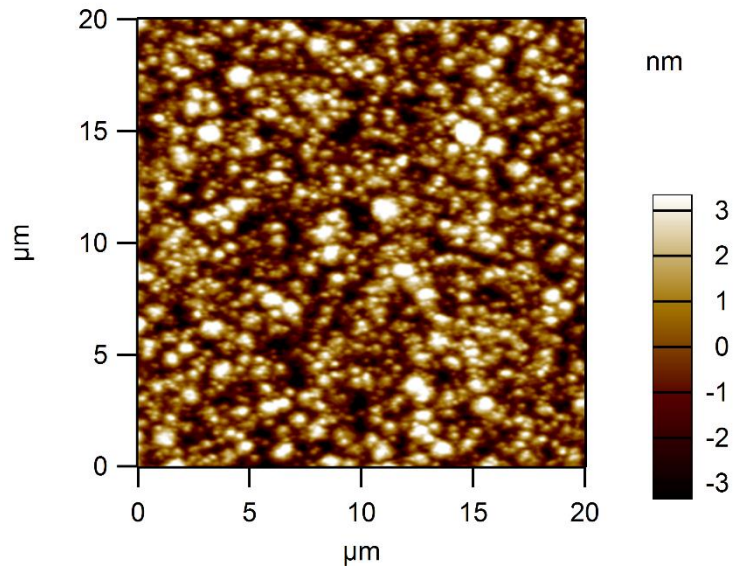


Figure 3.8: 13 nm (110) film with 1.6 nm rms roughness. While still outside of desired roughness range, this film series showed good homogeneity and strong transition characteristics.

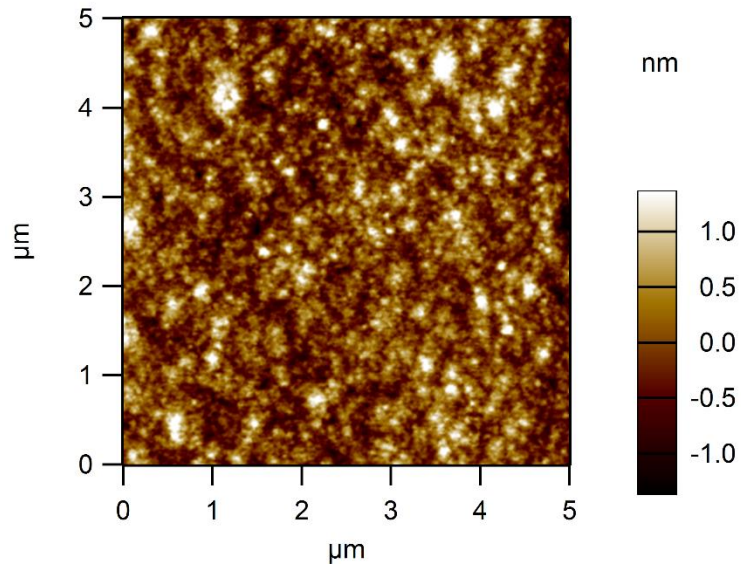


Figure 3.9: 11 nm (110) film with 0.48 nm rms roughness. This series proved to be ideal for producing FM heterostructures for FMR measurements.

CHAPTER 4:

LONG TIMESCALE RELAXATION OF VO₂ THIN FILMS ANALYZED WITH IMPEDANCE SPECTROSCOPY

The MIT has been shown to be highly sensitive to growth conditions, substrate type, and doping, allowing the T_c to vary between 290 K and 350 K [38]. This highly tunable transition has garnered considerable interest in the past decades for use in nonvolatile memory and logic devices [39]. More recently, it has been shown that VO₂ exhibits some long timescale variation in its transport characteristics, which calls into question the validity of many experiments [40] describing device level VO₂ applications where the system state would need to be stable over many years [41]. First-order reversal curve measurements of VO₂ thin films showed evidence for a persistence of high-temperature rutile metallic domains well below the T_c [42]. There is evidence that the VO₂ film does not return to the fully monoclinic (semiconducting) state until well below room temperature. These metallic domains, while only marginally modifying the sample resistance post transition, can act like nucleation points for the MIT upon temperature reversal, leading to degenerate R(T) curves for samples not reset to homogenous states.

This long timescale hysteretic relaxation appears to translate to readily measurable macroscopic features. Claassen et al [43] took simple 4-point resistance measurements of epitaxial sapphire (0001)/VO₂ (~100nm) at single temperatures over the course of ~15 hrs per temperature step. The experiment showed that sample resistance tended to relax toward an apparent equilibrium value following a log(t) behavior. This result seems to imply a wide distribution of transition temperatures which would be highly dependent on sample quality and

fabrication method. This relaxation effect has been noted in other phase change materials, specifically in NdNiO₃ thin films [44], where a nearly 20% resistance drift was observed after a 5 hour settling period near the T_c. The problem of resistance drift in some proposed phase change memory devices (list) have also been noted in literature.

With these previous works in mind, it is clear that additional studies on transition mechanisms in VO₂ should meet the following requirements:

1. A well defined and stable setpoint temperature with an easily tunable heating and cooling rate.
2. Methods for “resetting” the sample to a fully rutile or monoclinic phase between individual runs to avoid degenerate transition states.
3. For samples with T_c close to room temperature, system cooling capabilities when running sweeps from low to high temperature to ensure complete metallic domain switching.

In this chapter, we describe an impedance spectroscopy (IS) experiment that elucidates some aspects of the MIT transition mechanisms and provides data on the limitations of VO₂ in storage applications. We monitor the real and imaginary parts of the sample impedance (Z' and Z'' , respectively) at many temperature steps throughout the MIT. This data is then fit to a parallel RC circuit model to extract DC resistance and equivalent capacitance. By repeating this impedance measurement continuously over the course of several hours at a single setpoint temperature, the change in both R and C can be tracked versus time. As DC resistance is a general indicator of the electronic state of the system, time dependent variations in R should indicate modifications of the electron transport mechanisms, sample geometry, and relative population of metallic and semiconducting domains. In comparison, assuming a frequency independent dielectric function in our range of interest [45], the equivalent capacitance should only track variation of the domain

geometry and population. By comparing the relaxation trends of R and C over the course of the measurement cycle, we can provide evidence for the existence of multiple relaxation processes.

4.1. Impedance Spectroscopy

Impedance is an extension of standard DC resistance to circuits with alternating voltage sources. In a circuit with an AC source we can define the voltage and resulting current as the complex functions:

$$V = |V|e^{i\omega t}$$

$$I = |I|e^{i(\omega t + \phi)}$$

Similar to Ohm's law, we can then define impedance as

$$Z = \frac{V}{I} = |Z|e^{i\phi}$$

where ϕ is the phase between the AC voltage and resulting current. It can be useful for analysis to use the form

$$Z = Z' + iZ''$$

where Z' and Z'' are the real and imaginary components of the complex impedance. In the case of a series LCR circuit we can simplify this to

$$Z = R + iX$$

where R is the DC resistance and X is the reactance. The reactance comes from the capacitive and inductive circuit elements and is purely imaginary due to their current response being $\pm\pi/2$ out of phase with an applied AC voltage. In isolation we can define the capacitive and inductive reactances as

$$X_C = \frac{1}{\omega C}$$

$$X_L = \omega L$$

respectively.

An impedance analyzer works by outputting an AC voltage with a well-defined magnitude and frequency and measuring the amplitude and phase of the current response. This measurement is generally repeated through a broad range of frequencies. The frequency response of the circuit can then be used as a basis for a circuit model from which equivalent capacitance and inductance can be extracted.

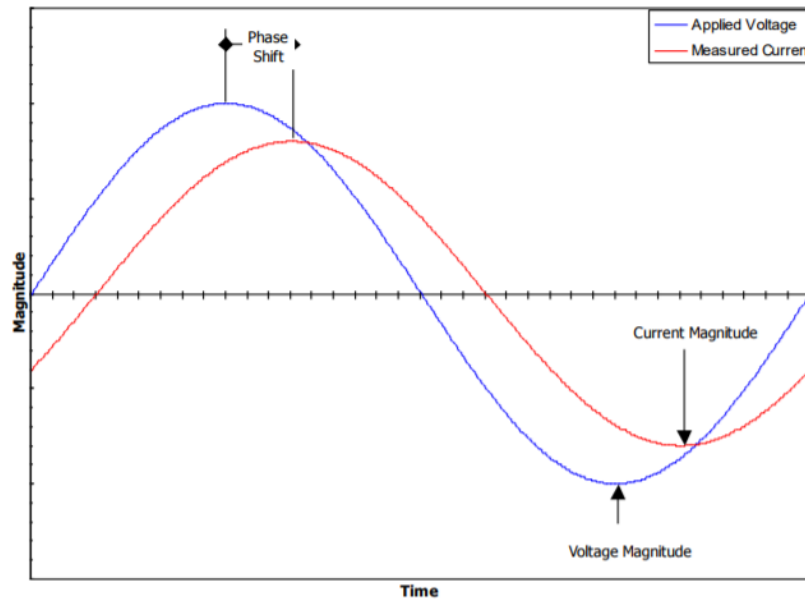


Figure 4.1: The basic characteristics of an AC impedance measurement. An applied AC voltage of well-known frequency and magnitude is applied to the sample and the resulting current is monitored. The current magnitude and phase shift are used to calculate the complex impedance terms, then usually fit to a circuit model relevant to the sample type.

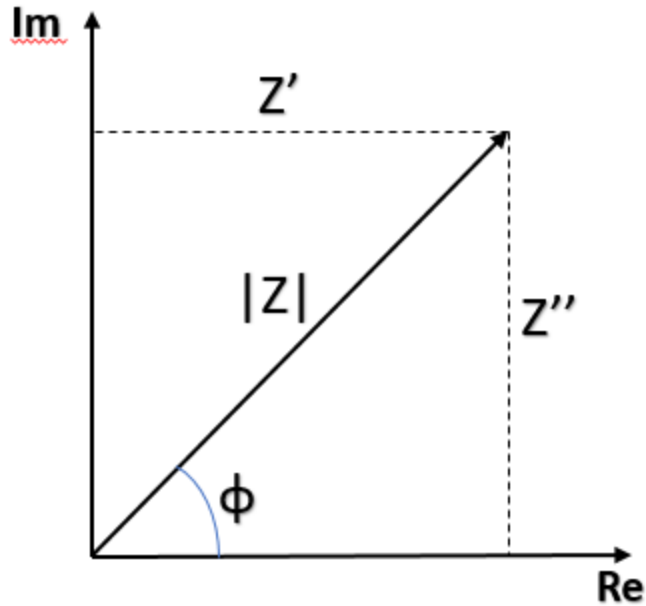


Figure 4.2: A representation of impedance on the complex plane. This diagram represents how to extract Z' and Z'' from a measurement of $|Z|$ and ϕ .

4.2. Impedance Model for VO₂(001) Thin Films

Impedance spectroscopy has been utilized to probe many material systems [46] which undergo a MIT or show other dynamic transport behaviors. For example, the technique has gained widespread use in biochemical sensor [47], fuel cell [48], and solar cell testing [49] applications.

VO₂ is an ideal candidate for IS analysis due to the underlying change in sample geometry as the film undergoes the MIT. As discussed previously, the MIT is generally characterized by the formation of metallic islands in an insulating matrix. In the films discussed in this section, epitaxial VO₂ of ~75nm thickness, there is evidence for the growth of metallic filaments which combine to form conductive channels near T_c . As discussed in Chapter 6 (noise spectroscopy) we can assume the film regions in the monoclinic phase have a resistivity several orders of magnitude higher than the rutile metallic filaments. Below and near the transition,

before a significant number of percolative channels have formed along the current direction, this geometry can effectively be modeled as a random resistor and capacitor network [50]. Post transition, where current can easily flow along metallic channels, the film should behave as an ohmic resistor with little reactive behavior. Thevenin's theorem shows that any linear electric network can be generalized to a single equivalent impedance. We therefore can treat the complex network in a simple parallel RC circuit model, with the resistive channel representing the combined contributions of the conductive metallic channels and tunneling between metallic regions and the capacitive channel representing the charge storing characteristics of neighboring metallic regions separated by the insulating matrix. The equivalent capacitance can therefore provide information about the sample wide growth of metallic domains and filaments. As C should increase with both the increase of filament cross-sectional area and the decrease of filament spacing, we can expect a rapid growth in C near the T_c . As the metallic filaments combine to complete conductive channels, the sample capacitance should be effectively nullified.

To derive the impedance model for this circuit, we can utilize the fact that voltage will be equivalent for the R and C channels and equal to the total applied voltage for the DUT, while the currents may vary for each channel. We can solve for I in the complex form of the impedance

$$I = \frac{V}{R} + i \frac{V}{X_c}$$

and as V is equivalent in both channels, we can use the definition of impedance to simplify this form to

$$\frac{1}{Z} = \frac{1}{R} + i \frac{1}{X_c}$$

Solving for Z we find

$$Z = -\frac{iRX_C}{R - iX_C} = \frac{RX_C^2}{R^2 + X_C^2} - \frac{iR^2X_C}{R^2 + X_C^2}$$

To determine the general behavior of this type of circuit, we can apply the complex conjugate to derive the magnitude of impedance

$$|Z| = \frac{RX_C}{\sqrt{R^2 + X_C^2}} = \frac{R}{\sqrt{4\pi^2 C^2 R^2 f^2 + 1}}$$

From this final form we can easily describe the main features of the impedance curve. At the DC limit, $f = 0$ Hz, our impedance will match the DC resistance. In most films C is several orders of magnitude lower than R , and will remain effectively flat with frequency, up until around one order of magnitude to the cutoff frequency, f_c , defined as

$$f_c = \frac{1}{2\pi RC}$$

at which point the impedance will decrease continually with frequency, until system dependent inductive contributions become significant (usually near the 10 MHz range). These features can be seen in Fig. 4.3 where the R and C values have been chosen as 1 MOhm and 1 pF, which fall within the expected range seen in thin VO_2 films; the cutoff frequency (approximately 159kHz) is marked in red.

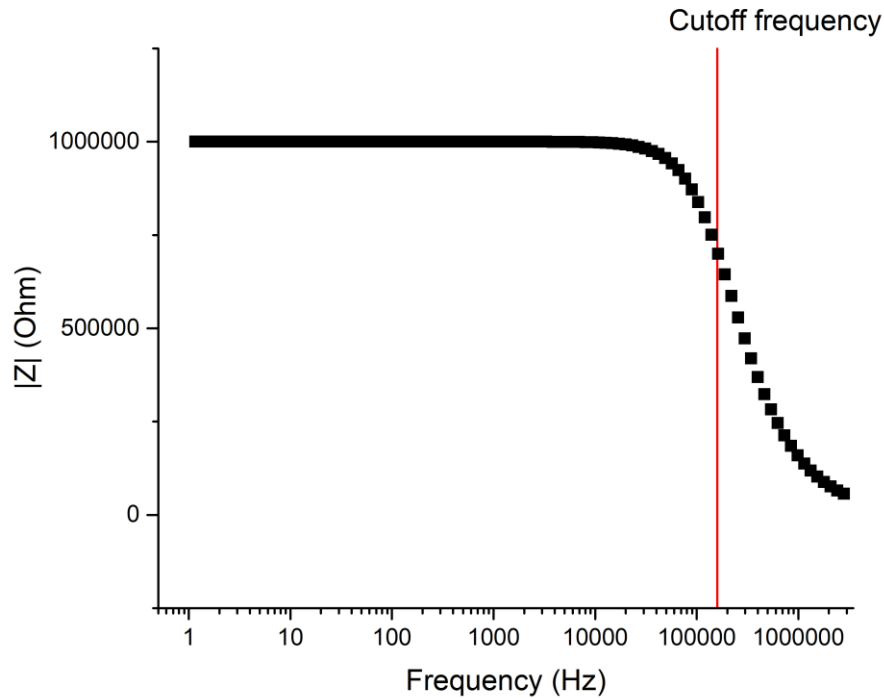


Figure 4.3: A simulated impedance spectrum for an example parallel RC circuit ($R = 1 \text{ M}\Omega$ and $C = 1 \text{ pF}$) of similar component values to a VO_2 thin film. We can see the nearly flat frequency response up to the cutoff frequency before capacitive reactance begins to dominate.

While these simple calculations are useful to roughly determine the validity of using the parallel RC model based on initial experimental data, in practice we will be using a commercial impedance analyzer software (*Zview*) to include corrections for the system components and cabling as well as to test more complex circuit models, such as including inductive elements related to filament growth.

4.3. Measurement System and Error Estimation

The measurements were taken using an HP 4284A precision LCR meter (now a Keysight Technologies system). This meter has a frequency range of 20 Hz to 1 MHz with a $\pm 0.01\%$

accuracy and a measurable impedance range of 0.01 m Ω to 99.9 M Ω . As with most benchtop LCR meters, this system is capable of directly measuring sample capacitance utilizing internal series and parallel circuit models, with a functional range of 0.01 fF to 9.99 F. For samples with total impedance of >10k Ω the parallel mode is generally implemented.

It is essential to determine the accuracy of the extracted sample capacitance values as the total measured capacitance will be dominated by system and cabling contributions in our region of interest. This is especially important near T_c , where the sample capacitance should rapidly drop below the system minimum capability. In order to obtain a measurement of sample capacitance during the transition, the sample contribution must be higher than the percent accuracy of total impedance.

The HP4284A manual provides specifications for determining the accuracy of C for a given sample impedance and voltage range. Absolute accuracy includes both relative and calibration accuracy contributions, but in general the calibration accuracy term will be effectively zero when proper measurement procedures are followed. These procedures include a 30 minute warm up period, using short cable lengths (sub 1m), open and short circuit corrections, reasonable test signal voltage (impedance dependent), and optimal measurement range selection. As these procedures were all followed for our measurements, we can approximate our absolute accuracy from the provided relative (basic) accuracy for our measurement specifications. Fig. 4.4 shows the basic accuracy (A_{t1}) for our measurements, which is 0.1% for a test signal voltage of 0.1 V_{rms} with medium or long integration time.

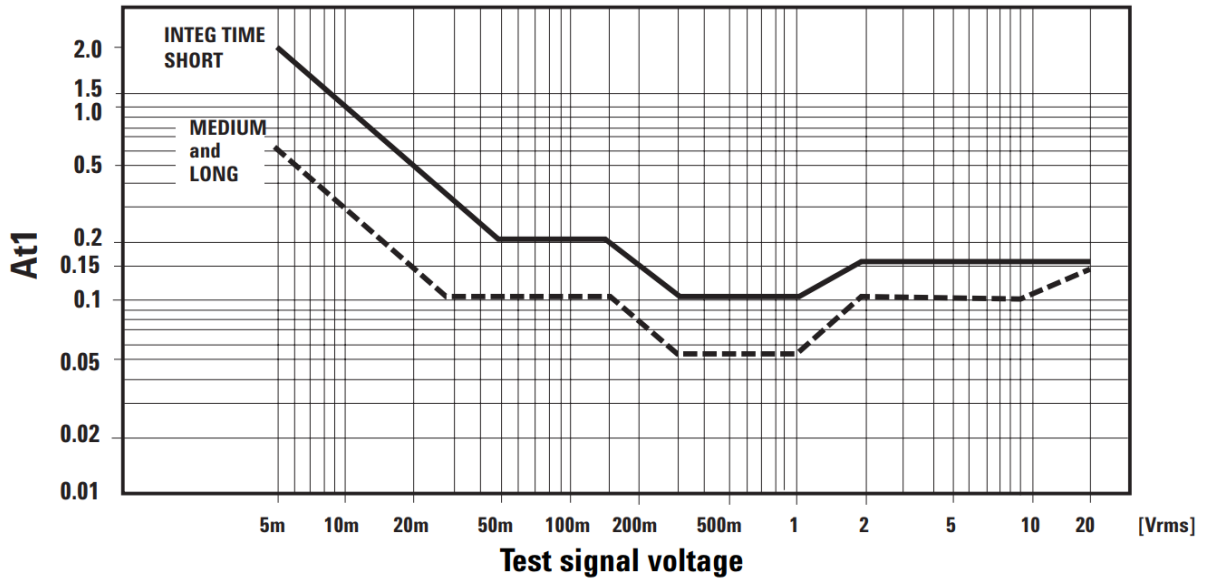


Figure 4.4: The sensitivity profile of the HP4284A LCR meter [51]

These meter level C measurements use discrete frequencies instead of utilizing a range of frequency values. The error in C can be reduced by increasing the integration time, but still assumes an ideal parallel RC response from the sample. Therefore, the equivalent C values, while accurate to $\pm 0.1\%$ over a broad range of impedances, are valid only at the frequency used for data collection.

As the standard IS procedure involves collecting a complex impedance measurement for many tens or hundreds of frequencies for each sample, one could easily assume the increased statistics would allow for a higher accuracy in the extracted C [52]. From actual VO₂ thin film impedance data we can see there is some deviation from an ideal RC response, even after system and cabling contributions are removed. This deviation is difficult to model and is variable between samples as it is likely due to a combination of defects and nonlinear transport behavior. Attempting to fit this data to the ideal RC model generally results in an error close to the expected basic accuracy for measurements below T_c (as low as 0.05%) but can significantly increase above the MIT as the reduced sample capacitance provides little reactive contribution

within the measurable frequency range. Above T_c the fitting error can exceed 2%, making the extraction of sample contributions impossible. With these limitations in mind, we will estimate the error in C to be equivalent to the fitting error of the ideal parallel RC circuit model.

4.4. Methodology

Thin films of VO_2 were grown onto TiO_2 (001) substrates. (001) films were chosen due to having the largest transition magnitude in comparison to (100) and (110) films [34] [32]. Film thickness was confirmed with XRR to be 75nm. Additional details of the characterization can be found in Chapter 3. The samples were mounted with thermal grease to the copper heating block of a LabView controlled heating system with low-overshoot capabilities (see Chapter 2). The samples were wire bonded at two points (spaced 3mm) to copper pads on the heater mount. The mount was inserted into a homemade breakout box and shielded by a thick steel covering for thermal stability. Two 1 ft BNC cables connected the breakout box to the 4284A LCR meter.

The LCR meter was controlled by a custom LabView program which included fully automated data collection. The test voltage was set to 100 mV with a frequency range of 100 Hz to 1 MHz with the total number of measurement frequencies set to 100. The controller program allowed a temperature measurement range of 300 K to 400 K for both heating and cooling cycles. (For our purposes, a heating cycle is defined as a series of impedance measurements where each subsequent run is performed at a temperature higher than the previous measurement temperature, generally beginning the series at a temperature below T_c and ending at a temperature above T_c . A cooling cycle is similarly defined moving from high to low temperature between subsequent measurements.) For heating cycles the sample is reset to 300 K between each run; the cooling cycles have reset temperature of 400 K. For all measurements, upon the

stabilization of the setpoint temperature, impedance spectrums were collected continuously for several hours. The measurement period was 2.5 hours for all runs. As each impedance spectrum took 3 minutes to collect, these periods represent 51 impedance spectrums per temperature step.

Only cooling cycles were utilized in this experiment due to the lack of capabilities to fully reset the sample to the low temperature state between runs. As discussed previously, the persistent metallic domains make a sub room temperature reset cycle essential for repeatable results. The available PPMS systems had stray capacitances in the nano to micro F range, making extraction of the sample capacitance impossible with these set-ups.

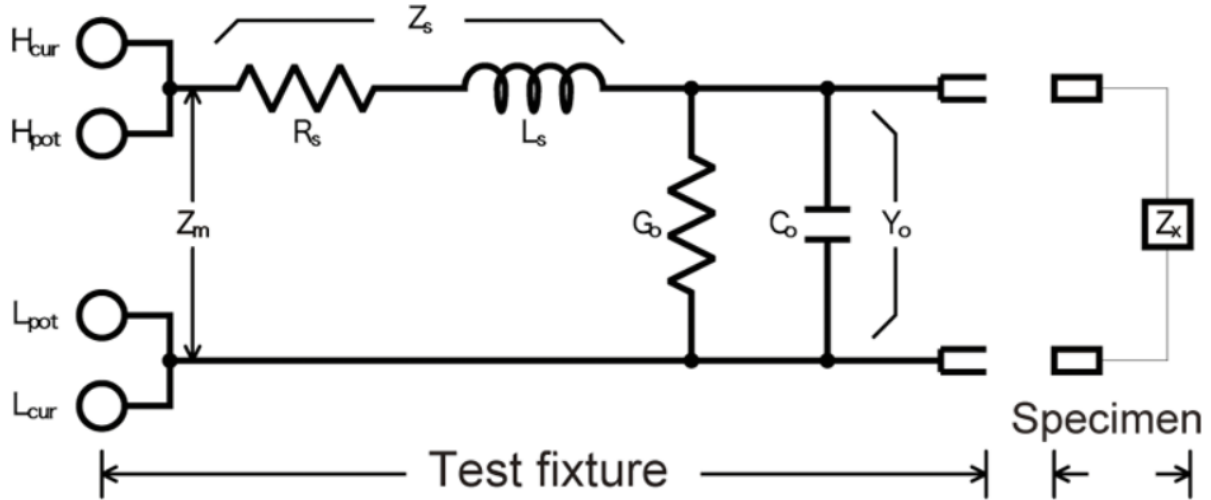


Figure 0.5: The equivalent circuit model of the system and cabling contribution to the impedance response. The Z_s elements are fitted by taking a shorted measurement; the Y_0 elements are fitted from an open circuit measurement. [53]

To determine system and cabling contributions, shorted and open measurements were performed and fit to a standard calibration model seen in Fig. 4.5. The shorted measurement only contains contributions from the series resistor and inductor (Z_s) while the open test is dominated by the parallel resistor and capacitor (Y_0). The extracted values for Z_s were $L_s = 2.70e-7$ H and $R_s = 0.37 \Omega$. In our frequency and sample impedance range these have a net contribution below the meter's relative accuracy and will therefore not be included in the modeling. G_0 was found to

be effectively infinite and is also disregarded from our modeling. C_0 was generally on the order of $1.5e-12$ F, but was found to be highly sensitive to the specifics of the sample mounting, orientation and proximity of the cabling within the breakout box, and the geometry of the bonding wires. As this was highly variable between samples, to more closely approximate the net system contribution, an equivalent system capacitance (C_0) was extracted by taking a mounted VO_2 sample, heating it to a temperature well above T_c (~ 400 K) and extracting the equivalent capacitance. We can justify this extraction method by noting that the system and sample capacitances are in parallel, and with therefore simply sum to give us the net capacitance.

The collected data was analyzed using Zview, a commercial impedance analysis software. The major benefit of this software was the batch fitting capabilities, which helped speed up the processing of the nearly 1000 impedance spectrums collected during the experiment. The software also allowed for the efficient testing of alternative circuit models and calibration. As compared to some previous works on modeling the impedance spectrums of VO_2 films [54] [55], we found that it was not necessary to include additional circuit elements aside from the parallel RC channels. For example, attempting to extract the inductance contribution due metallic filament formation produced equally high-quality fits for values of $L = 0$ H and 0.3 H, the latter representing an unphysically large value for a thin film, making any estimation of inductance invalid within our frequency range. Equivalent R and C were extracted for each spectrum, which was then plotted in OriginLab and fit with the proper model for time dependence, as discussed below.

4.5. Impedance Analysis of VO₂ (001)

In Fig. 4.6 we show a Bode plot of several raw impedance spectrums for measurements taken before and after the MIT. The pre-MIT spectrums show nearly ideal parallel RC behavior, with a flat frequency response up to the cutoff frequency followed by a log(f) decrease in $|Z|$. The high frequency regime for the 315 K, 319 K, and 325 K datasets nearly overlap at this scale due to the stray system capacitance dominating the sample capacitance contributions at all temperatures. Post T_c data shows a nearly flat frequency response in our range of interest.

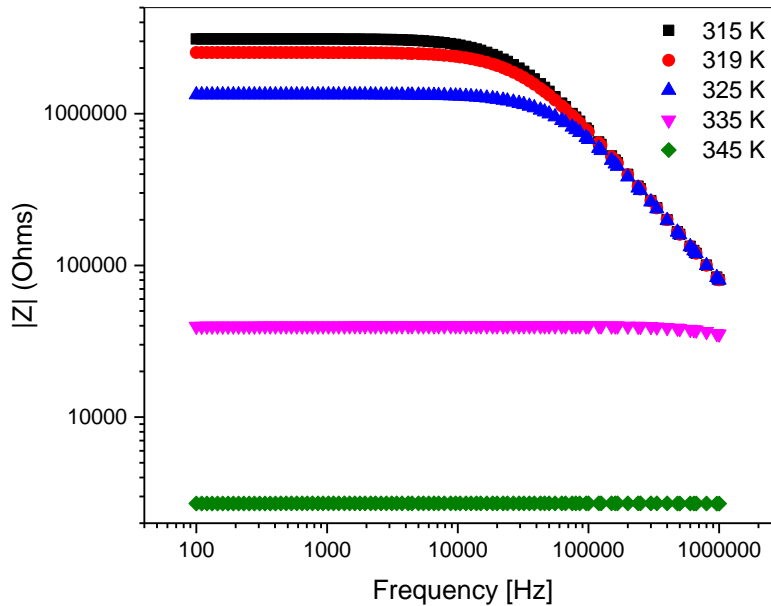


Figure 4.6: A Bode plot of several impedance spectrums taken before, during, and after the MIT. Low temperature measurements show the typical parallel RC profile presented in Figure 1. High temperature measurements increasingly flatten within our frequency range as the system becomes more metallic and loses its capacitance characteristics.

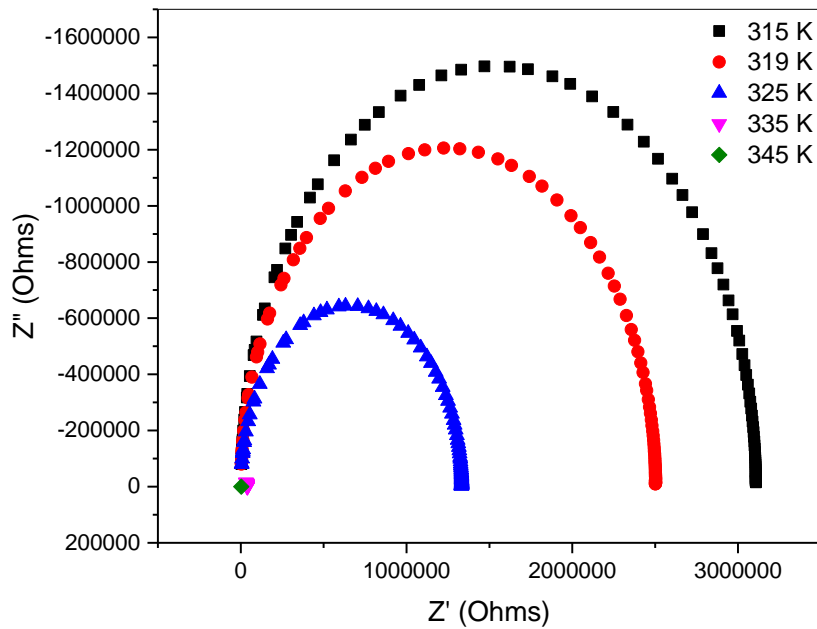


Figure 4.7: Nyquist plots of the same measurements. In the low temperature monoclinic state our films show the typical semi-circular line shape characteristic of parallel RC circuits. Upon the metallic transition, the semi-circles collapse very near to a point along Z' that matches the sample DC resistance.

The Nyquist plot (Z'' vs Z') for the same data series is presented in Fig. 4.7. The semi-circular shape is indicative the smooth transition from a resistive to reactive circuit response seen in a parallel RC circuit. After the MIT the datapoints collapse around a Z' value near the sample resistance with little extension into the Z'' axis. This behavior parallels the flat response for these temperatures seen in the Bode plots.

The data collection resulted in 969 impedance spectrums, which were batch fitted using the ZView impedance analysis software. The fitting model, as described above, provided excellent fits for all datasets. The extracted resistances showed a clear long-timescale increase which continued to rise well past the 2.5 hour measurement period at each temperature step (Fig.

4.8), with no saturation observed after a maximum measurement period of 10 hours. The magnitude of the resistance drift across all temperatures is plotted in Fig. 4.9. The effect peaks near T_c (337 K for these samples). The magnitude of drift follows a nearly Lorentzian trend, with a FWHM of ~ 12 K. The resistance drift is readily detectible well above and especially below T_c , providing further evidence for the continued existence of metallic domains near room temperature.

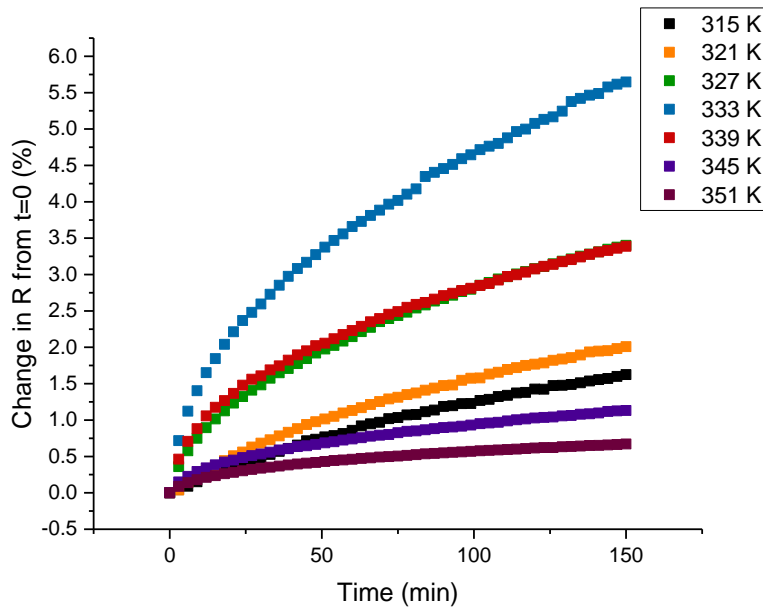


Figure 4.8: Fitted DC resistance drift plotted as a function of the settling time. The drift seems to maximize around T_c . The resistance drift effect continued well past the 2.5 hour measurement period, with no indication of settling even after 10 hours of measurement time.

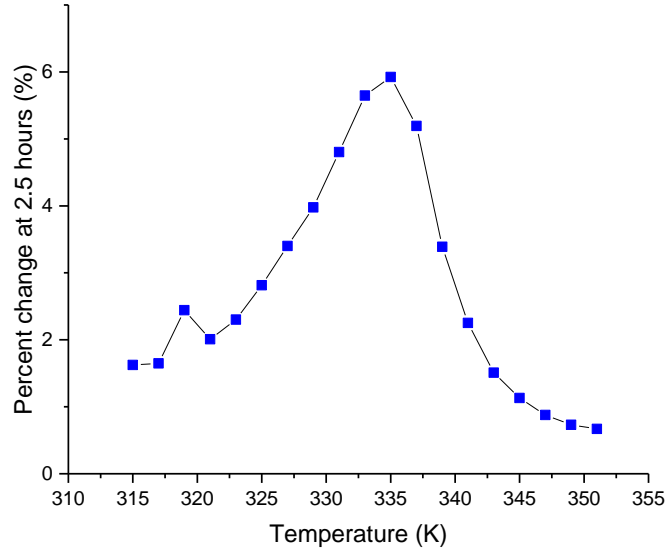


Figure 4.9: Resistance drift magnitude (at 2.5 hrs) plotted vs settling temperature. The effect peaks very near T_c .

The $T = 0$ capacitance is plotted in Fig. 4.10 for all temperatures. As expected, the capacitance peaks near T_c and is associated with the densely packed metallic islands separated by short insulating regions that form upon reaching the MIT. We can see that above T_c , when the metallic islands are mostly formed into continuous conductive channels, C rapidly drops with increasing temperature. An unexpected feature is the slight dip in C between room temperature and T_c . This could possibly be due to an increased percolation rate in this temperature range leading to the rapid growth of conductive channels, shorting some regions contributing to C . As this is a complex transition with multiple competing processes, simulations would likely be needed to fully interpret this behavior.

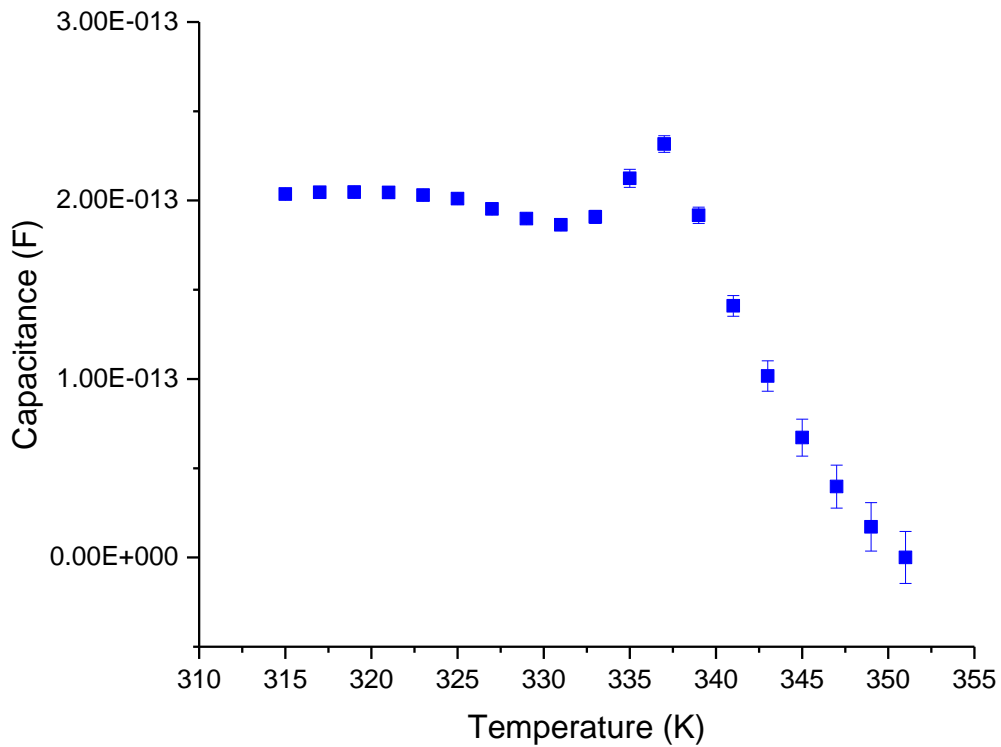


Figure 4.10: Temperature dependence of the fitted values of C . C peaks very near T_c , before falling to effectively zero after entering the metallic phase. The distinct dip in C in the region below T_c could be due to interfilament growth shorting isolated metallic regions.

We then attempted to model the time dependence of the resistance drift. We plotted resistance drift percent vs $\log(t)$, a dependence that would be expected for a system with a uniform distribution of energy barriers to transition [56]. This data is shown in Fig. 4.11. It is clear that below around 10^4 s the trend shows significant nonlinearity. Above this time, the resistance shows nearly linear behavior with respect to $\log(t)$. This would indicate the at least two processes of relaxation occurring simultaneously with two distinct timescales. Fig. 4.12 shows of an example data set (337 K) fit to both single and double exponential decay functions. The single decay function provided an R-square of 0.987 while the double decay function's R-

square was 0.9995. This double decay model for resistance drift has also appeared in other phase change systems [57] [58].

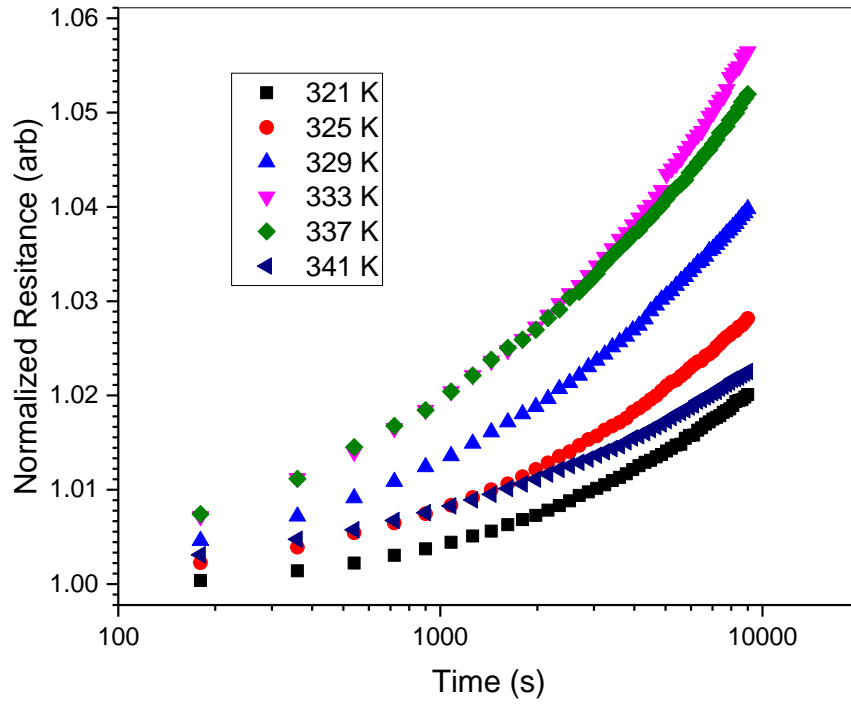


Figure 4.11: The time dependence of the normalized resistance for several temperatures in the region of T_c . A clear non-linearity appears when plotted versus $\log(t)$ indicating the presence of multiple relaxation processes.

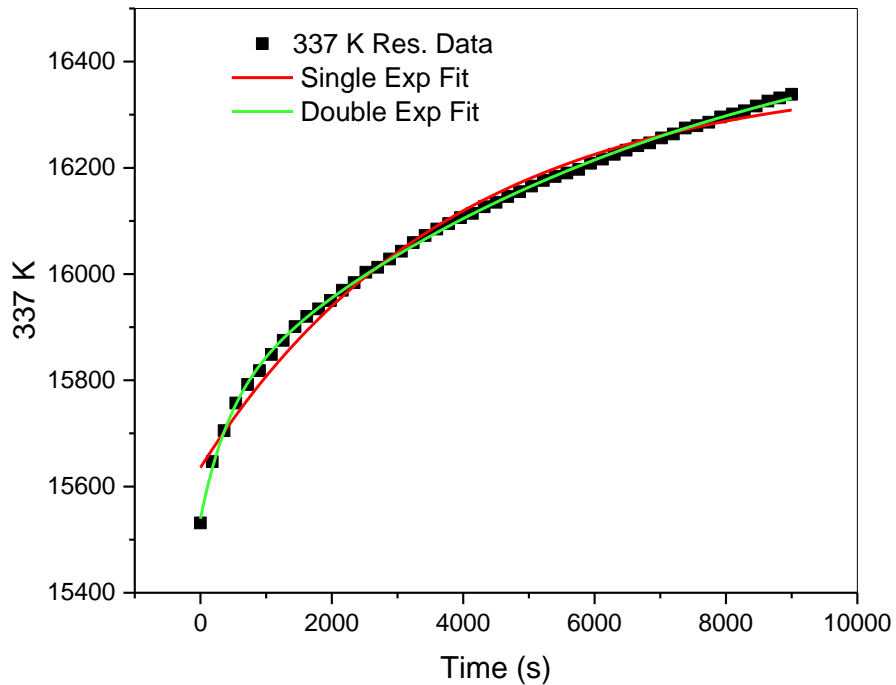


Figure 4.12: Time dependent resistance for the 337 K settling temperature fit with single and double exponential decay functions. The double decay function provides a superior (R -square > 0.995) fit for all measurements.

As fit quality will always increase by adding additional fitting parameters, it was necessary to justify the second exponential with some physical process. As we know the resistance should not only track the metallic domain population but also the domain geometry, it is reasonable to assume that the sample capacitance should track at least one of the relaxation processes. Fig. 4.13 shows the C vs time for 335 K. For all measurements error in C greatly outweighs the magnitude of the drift. Though this is an issue for determine the drift to a high accuracy, it is not uncommon in IS experiments to obtain signals with magnitude on the order of the measurement error. In these cases, a high measurement precision is assumed and many measurements are taken at each frequency to improve the extraction capability.

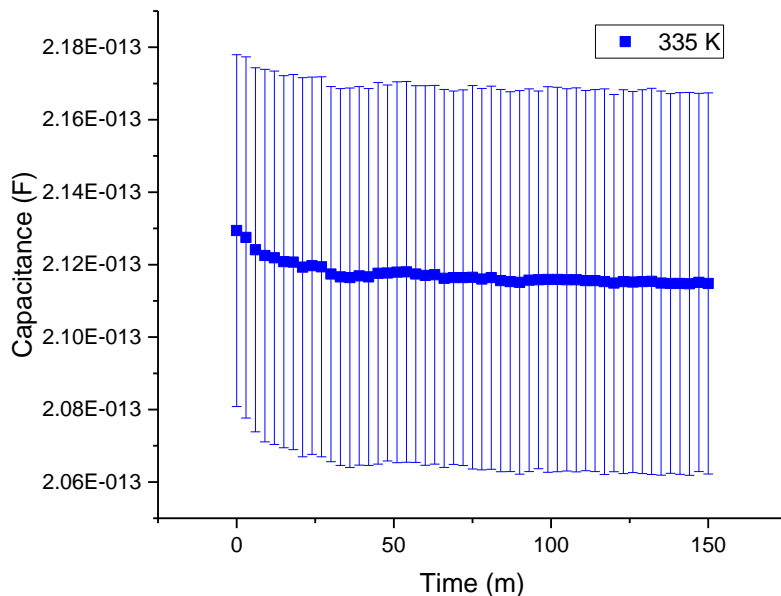


Figure 4.13: Extracted capacitances of the 335 K settling temperature overlaid with the fitting error margins for measurement accuracy.

Though the measurement accuracy for our samples is limited to a few fF, we can safely assume the measurement precision is a several orders of magnitude lower than this value, on the order of 0.1 fF (Fig. 4.14). This was confirmed by measuring a high-quality reference capacitor over a 5 hr timescale, which upon analysis showed a standard deviation 3 orders of magnitude below the basic accuracy. This was further confirmed by repeating the VO_2 impedance tracking measurement at a stable room temperature after a 24 hr settling period. These measurements showed no evidence of long timescale variation in either R or C, again with standard deviation much less than the basic accuracy.

With this in mind, we can fit the extracted values for C to an exponential decay function to determine the time dependent variation of this parameter without being able to determine the absolute magnitude of the transition within each range. This allows for comparison of the

timescale of relaxation in the capacitance to the secondary process extracted from the resistance fits.

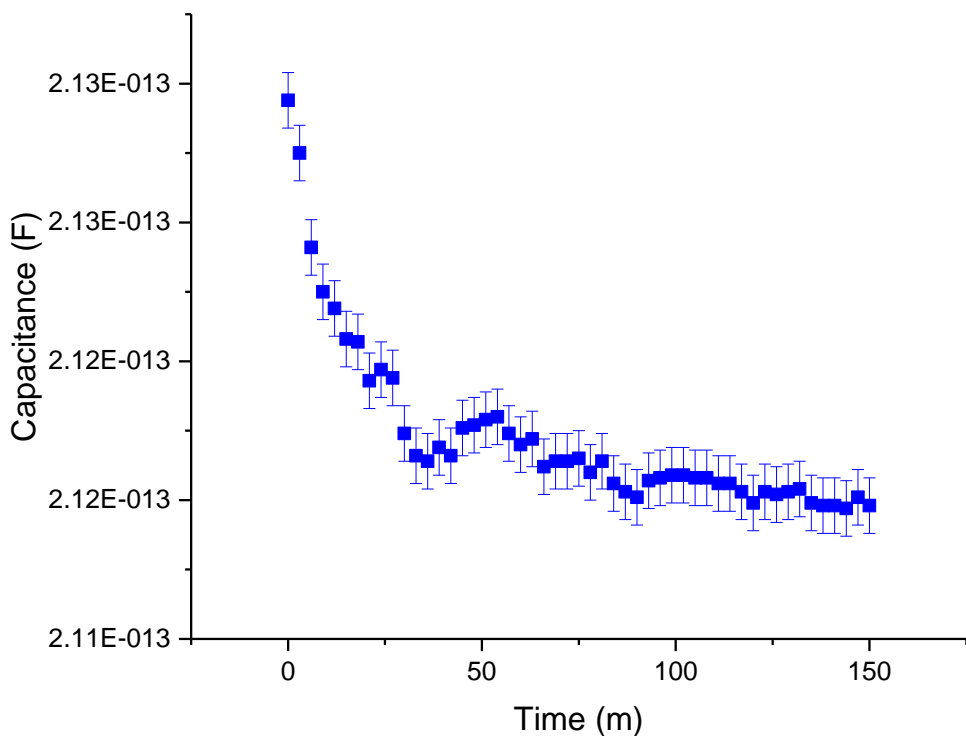


Figure 4.14: The same C data overlaid with the estimated fit precision. We can conclude our fits provide evidence of long-timescale decay in capacitance.

The time dependent C values showed good agreement to the single decay model (R-square of 0.996 in the 323 K example, Fig. 4.15). In most cases C dropped 2-5% within the first hour of the measurement and showed very little time dependence after this period.

The extracted time constants for all measurement are plotted in Fig. 4.16. t_1 and t_2 for the resistance fits show two clearly distinct and consistent timescales, with the first and second processes having timescales of $\sim 10^2$ - 10^3 s and $\sim 10^4$ - 10^5 s respectively. The extracted timescales for C are plotted in the same figure. The t_1 capacitance values clearly overlap with the first

resistance relaxation process for all temperatures. In most cases above T_c , the drift in C was too small to obtain a meaningful fit and was therefore not included.

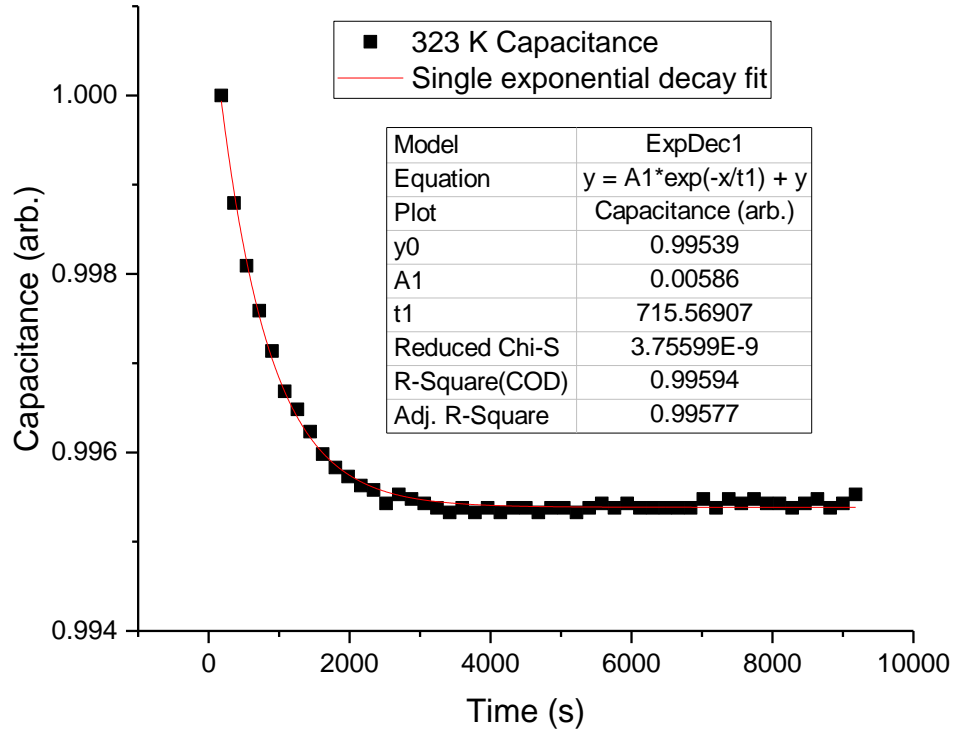


Figure 4.15: Time dependent capacitance of the 323 K settling temperature measurement fit to a single exponential decay function.

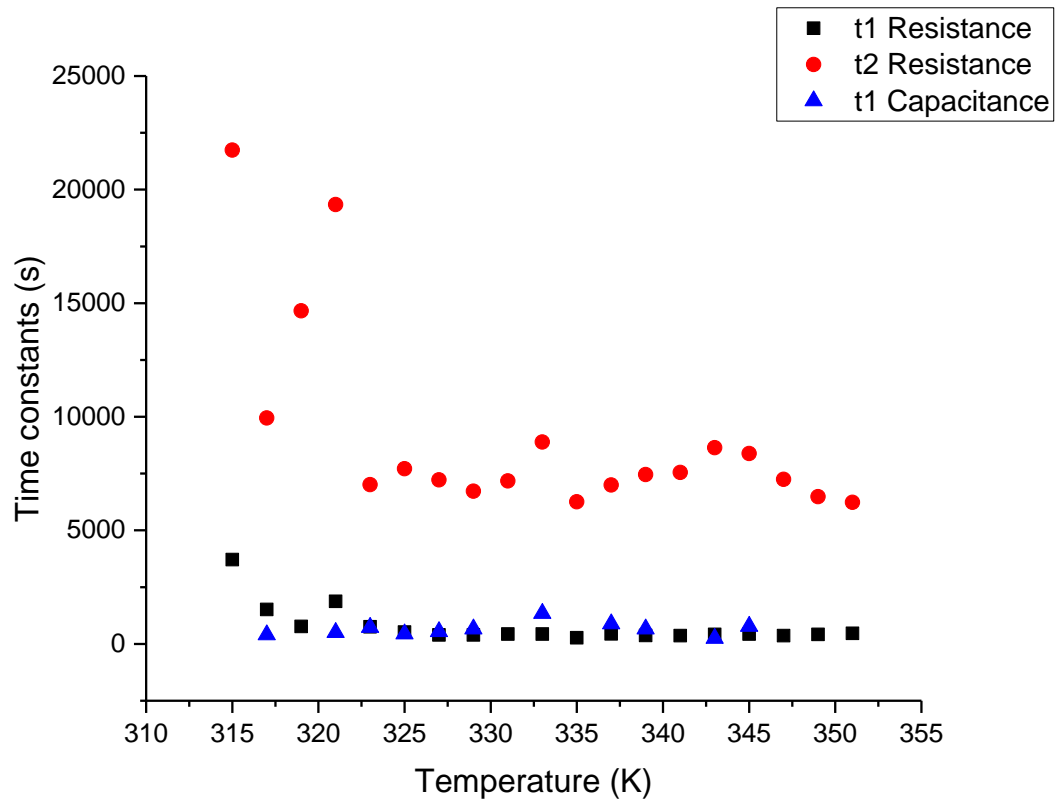


Figure 4.16: The fitted values for the R and C decay time constants for all settling temperatures. The t1 time constants for R and C show a very strong correlation, possibly indicating identical physical origins.

4.6. Discussion

The above analysis shows strong evidence for the existence of multiple relaxation processes in VO₂ films during the MIT. The longer timescale process affecting the transition has been studied previously and, as mentioned above, is generally attributed to the existence of a distribution of transition barriers.

Due to the lack of cooling capabilities, systematic measurements were not taken through heating cycles. In spite of this system limitation, a short series of heating runs were collected to very roughly gauge the time dependent behavior of R and C. Surprisingly, in both cooling and

heating cycles the capacitance decreases over the measurement period. This would suggest that the change in C is not controlled solely by the formation (or loss) of metallic domains, as this would cause heating and cooling cycles to have time dependencies of opposite signs. Instead, as the sample is settling at the setpoint temperature, the decrease in C is likely caused by the newly formed metallic domains coalescing into larger metallic regions, similar to Ostwald ripening [59]. This would have net effect of increasing the average domain separation and decreasing the total domain area, resulting in a decrease in capacitance. This process should be equally viable in cooling cycles where rutile metallic islands are transformed to insulating monoclinic regions separated by gradually decreasing volumes of metallic domains.

Regarding the resistance drift, it is obvious that a net increase of metallic regions in the sample would decrease the resistivity, but it is not as clear why the capacitance would be mostly unaffected. This could be related to the different distance scales defining capacitance and tunneling (which would be the primary transport mechanism in the interstitial regions). As the tunneling probability between metallic domains should be proportional to e^{-x} , the formation of very small domains between neighboring metallic islands would have a significant effect on transport probability while only minimally contributing to capacitance due to their small surface area. As many of the domains forming during the measurement period would be spaced far from the large metallic islands, they would have a low probability of merging with the larger regions, resulting in a stable increase of conductivity.

This measurement could be greatly improved by reducing the stray capacitance of the measurement set-up, as well as implementing proper cooling capabilities to allow for heating cycles to be executed with a full sample reset. There is no guarantee that the relaxation dynamics would match for both heating and cooling at all temperatures [60].

More generally it is interesting to note that while the long timescale resistance drift has been characterized by others for VO₂ thin films, and the necessity of fitting with two exponential decay functions has been described in other phase change materials, it seems that no other works have defined a relationship between the capacitance relaxation and first resistance relaxation process timescale. It may be the case that this is a universal relationship in metal-to-insulator transition materials.

In summary, we have collected time dependent impedance spectrums for thin films of VO₂ as they were kept at a series of highly stable temperatures after cooling from well above T_c. We justified using a parallel RC circuit model to fit these films. The drift in the extracted resistances was found to be defined by two relaxation processes of distinct timescales, one of which closely matches the timescale found in the drift of the sample capacitance. We proposed that the process trending with the capacitance drift is related to small metallic domains congregating into larger metallic islands in a process similar to Ostwald ripening. The second process is likely due to the random formation of metallic domains within the insulating interstitial regions due to the presence of a broad distribution of energy barriers to transition.

CHAPTER 5:
HIGH TEMPERATURE FERROMAGNETIC RESONANCE STUDIES OF
VO₂(110)/Ni₈₀Fe₂₀ HETEROSTRUCTURES

It has recently been shown that the magnetization relaxation properties of ferromagnetic materials can be significantly modified when deposited in multilayers with materials that undergo a phase change [61] [62] [63]. This has been described in detail for Ni₈₀Fe₂₀ (Permalloy, or Py) and Gd bilayer structures that have been cooled through the Gd Curie temperature to induce a paramagnetic-to-ferromagnetic phase transition. Ferromagnetic resonance (FMR) studies of these heterostructures showed clear temperature dependencies on the gyromagnetic ratio (γ), effective magnetization (M_{eff}), and the effective Gilbert damping parameter (α_{eff}). The modification of the damping is of particular interest here as the enhanced damping with decreasing temperature could be directly attributed to increased spin pumping into the Gd layer. In the Py/Gd system this spin pumping enhancement was linked to the decrease in the spin diffusion length (λ_{SD}) upon the FM transition as well as a peak in the spin mixing conductivity near the Gd Curie temperature.

As VO₂ shows a dramatic increase in conductivity (10^{-1} to $10^3 \Omega^{-1}\text{cm}^{-1}$) through the MIT, as well as sharp increase in the magnetic susceptibility at T_c , [21] we can reasonably suggest VO₂/Py bilayers as a candidate system for temperature dependent FMR studies. As the spin pumping contribution should be directly proportional to the spin mixing conductance [64](see

below), which should be enhanced dramatically upon the MIT [65], it could be reasonably predicted that the effective damping parameter should be modified upon the MIT.

In this chapter we describe the details of the broadband FMR system with a modified high temperature controller. We describe the deposition and characterization of a series of VO₂/Py bilayers with variable Py thickness to isolate effects due to interfacial origins. We then examine the temperature dependence of the linewidth broadening in the context of the spin pumping to determine if the VO₂ layer behaves as an effective spin sink in the metallic phase.

5.1. FMR Technique

The theoretical treatment of the magnetization dynamics of FM films begins with the Landau-Lifshitz-Gilbert (LLG) equation [66]

$$\frac{d\mathbf{M}}{dt} = -\gamma'\mathbf{M} \times \mathbf{H} + \frac{\alpha\mathbf{M}}{|\mathbf{M}_s|} \times \frac{d\mathbf{M}}{dt}$$

where \mathbf{M} is the film magnetization, \mathbf{M}_s is the saturation magnetization, γ' is gyromagnetic ratio, and \mathbf{H} is the effective field, which is the sum of the external field from the electromagnet, the microwave field, and all anisotropy contributions. Kittel derived a general form for the resonance condition

$$\omega_0 = \gamma' \sqrt{[H_z + (N_y + N_y^e - N_z)M_z] \times [H_z + (N_x + N_x^e - N_z)M_z]}$$

where N_y and N_x are demagnetization factors (corresponding to the shape anisotropy) and N_y^e and N_x^e are effective demagnetization factors (determined from an equivalent field derived from

the magnetocrystalline anisotropy energy) [67]. This general form assumes a static magnetic field applied in the z-direction and an alternating microwave field in the x-direction.

The derivation of the FMR resonance condition was further simplified by Smit and Beljers [68]. Their formulation is also based on the LLG equation but does not require determination of demagnetization factors, which can be quite challenging to calculate for all but the simplest geometries. The resonance is given by

$$\left(\frac{\omega}{\gamma'}\right)^2 = \frac{1}{M_s \sin^2 \theta} \left[\frac{\partial^2 F}{\partial \theta^2} \frac{\partial^2 F}{\partial \phi^2} - \left(\frac{\partial^2 F}{\partial \theta \partial \phi} \right)^2 \right]$$

where F is the free energy. For a thin film, θ is the angle between the magnetization and film normal.

In this experiment, where we will be probing thin film systems with single FM layers in the in-plane geometry, our treatment simplifies greatly to the following form [69]

$$f = \gamma' \sqrt{H_{res}(4\pi M_{eff} + H_{res})}$$

where the effective magnetization is defined as

$$4\pi M_{eff} = 4\pi M_s - \frac{2K_u}{M_s}$$

where K_u is the uniaxial anisotropy term.

To model the magnetization relaxation we will be interpreting the frequency dependent linewidth following the Gilbert formulation

$$\Delta H = \Delta H_0 + \frac{2}{\sqrt{3}} \frac{\alpha_{eff}}{\gamma'} f$$

where ΔH_0 is the extrinsic damping term responsible for the zero-frequency linewidth and α_{eff} is the effective Gilbert damping parameter generally dominated by intrinsic damping contributions, though also influenced by interfacial effects such as spin pumping, as described in the next section.

5.2. Spin Pumping

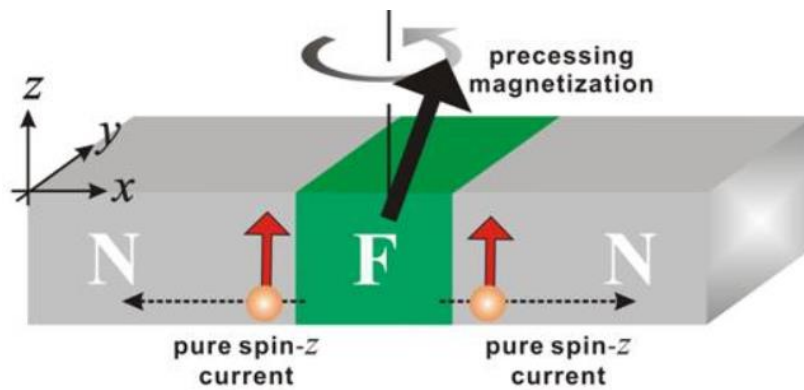


Figure 5.1: A schematic of a spin pumping experiment, where the precession of the FM layer injects spin polarized current into neighboring metallic layers. [70]

Spin pumping is an interfacial magnetic relaxation effect [64] [71] where magnetic precession in the FM layer produces a spin current in neighboring metallic layers. The spin current can be produced in both normal metallic or magnetic layers, though FM spin sinks can exhibit enhanced damping characteristics due to the asymmetry in the DOS for majority and minority spin polarizations.

The spin pumping effect appears in the effective damping term as [64]

$$\alpha_{eff} = \alpha_0 + \alpha'$$

where α_0 is the intrinsic damping term and α' is the spin pumping damping contribution. We can write this contribution as

$$\alpha' = \frac{\hbar \gamma g^{\uparrow\downarrow}}{4\pi M_s S t (1 + g^{\uparrow\downarrow} \beta)}$$

where \hbar is the reduced Planck constant, $g^{\uparrow\downarrow}$ is the spin mixing conductivity, S is the cross-sectional area, t is the FM layer thickness, and β is the back-reflection factor. This back-reflection factor is defined as

$$\beta = \frac{\tau_{SF} \delta_{SD}}{h} \coth\left(\frac{L}{\lambda_{SD}}\right)$$

where τ_{SF} is the spin flip time, δ_{SD} is the energy-level splitting factor, h is the Planck constant, L is the spin sink layer thickness, and λ_{SD} is the spin diffusion length [72].

From this theoretical treatment, we can expect a significant enhancement in the spin pumping damping contribution due to an increase in $g^{\uparrow\downarrow}$ as the VO₂ moves from the insulating to metallic state [71]. If a net increase in the effective damping is seen upon the MIT, this spin pumping origin can be confirmed by repeating the analysis with an increasing series of Py thicknesses. As α' is inversely proportional to the FM layer thickness, we can expect the effective damping enhancement to rapidly decline in heterostructures with increasingly thick FM layers.

5.3. FMR System Description

The resonance measurements were collected on broadband FMR system using a microwave source with a 1-65 GHz range. This wide frequency range is achieved with the use of a coplanar waveguide (CPW) sample mount. The CPW is impedance matched with the microwave cabling (50Ω) to maximize the microwave power reaching the sample. The output of the waveguide is connected to a diode microwave detector which outputs a voltage proportional to the absorbed microwave energy.

The mounted sample and CPW is placed in within an electromagnet capable of providing a static field up to 20 kOe. A Hemholtz coil provides a small (5-10 Oe) alternating field parallel to the static field orientation driven by a lock-in amplifier. The microwave source is set to the desired frequency and the external field is slowly swept. As the field approaches the resonance value, the microwave power absorbed by the sample will increase, resulting in a voltage drop from the diode detector. This voltage is fed into the lock-in amplifier which outputs the derivative of the detector signal. The use of the lock-in amplifier, as compared to directly monitoring the diode voltage with a GPIB multimeter, is beneficial due to the highly effective noise reduction which is necessary to accurately monitor the very small microwave absorption from thin magnetic films.

Sample heating was controlled by a modified version of the custom low-overshoot heater described in Chapter 2. Changes to the standard design included replacing the metal Joule heater with a ceramic version without magnetic leads and removing the copper heater block, which was found to interfere with the impedance matching of the CPW. The diode thermometer was replaced with a standard K-type thermocouple. Thermal contact between the sample and ceramic

heater was improved with the use of silver based thermal grease. The removal of the copper heating block, along with the limited ability for thermal isolation of the sample due to space constriction within the electromagnet, resulted in increased temperature instability with fluctuations up to 2 K under non-ideal conditions. As the hysteretic VO₂ films are highly sensitive to temperature near T_c, this heater solution was not capable of accurate control within the transition region. Therefore, resonance measurements were conducted twice for each sample: once at room temperature and once at ~385 K, far into the metallic state where fluctuations in temperature show little influence on the conductivity.

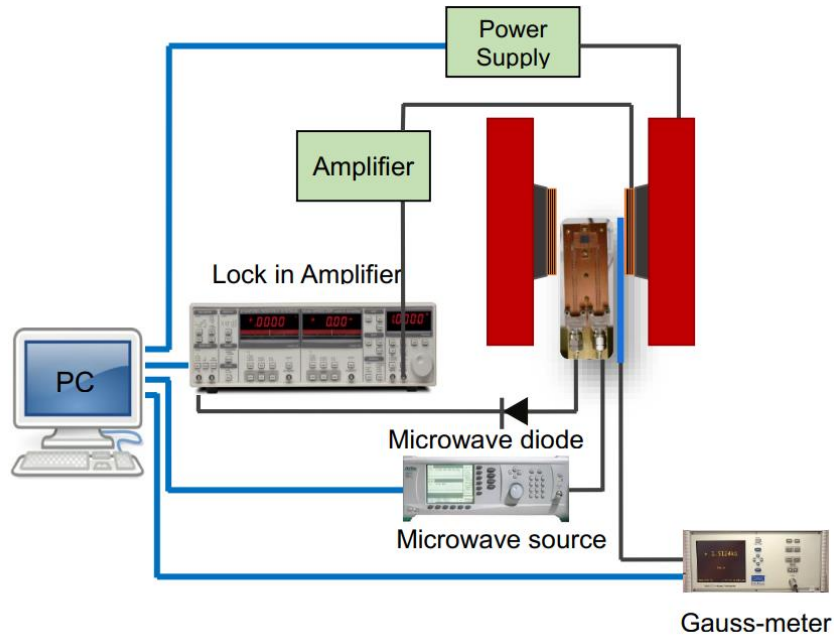


Figure 5.2: The components and basic design of the FMR system.

5.4. Sample Preparation and Methodology

Thin films of VO₂ were deposited on TiO₂ substrates with crystallographic orientation (110). The epitaxial quality of the films were confirmed with XRD measurements as shown in Chapter 3. XRR showed a film thickness averaging about 12 nm.

(110) substrates were chosen because they exhibited the lowest roughness (as compared to (100) and (001)) for all film thicknesses. In previous studies we had produced samples with a minimum roughness of 0.54 nm rms in very thin (110) films. By minimizing the growth rate with a reduced substrate temperature and precursor flux, along with a short 5 minute deposition time, we were able to consistently achieve films of 0.48 nm rms roughness. Detailed discussion of the VO₂ roughness calibration can be found in Chapter 3.

After CVD, the films were sputtered in the RASCAL magnetron sputtering system using high quality Py, Ru, and Al targets. In all samples a 3 nm Al capping layer was included to prevent oxidation of the Py layer upon removal from vacuum. After some initial test samples were produced and measured to determine the resonance quality, three separate film series were produced to systematically probe the spin pumping characteristics:

A: TiO₂/VO₂/Ru(3.3)/Py(6.5)/Al(3)

B. TiO₂/VO₂/Ru(2.3)/Py(t)/Al(3), where t = 4, 6, 10, 20 nm

C. TiO₂/VO₂/Py(t)/Al(3), where t = 6 and 20 nm

Ru was chosen as a seed layer for series A and B as it has been shown to enhance the Py quality when sputtering onto rough films. This step was found to only minimally contribute to the

resonance quality for our heterostructures as the FMR signal was of similar strength across all series.

5.5. Analysis

We first determined the transport characteristics of the heterostructures by performing a 4-point $R(T)$ measurement on a representative sample: a Py(6) film from series B. As seen in Figure 5.3, dR/dT changes sign near the expected value of T_c . The VO_2 layer resistance contribution can be determined by treating the sample as a bilayer with the Ru/Py/Al stack connected in parallel with the VO_2 film. As the metallic stack shows an expected linear dependence on R with increasing temperature, this can be fit to extract the stack resistance at our measurement temperatures of 300 K and 385 K, then further applied in a parallel resistance model to solve for the VO_2 layer resistance.

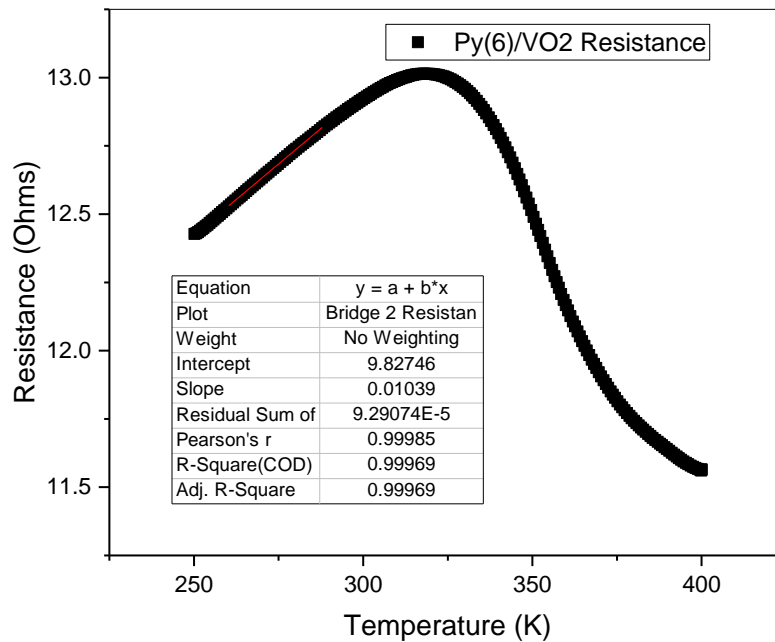


Figure 5.3: Temperature dependent resistance of Py(6)/Ru(2.3)/VO₂ through the MIT. The VO₂ film resistance contribution is estimated with the use of a parallel model. The linear fit of the low temperature region was used to model the high temperature resistance of the Py layer. The distinct decrease in R near T_c indicates the MIT is not inhibited by the additional sputtering steps.

We can confirm that the VO₂ resistance is on the order of $\sim 10^5$ for the 300 K measurement and drops to 65 Ω at 385 K. This result closely matches the temperature dependent resistivity measurements discussed in Chapter 3 and confirms that the VO₂ continues to show a ~ 4 order of magnitude MIT after sputtering additional layers on top of it.

Figure 5.4 presents the raw FMR resonance data for the series A sample. The clearly defined resonances seen in the figure were present in all measurements described in this chapter. The small shift in the field position as the temperature is increased to 385 K is expected given the temperature dependence on the M_s of Py. Figure 5.5 shows the corresponding frequency dependent linewidth results. A very small (3.7%) systematic enhancement of the damping parameter is observed, which naively could be attributed to the enhancement of spin pumping.

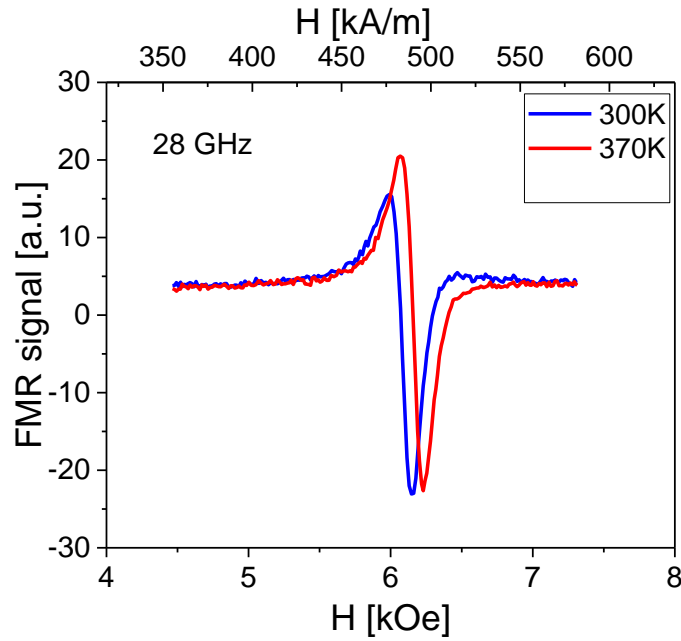


Figure 5.4: Raw resonance curves from the series A sample. The shift in H_{res} is expected due to the temperature dependence of T_c in Py.

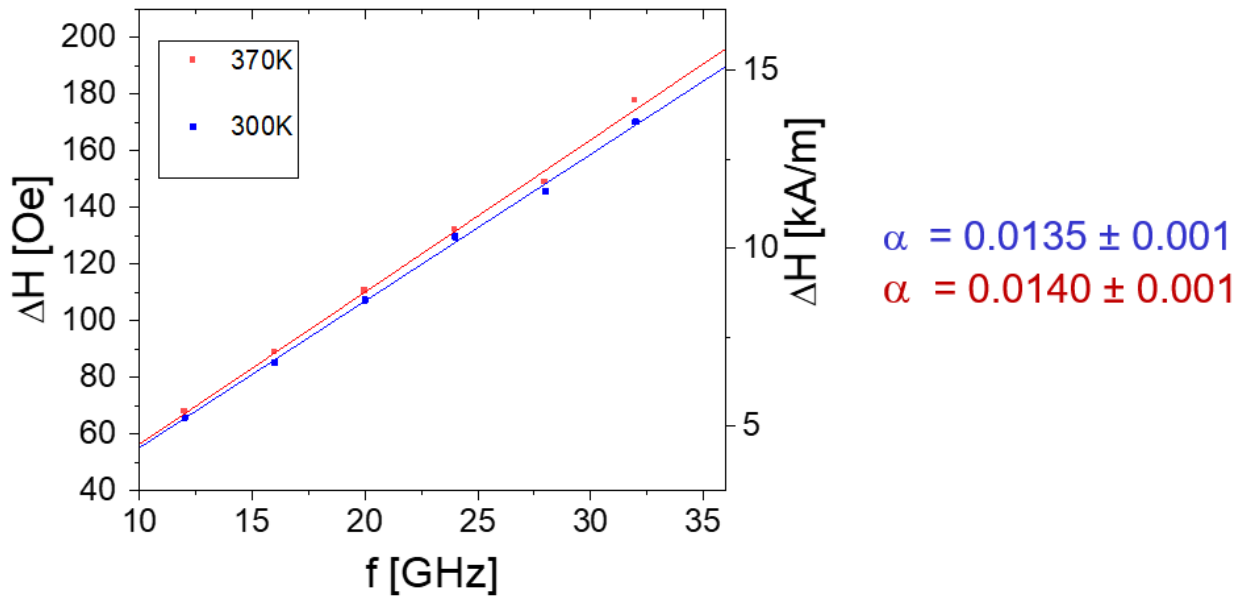


Figure 5.5: Series A effective damping parameters above and below the MIT

One should note that the extracted values of α , 0.0135 and 0.0140, are significantly higher than the expected value for pure Py at room temperature ($\alpha \sim 0.007$ -0.008) in both the pre

and post MIT measurements [73]. This would suggest that Ru is acting as an effective spin sink and is likely greatly limiting the magnitude of spin current reaching the VO₂ layer.

Figures 5.6 through 5.8 present the damping analysis for the 4, 6, and 20 nm Py films from series B, where the Ru seed layer is 2.3 nm. In all cases the damping has been reduced below the value seen in series A.

The back reflection (β) relation implies that for spin sinks where the spin diffusion length exceeds the film thickness we should have an elevated back reflection magnitude [74], resulting in a reduced α' contribution. As the layer thickness is increased, α' should likewise be enhanced. It has been reported by Behera, et.al. that the spin diffusion length in ruthenium is ~14nm at 4 K and the authors suggest this should be of similar order for room temperature measurements [74]; other authors [63] have argued this value is greatly reduced near room temperature and should be in the 3-5 nm range. In either case, it could be reasoned that the increased back reflection term explains the lack of spin polarized current reaching the VO₂ layer. As the effective damping seems to be highly sensitive to the Ru thickness in these series, we can presume that the relaxation of spin current pumped into the Ru layer is the dominant mechanism contributing to the increased damping magnitude.

Furthermore, we see that when the Py thickness has become large (20 nm) the effective damping has returned to the values seen in pure Py. As the spin pumping contributions have been mostly removed due to the inverse thickness dependence of the effect, the small change in the damping between the room temperature and 385 K measurement can be attributed only to changes in the relaxation mechanisms intrinsic to Py. This thermal increase in magnetic relaxation has been reported by Zhao, et al who showed that the effective bulk damping parameter in pure Py films shows a nearly linear increasing trend with temperature [75] (Figure

5.9). Their trend would very roughly suggest a bulk damping parameter increase of ~ 0.0005 - $.0006$ between our two measurement temperatures, which shows consistency with the extracted effective damping parameters presented below. This small shift in the net effective damping due to the increase of the Py bulk damping factor could be seen in all samples in series A and B (excluding Py(4nm)). By subtracting out this contribution, we can see that in all samples with the Ru seed layer the spin pumping contribution to the effective damping shows no increase upon the MIT.

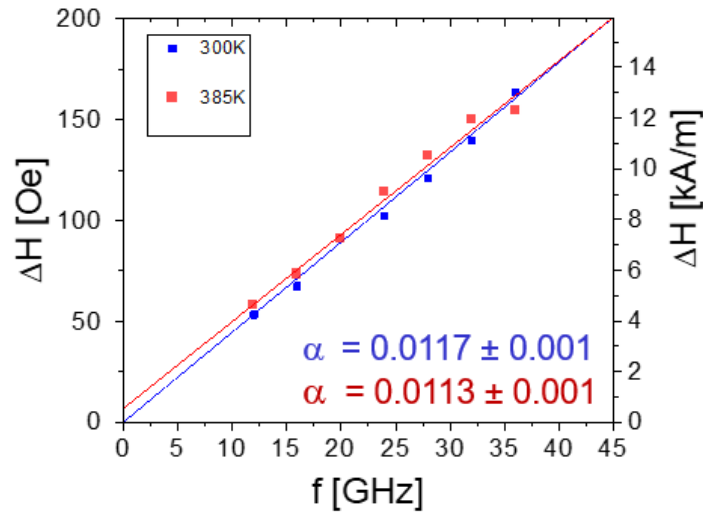


Figure 5.6: Series B, 4 nm effective damping parameters

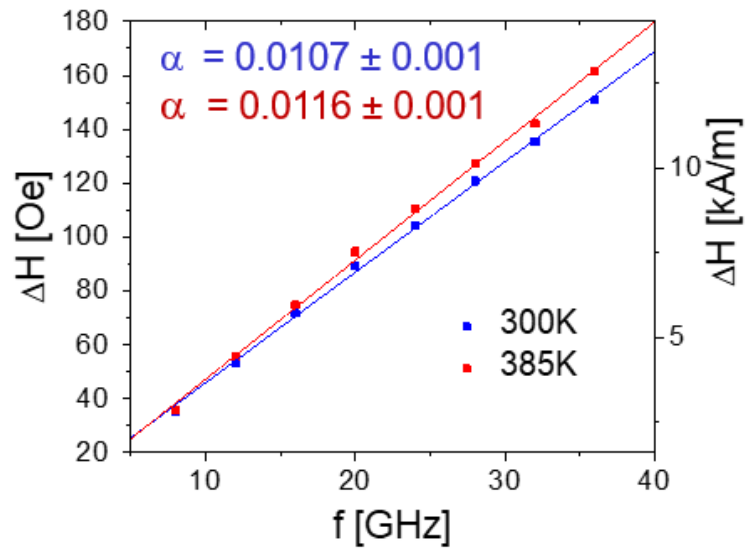


Figure 5.7: Series B, 6 nm effective damping parameters

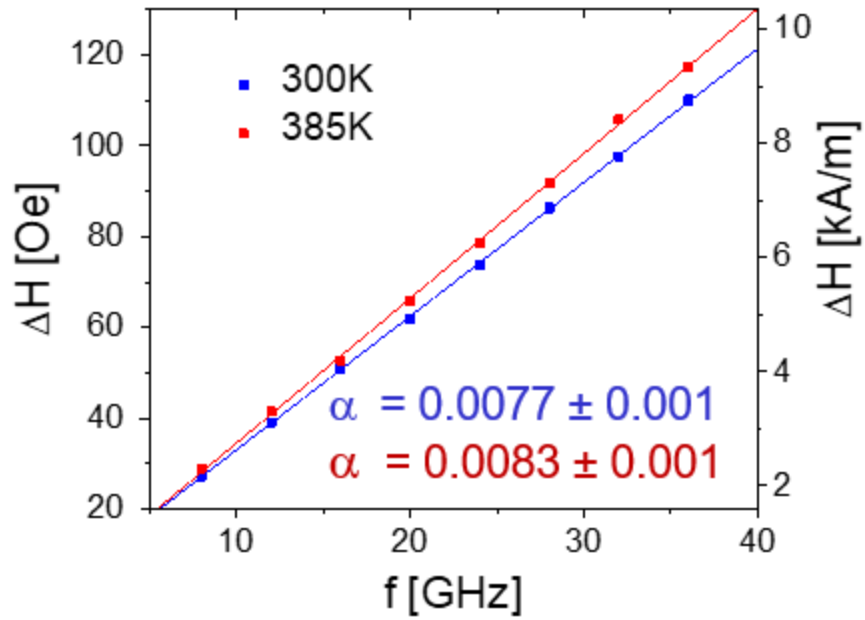


Figure 5.8: Series B, 20 nm effective damping parameters

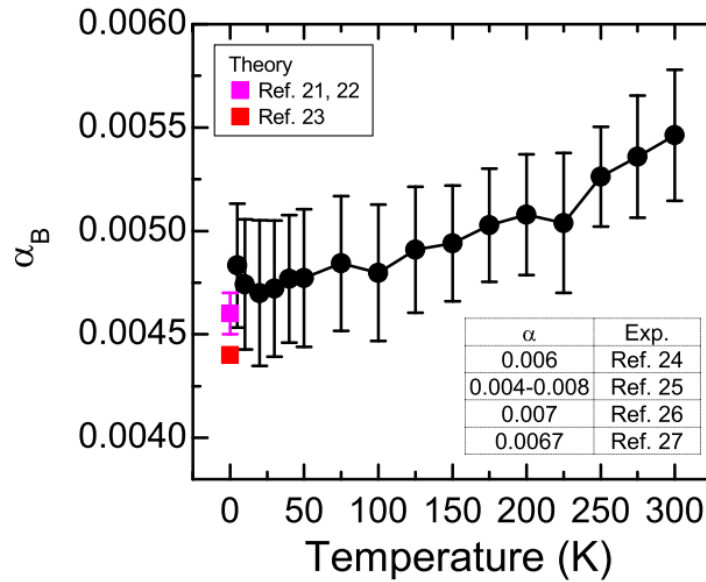


Figure 5.9: Bulk damping parameters in Py exhibit a nearly linear dependence on temperature approaching room temperature. This increase in Py damping with heating can account for the variable damping parameters seen in the VO₂/Py(20) films where spin pumping should mostly be eliminated. [75]

In series C we have removed the Ru seed layer entirely. The effective damping analysis results are presented in Figures 5.10 and 5.11. We can see that for the Py(20nm) sample, the damping parameters exactly match the values shown for series B, including the small (~ 0.0006) enhancement to the damping parameter associated the temperature dependent bulk damping parameter of permalloy.

For the Py(6nm) film there is a clear decrease in the effective damping from the equivalent thickness sample in the B series. From this we can deduce that the Ru seed behaves more effectively as a spin sink as compared to the VO₂ layer. This is not surprising as the conductivity of VO₂ (110) in the metallic phase is $\sim 10^3 \Omega^{-1}\text{cm}^{-1}$ which is 2 orders of magnitude lower than for ruthenium ($1.4 \times 10^5 \Omega^{-1}\text{cm}^{-1}$).

We can now compare the effective damping parameters in the Py(6nm) film to see if the spin pumping is enhanced upon the MIT. As mentioned above we can correct for the enhanced

bulk Py damping by subtracting it from our 385 K damping parameter. After this correction is included we see an enhancement of the 385 K damping parameter of nearly 8% after transitioning from the insulating to metallic state. As this enhancement is clearly dependent on the Py film thickness, we can attribute this increase to spin pumping into the metallic VO₂ layer.

We can also note that in the room temperature measurement of the Py(6nm) sample the damping parameter does not fully return to the pure bulk permalloy value. As has been suggested elsewhere in this work, VO₂ does not fully return to the insulating state at room temperature and will have many regions of sparsely populated metallic domains persist until well below 300 K. It is likely that the small damping enhancement is associated with spin pumping into these small metallic regions of the VO₂ layer.

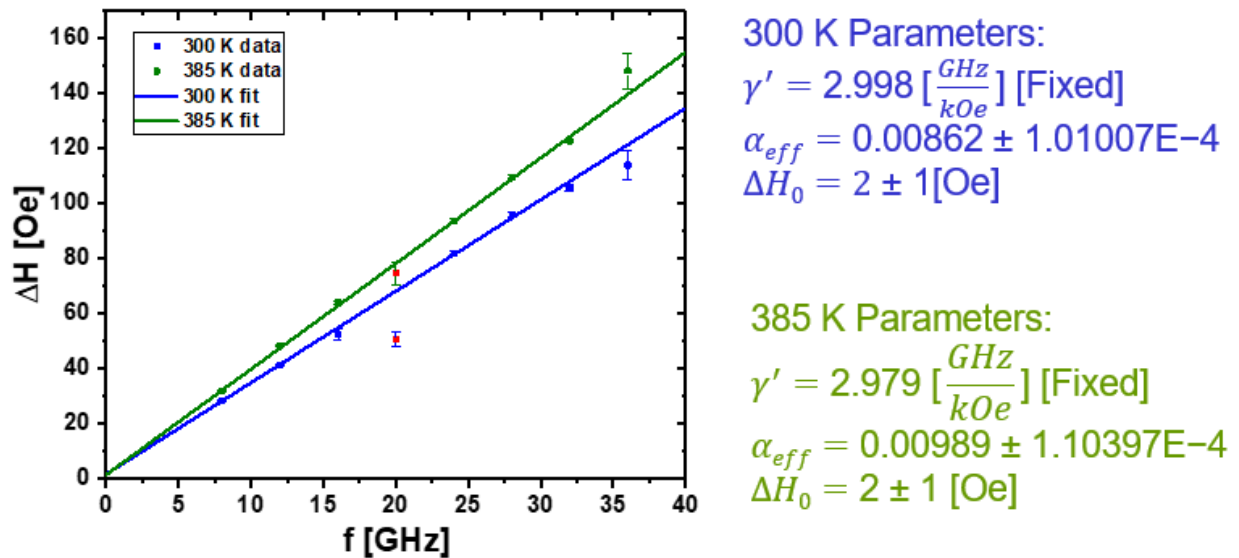


Figure 5.10: Series C, 6 nm effective damping parameters

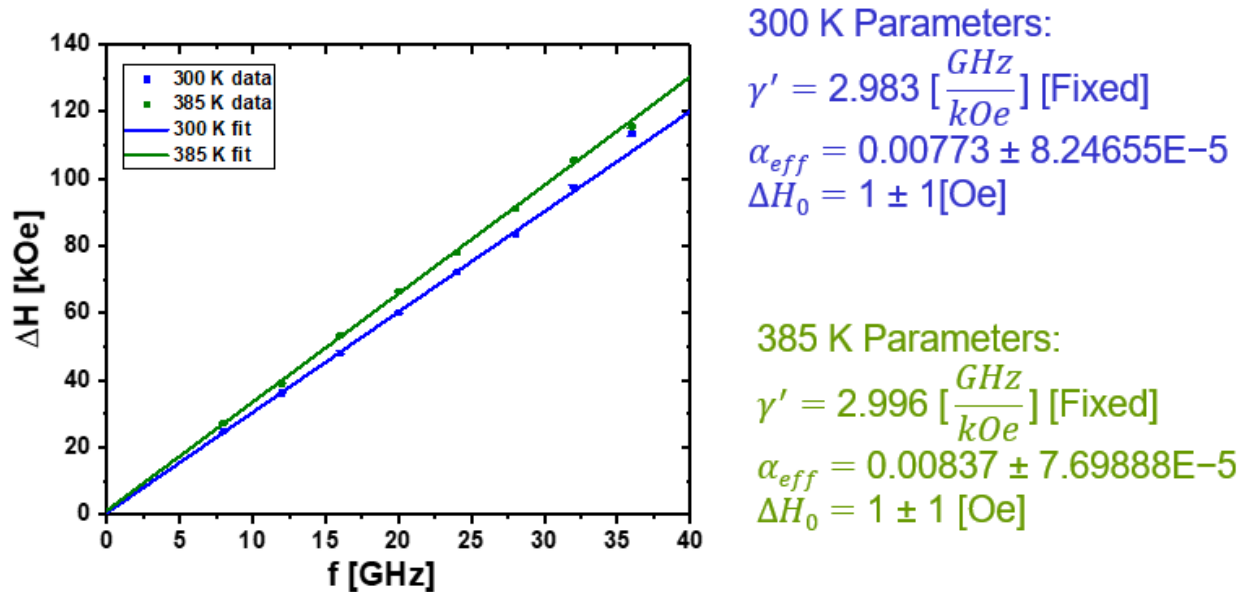


Figure 5.11: Series C, 20 nm effective damping parameters

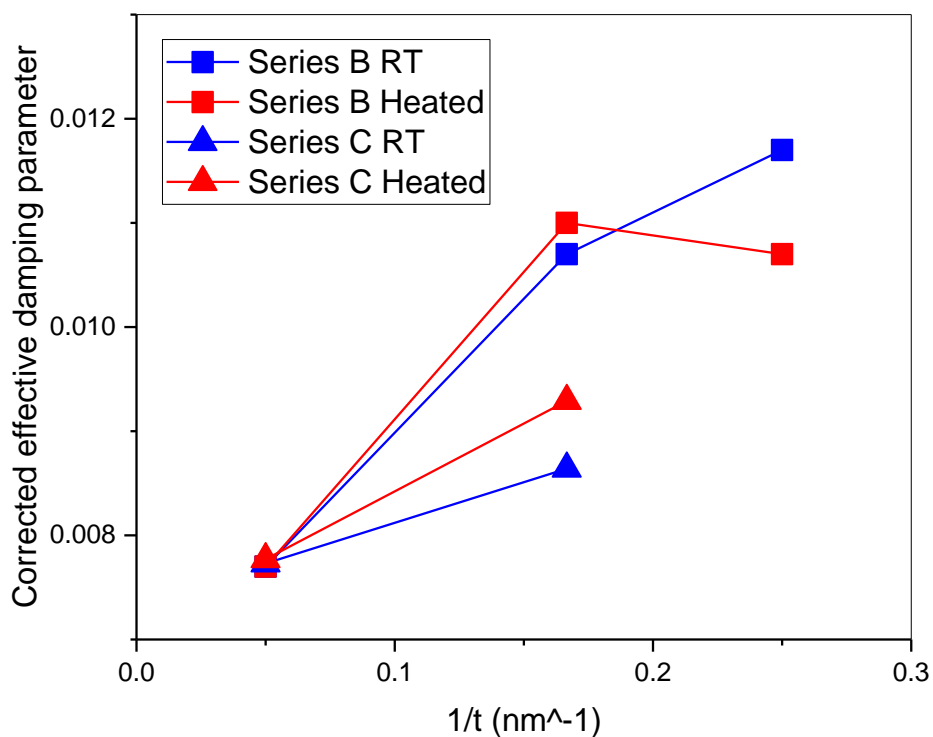


Figure 5.12: A summary of the damping results from series B and C after correcting for thermal effects.

5.6. Summary

In summary, we have produced three series of VO₂(110)/Ru(t)/Py(t)/Al(3) sputtered samples to determine the contributions to effective damping upon the MIT in VO₂. We showed that upon the MIT, the effective spin damping parameter shows an enhancement of 8% and can be directly attributed to increased spin pumping into the VO₂ film as it transitions into the metallic state. This temperature dependent damping enhancement associated to spin pumping is removed upon the insertion of a Ru seed layer between the Py and VO₂. All series with Ru seed layers show no temperature dependence in the damping upon correcting for thermal variation in the bulk Py damping factor.

CHAPTER 6:

LOW FREQUENCY NOISE SPECTROSCOPY OF THE METAL-TO-INSULATOR TRANSITION OF PATTERNED VO₂ THIN FILMS

Low frequency (1/f) noise [76] [77] [78] spectroscopy has proven to be a useful tool in characterizing the dynamic electronic properties of many material systems including GMR and TMR reader devices [79], semiconductor materials [80], percolation networks [81], and a variety of strongly correlated electron systems. It has also been applied to probing film and interface quality in manufacturing applications.

As the MIT of VO₂ is characterized by the coexistence of metallic and insulating regions, with evidence for a broad distribution of energy barriers to transition (see Ch 4), the system is an ideal candidate for analysis with 1/f spectroscopy. When heating through the MIT, the random creation of metallic domains (forming percolative conductive channels through the film) leads to highly temperature dependent noise profiles [82] [83] [84]. By isolating transport along the crystallographic axes through Hall bar patterning, we can determine if the anisotropic conductivity measurements described in Chapter 3 extend to axis dependent noise features. By fitting the 1/f noise data to Hooge's formula we can extract a noise factor, K, for all temperatures that should allow the selection of physical models for noise scaling behavior both before and after the MIT.

In this chapter, we describe the architecture of a home-built low frequency noise spectroscopy system and the software tools used in analyzing the collected spectrums. We describe a series of Hall bar patterned VO₂ films that allow for crystallographic isolation of the noise profiles. The resulting noise factors are shown to have distinct physical origins in the pre

and post transition states. Below T_c the noise factor scales as R^{-2} indicating the primary noise source as being thermal fluctuations within the isolated metallic domains. In the metallic regime the noise factor begins to scale as R^{-3} which is possibly a feature of the strong electron-electron correlations modifying transport from a simple metallic like behavior.

6.1. System Description

Noise spectrums were collected using a home-built system diagrammed in Figure 6.1 [85]. The VO_2 samples (DUT) is mounted with thermal grease to the copper heating block of the LabView controlled low-overshoot heating system (described in Chapter 3) and bonded with a 4-contact configuration. A constant current source is used to probe the samples for all $1/f$ measurements, and is seen connected in parallel with the sample. The current source has a high output impedance (~ 100 MOhm) to minimize thermal noise contributions; as the source is connected in parallel with the DUT, the combined impedance should approximate the sample impedance when $R_{Source} \gg R_{DUT}$.

Two voltages signals are independently passed through a series of 0.03-100 kHz band pass filters to minimize noise power contributions outside our range of interest and further amplified with a pair of Par-113 low noise amplifiers with a net gain of 100,000x. The signals are then collected with a NI-6154 data acquisition card. This card is utilized due to its high sampling rate (250 kHz) and channel-to-channel isolation (no shared ground between channels).

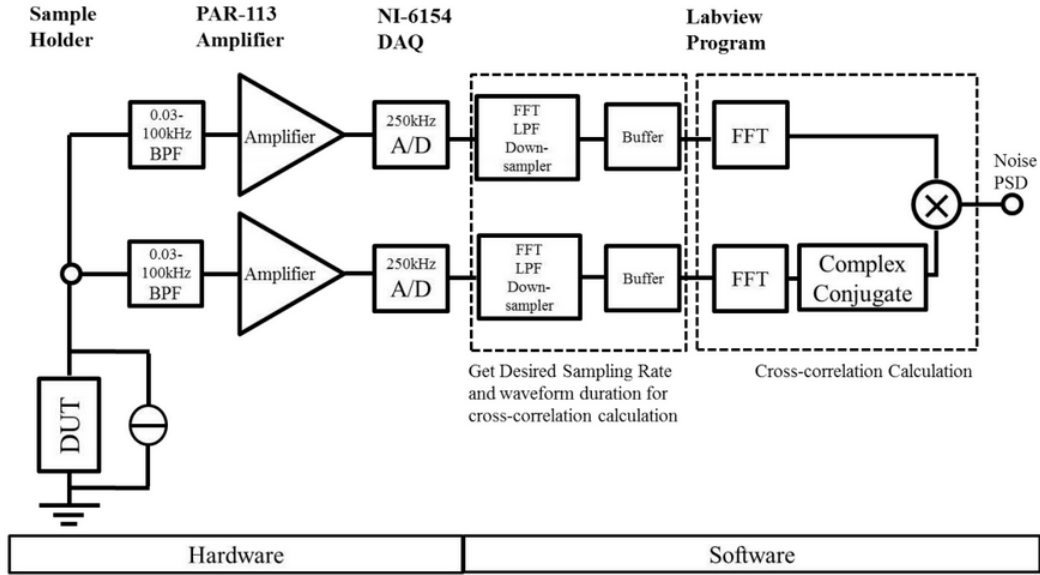


Figure 6.1: The hardware components of the home-built 1/f noise spectroscopy system.

The DAQ then feeds the voltage signals through a custom LabView controller. This controller makes use of the cross-correlation method to extract the power spectrum associated only with the samples. For two continuous voltage signals, $x(t)$ and $y(t)$, we can define the cross correlation as [86]

$$R_{xy}(\tau) = \int_{-\infty}^{\infty} x^*(t)y(t + \tau)dt$$

where τ is defined as the lag time and $x^*(t)$ is the complex conjugate of $x(t)$. From the Wiener-Khinchin theorem we can then relate this cross-correlation to the power spectral density

$$S_{xy}(\omega) = \mathcal{F}[R_{xy}(\tau)]$$

where \mathcal{F} is the Fourier transform function. The cross-correlation theorem states

$$R_{xy}(\tau) = \mathcal{F}[x^*(t)y(t)]$$

which allows the simplification of calculating the power spectrum to computing the Fourier transform of x and y independently then computing the cross correlation of the resulting functions

$$S_{xy}(\omega) = \mathcal{F}[x(t)]^* \mathcal{F}[y(t)]$$

By buffering our signal for a user defined period (generally 10s) we can apply the fast Fourier transform method (FFT) to calculate \mathcal{F} for each channel. The calculated power spectrums are continuously averaged over several hours to increase the total measurement sensitivity, with a minimum of $\sim 10^{-20}$ V²/Hz over a 5 hour measurement period. The minimum frequency is controlled by the buffering time, and is defined as $f_{min} = \frac{1}{t_{buffer}}$. The maximum frequency is capped by the Nyquist limit as half the DAQ sampling frequency (125 kHz) though this can be further reduced with a low pass filter down sampler before the buffering stage.

To reduce external interference the measurement hardware is contained in a shielded steel cabinet. Within the cabinet the channel specific electronics are further isolated in individual metal boxes. Several modifications to the controller computer were required to allow the use of the available onboard PCI DAQ versus a more expensive USB capable card. Some of the modifications can be seen in Figure 6.2. The primary improvement in noise reduction came from the externalization of the AC to DC power supply. The power supply in the desktop is of a switched-mode type which produces significant RF interference when in close proximity to the unshielded pins of the DAQ before completing the analog to digital signal conversion. The power supply was removed from the computer casing and the component power supply cables were extended to ~ 1 m. The supply was placed in a steel container external to the measurement cabinet with the component power cabling fed through a braided copper sheath extending directly to the motherboard. The DAQ was further isolated from system components via the

installation of a thick copper plate in the adjacent card slot. These modifications reduced the 5 hour system sensitivity from $\sim 10^{-18}$ V²/Hz to $\sim 10^{-20}$ V²/Hz and reduced the 60 Hz interference peak by around 4 orders of magnitude.

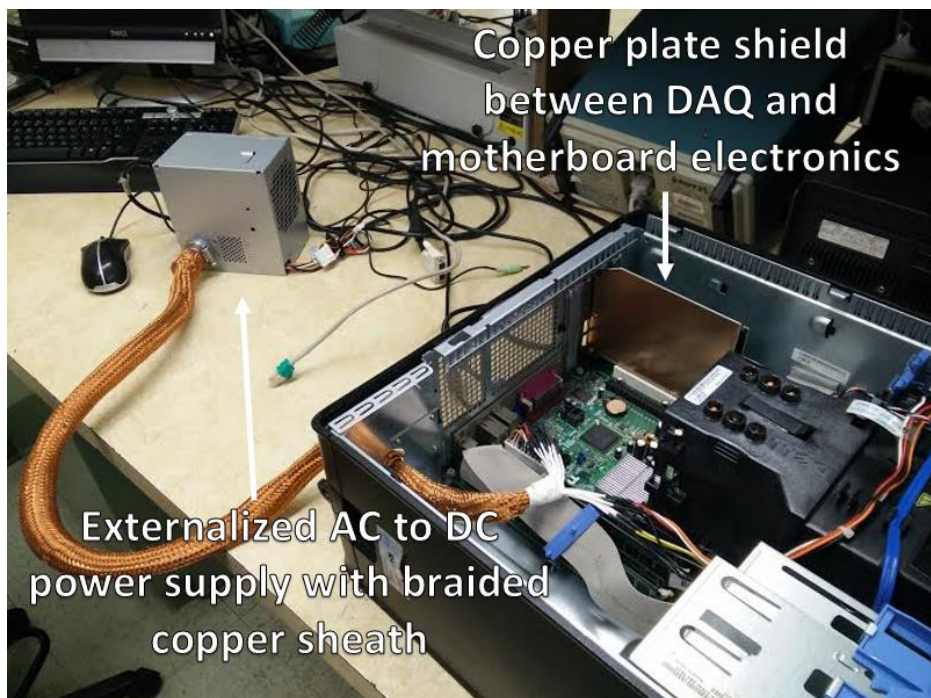


Figure 6.2: Modifications made to the controller computer to limit noise contributed by the internal switched-mode power supply. The externalization of the supply reduced the system noise floor by two orders of magnitude.

6.2. Methodology

Thin films of VO₂ were grown onto TiO₂ substrates with the crystallographic orientations (100), (001), and (110). Details of the film growth and characterization of the samples used in this experiment can be found in chapters 2 and 3 respectively. Additionally, the (100) films were patterned via photolithography with a Hall bar mask to isolate transport along the a and c axes. The LabView interface features fully automated control of temperature and measurement parameters. For all samples, spectrums were collected at many temperatures between 300 K – 400 K with increased measurement density in temperatures near T_c and were repeated for both

heating and cooling cycles. At every temperature step the temperature controller was allowed a 10-30 minute settling period to before beginning PSD collection. Both white noise spectrums (discussed below) and probing current spectrums were collected for every temperature, with currents varying from 0.5-10 μA . The data collection periods were 1 hour, which provided sufficient time dependent sensitivity at all sample impedances.

6.3. Analysis Method of 1/f Noise Parameters

Due to large file sizes (~31 MB, 2.5 million values per PSD) of the collected spectrums, the resulting white noise and current probed data was initially processed by a self-written MatLab program. The software first subtracts the zero current white noise spectrums from the current probed data to remove thermal noise, external interference, and other spurious contributions. The thermal noise (Johnson-Nyquist) has a frequency independent PSD given by

$$S_V = 4k_B TR$$

and can further be used to extract the sample resistance for all measurements to normalize the PSD as

$$\frac{S_V}{V^2} = \frac{S_R}{R^2} = \frac{S_V}{I^2 R^2}$$

The script then selects only the frequency range of interest, here selected to be 1-10 Hz, and fits this range to the Hooge empirical formula for 1/f noise: [76]

$$\frac{S_v}{V^2} = \frac{\gamma}{nVf^\alpha} = \frac{K}{f^\alpha}$$

where γ is the Hooge parameter, n is the charge carrier density, V is the active volume, α is the frequency exponent, and K is the noise factor. We can define V as the net sample volume through which current is carried, which should be distinct from the volume fraction of metallic

domains, as local percolative channels could allow for the majority of current to be carried in a small subset of the total metallic volume. This definition limits the capability of accurately determining V through standard transport measurements. Similarly, the value n is highly sensitive to the sample transition state and varies by as much as 4 orders of magnitude (from $\sim 10^{19}$ to 10^{23} cm⁻³) through the MIT [87]. As extraction of γ would require precise measurements of both V and n , we will use the noise factor K as a general indicator of noise magnitude within our desired frequency range.

6.4. Noise Factors and Scaling

A representative selection of raw current probed noise spectrums are presented in Figure 6.3. This series comes from an a-axis isolated (100) sample during a heating cycle using a probing current of 1 μ A. There is a clear bimodal grouping of the spectrums in the low frequency regime, with the total $1/f$ noise power increasing from room temperature to a maximum at T_c then dropping by more than three orders of magnitude once achieving a fully metallic transition. The roll-off seen in all spectrums around 10^4 Hz is due to system stray capacitance that only minimally contributes to a reduced noise power within the low frequency region; any minor contribution is removed by the initial white noise subtraction step described in the previous section. The outlying points seen around 60 Hz and its multiples are due to powerline interference that is not reduced during the cross-correlation step, but does not affect the analysis due to falling outside the selected frequency range. The large peaks at ~ 30 kHz are due to fluorescent light ballasts in adjacent laboratories.

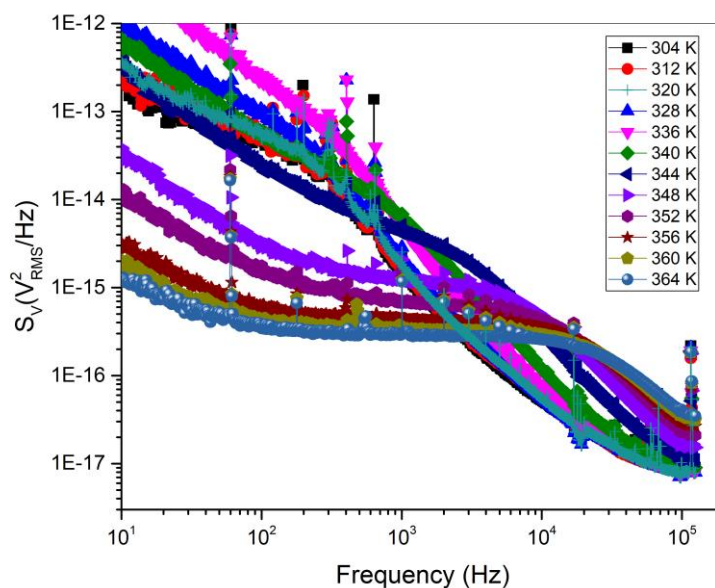


Figure 6.3: Raw output data from the noise spectroscopy system in the full frequency measurement range. The overall noise power for samples drops after the MIT, which is attributed to the reduction of Johnson-Nyquist thermal noise when the sample resistance decreases.

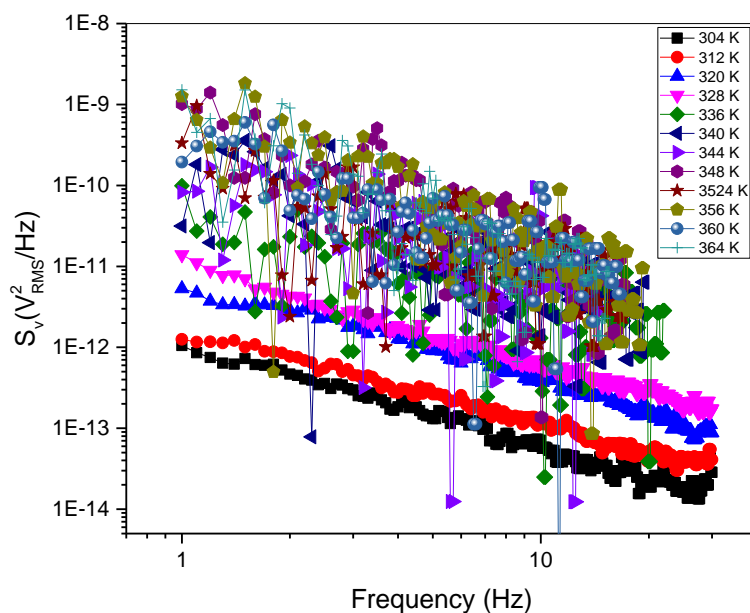


Figure 6.4: Normalized $1/f$ noise profiles for a wide range of measurement temperatures. After normalization, there is a clear pattern of increasing noise power factor as the film transitions to the rutile metallic state.

The same data series is shown in Figure 6.4 after being processed for analysis. The normalization procedure produces another bimodal grouping of spectrums with a smooth transition in increasing noise factor as the sample undergoes the MIT through heating. The results of the noise factor analysis for all un-patterned samples is summarized in Figure 6.5. For all crystallographic orientations (and for both heating and cooling cycles) the noise factor is mostly stable in the fully insulating or metallic state, smoothly transitioning by 3-4 orders of magnitude within the proximity of T_c . The lack of an extended stable region of K for the insulating states of (100) and (110) are further evidence for the existence of persistent metallic domains down to room temperature. The K values stabilize quickly after the sample reaches T_c as the majority of conduction will occur within a small volume of percolative metallic channels that will dominate the overall noise profile. The frequency exponent, α , is near 1 for most measurements and generally falls between 0.8 and 2.

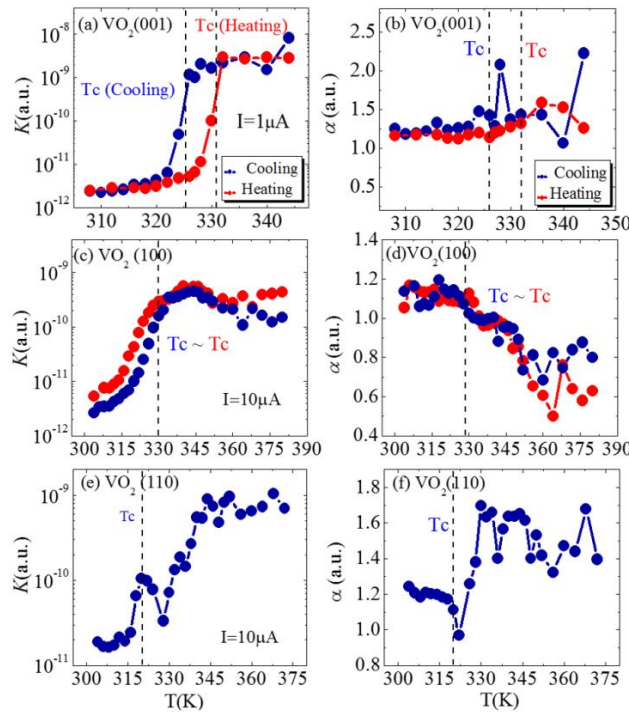


Figure 6.5: The temperature dependence of the noise factor for (001), (100), and (110) film orientations.

As we know the VO₂ film resistance falls by 3-4 orders of magnitude from the insulating to metallic state while the noise factor seems seem follow an inverse trend, it is reasonable to suggest that the noise power should have some consistent scaling behavior with the resistance. As we also know that the axis specific conductivity (shown in Figure 6.6 for a (100) patterned film) shows anisotropic characteristics it should be relevant to compare the noise scaling properties along the isolated axes to determine if the underlying noise mechanisms are independent in origin.

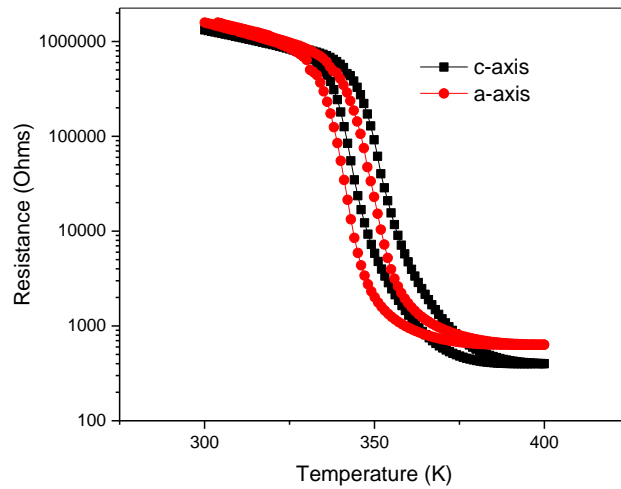


Figure 6.6: R(T) data for patterned (100) VO₂ exhibits a clear transport anisotropy, with the T_c of the c_r axis shifted to higher temperature in both heating and cooling cycles.

It is common for 1/f noise from a wide variety of transport mechanisms (ballistic and diffusive transport, mobility fluctuations) to produce clear power law scaling behavior [88].

Explicitly we should be able to easily fit 1/f data to the form

$$K \propto R^n$$

where we will extract a consistent value for the scaling exponent, n, when the transport noise mechanism is unchanged. In Figure 6.7 this scaling relationship is explored by tracking the ratio of log(K) to log(R) through the MIT. From this plot we can see that in the insulating state the

scaling exponent is very close to -2 while in the metallic region this decreases to approximately -3.

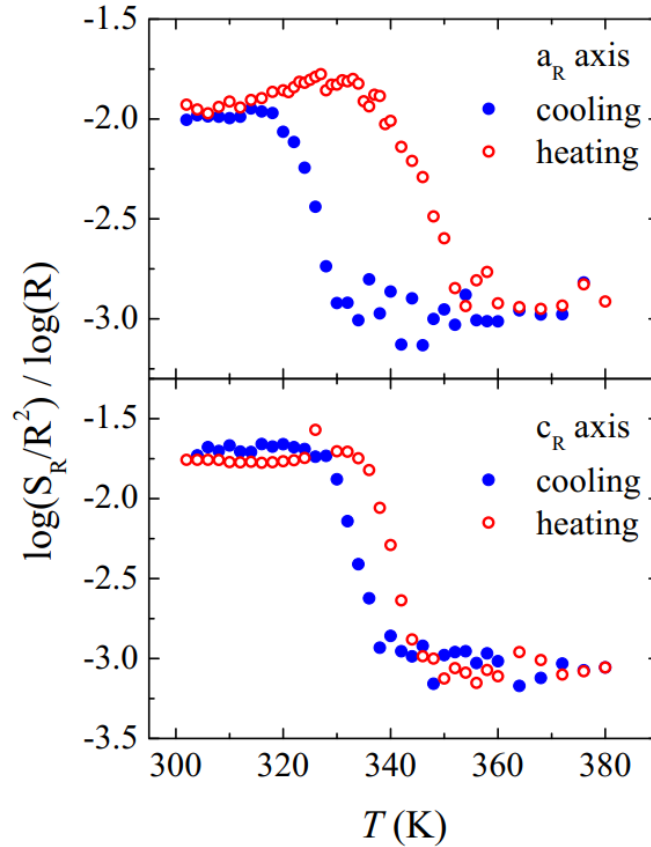


Figure 6.7: The ratio of $\log(K/R)$ shows nearly identical values in the metallic and insulating states for both axes. This would suggest that $1/f$ noise is fundamental to the transitional state of the sample. Due to the differing resistance scaling, we can argue that the $1/f$ noise arises from distinct physical origins in the rutile and monoclinic regimes.

The R^{-2} scaling behavior in the insulating state is consistent with models for the normalized power spectrums caused by thermal fluctuations. This can be shown to follow the relationship [89]

$$\frac{S_V}{V^2} \propto \left(\frac{1}{R} \frac{\delta R}{\delta T} \right)^2$$

In this model the total sample resistance is dominated by the insulating matrix while the derivative term is governed by the large resistance fluctuations caused by the unstable production

of metallic domains due to thermal variations within the sample, likely from a variety of mechanisms including avalanche breakdown and localized domain heating due to current crowding [90] [91]. In comparison, the R^{-3} scaling shown in the metallic state follows no well-known noise scaling behavior. This is likely due to the limitations of modeling the rutile VO_2 as a Drude-like metal, as the short mean free [92] path, on the order of the lattice constant, suggests a bad-metal like behavior in transport [93].

Regardless of the physical origins of the metallic scaling exponent, it is clear that the noise power scaling is consistent in both the a and c axes in our patterned films. This suggests that while the asymmetry in the conductivity, which derives from the dimerization of the vanadium atoms along the c axis, produces different transition magnitudes along each axis, the underlying noise mechanisms are consistent along both axes and for all crystallographic orientations.

CHAPTER 7:

SUMMARY

In this work, we have presented the details of dynamic transport characterization experiments of epitaxial VO₂ thin films grown onto rutile TiO₂ (100), (110), and (001) substrates. These films were deposited using a home-built LPCVD system described in Chapter 2. For 1/f noise spectroscopy experiments these films were patterned into Hall bars using photolithography techniques. For FMR spin pumping experiments our films were further deposited with Py and Ru using the in-house RASCAL magnetron sputtering system to create FM heterostructures devices.

In Chapter 4, we collected time dependent impedance spectrums for thin films of VO₂ as they were kept at a series of highly stable temperatures after cooling from well above T_c. We justified using a parallel RC circuit model to fit these films. The drift in the extracted resistances was found to be defined by two relaxation processes of distinct timescales, one of which closely matches the timescale found in the drift of the sample capacitance. We proposed that the process trending with the capacitance drift is related to small metallic domains congregating into larger metallic islands in a process similar to Ostwald ripening. The second process is likely due to the random formation of metallic domains within the insulating interstitial regions due to the presence of a broad distribution of energy barriers to transition.

In Chapter 5, we performed a series of temperature dependent FMR spin pumping experiments on VO₂/Ru/Py heterostructures. We showed that upon the MIT, the effective spin

damping parameter exhibits an enhancement of 8% and can be directly attributed to increased spin pumping into the VO₂ film as it transitions into the metallic state. This temperature dependent damping enhancement associated to spin pumping was removed upon the insertion of a Ru seed layer between the Py and VO₂. All series with Ru seed layers showed no temperature dependence in the damping upon correcting for thermal variation in the bulk Py damping factor.

In Chapter 6, we probed the 1/f noise profile along the isolated a_r and c_r axes of VO₂ (100) using Hall bar patterned films. We showed that while standard DC transport measurements show some degree of transport anisotropy, likely due to the V-V dimerization directed along the c_r axis, our 1/f measurements did not display unique noise profiles for each orientation. More generally we showed that the pre-MIT film state is characterized by an R⁻² noise scaling that indicates an origin of thermal fluctuations within the sparsely populated metallic domains. The fully rutile metallic regime is characterized by a unique R⁻³ scaling indicative of the bad-metal nature of metallic VO₂.

REFERENCES

- [1] F. J. Morin, "Oxides Which Show a Metal-to-Insulator Transition at the Neel Temperature," *Physical Review Letters*, vol. 3, no. 34, 1959.
- [2] A. Gray, J. Jeong, N. Aetukuri, P. Granitzka, Z. Chen, R. Kukreja, D. Higley, T. Chase, A. Reid, H. Ohldag, M. Marcus, A. Scholl, A. Young, A. Doran, C. Jenkins, P. Shafer, E. Arenholz, M. Samant, S. Parkin and H. Dürr, "Correlation-Driven Insulator-Metal Transition in Near-Ideal Vanadium Dioxide Films," *Physical Review Letters*, vol. 116, no. 116403, 2016.
- [3] D. R. S. R. Gokul Gopalakrishnan, "On the triggering mechanism for the metal–insulator transition in thin film VO₂ devices: electric field versus thermal effects," *Journal of Materials Science*, vol. 44, no. 19, pp. 5345-5353, 2009.
- [4] M. Nakano, K. Shibuya, N. Ogawa, T. Hatano, M. Kawasaki, Y. Iwasa and Y. Tokura, "Infrared-sensitive electrochromic device based on VO₂," *Applied Physics Letters*, vol. 103, no. 153503, 2013.
- [5] E. Arcangeletti, L. Baldassarre, D. D. Castro, S. Lupi, L. Malavasi, C. Marini, A. Perucchi and P. Postorino, "Evidence of a Pressure-Induced Metallization Process in Monoclinic VO₂," *Physical Review Letters*, vol. 98, no. 196406, 2007.
- [6] B. Hu, Y. Ding, W. Chen, D. Kulkarni, Y. Shen, V. V. Tsukruk and Z. L. Wang, "External-Strain Induced Insulating Phase Transition in VO₂ Nanobeam and Its Application as Flexible Strain Sensor," *Advanced Materials*, vol. 22, no. 45, pp. 5134-5139, 2010.
- [7] K. G. West, J. Lu, L. He, D. Kirkwood, W. Chen, T. P. Adl, M. S. Osofsky, S. B. Qadri, R. Hull and S. A. Wolf, "Ferromagnetism in Rutile Structure Cr Doped VO₂ Thin Films Prepared by Reactive-Bias Target Ion Beam Deposition," *J Supercond Nov Magn*, vol. 21, pp. 87-92, 2008.
- [8] L. Fan, S. Chen, Z. Luo, Q. Liu, Y. Wu, L. Song, D. Ji, P. Wang, W. Chu, C. Gao, C. Zou and X. Wu, "Strain Dynamics of Ultrathin VO₂ Film Grown on TiO₂ (001) and the Associated Phase Transition Modulation," *Nano Lett*, vol. 14, no. 7, pp. 4036-4043, 2014.
- [9] J. B. Goodenough, "The two components of the crystallographic transition in VO₂," *Journal of Solid State Chemistry*, vol. 3, no. 4, pp. 490-500, 1971.

- [10] V. Eyert, "The metal-insulator transitions of VO₂: A band theoretical approach," *Ann. Phys. (Leipzig)*, vol. 11, no. 9, 2002.
- [11] M. D. Ventra, Y. V. Pershin and L. O. Chua, "Circuit Elements With Memory: Memristors, Memcapacitors, and Meminductors," *Proceeding of the IEEE*, vol. 97, no. 10, 2009.
- [12] H. Jerominek, F. Picard, N. R. Swart, M. Renaud, M. Levesque, M. Lehoux, J.-S. Castonguay, M. Pelletier, G. Bilodeau, D. Audet, T. D. Pope and P. Lambert, "Micromachined uncooled VO₂-based IR bolometer arrays," *Proceedings Volume 2746, Infrared Detectors and Focal Plane Arrays IV*, 1996.
- [13] T. Manning, I. Parkin, M. Pemble, D. Sheel and D. Vernardou, "Intelligent Window Coatings: Atmospheric Pressure Chemical Vapor Deposition of Tungsten-Doped Vanadium Dioxide," *Chem Mater*, vol. 16, no. 4, pp. 744-749, 2004.
- [14] R. M. Wentzcovitch, W. W. Schulz and a. P. B. Allen, "VO₂: Peierls or Mott-Hubbard? A view from band theory," *Phys Rev Lett*, vol. 72, no. 3389, 1994.
- [15] A. Zylbersztein and N. F. Mott, "Metal-insulator transition in vanadium dioxide," *Phys. Rev. B*, vol. 11, no. 4383, 1975.
- [16] H. Choi, J. Ahn, J. Jung and T. Noh, "Mid-infrared properties of a VO₂ film near the metal-insulator transition," *Phys Rev B*, vol. 54, no. 7, 1996.
- [17] M. M. Qazilbash, M. Brehm, B.-G. Chae, P.-C. Ho, G. O. Andreev, B.-J. Kim, S. J. Yun, A. V. Balatsky, M. B. Maple, F. Keilmann, H.-T. Kim and D. N. Basov, "Mott Transition in VO₂ Revealed by Infrared Spectroscopy and Nano-Imaging," *Science*, vol. 318, no. 5857, pp. 1750-1752, 2007.
- [18] J. Laverock, S. Kittiwatanakul, A. A. Zakharov, Y. R. Niu, B. Chen, S. A. Wolf, J. W. Lu and K. E. Smith, "Direct Observation of Decoupled Structural and Electronic Transitions and an Ambient Pressure Monocliniclike Metallic Phase of VO₂," *Physical Review Letters*, vol. 113, no. 216402, 2014.
- [19] T. Yajima, Y. Ninomiya, T. Nishimura and A. Toriumi, "Drastic change in electronic domain structures via strong elastic coupling in VO₂ films," *Phys Rev B*, vol. 91, no. 205102, 2015.
- [20] A. Tselev, V. Meunier, E. Strelcov, W. A. S. Jr, I. A. Luk'yanchuk, K. Jones, R. Proksch, A. Kolmakov and S. V. Kalinin, "Mesoscopic metal-insulator transition at ferroelastic domain walls in VO₂," *Arcs Nano 4*, vol. 8, pp. 4412-4419, 2010.
- [21] J. Pouget, *J. Phys. Chem. Solids*, vol. 33, p. 1961, 1972.

- [22] J. Jones, C. Kaiser, Y. Zheng and Q. Leng, "Magnetic Reader Having a Nonmagnetic Insertion Layer for the Pinning Layer". United States of America Patent 9,842,615, 12 Dec 2018.
- [23] J. Lu, K. G. West and S. A. Wolf, "Very large anisotropy in the dc conductivity of epitaxial VO₂ thin films grown on (011) rutile TiO₂ substrates," *Appl. Phys. Lett.*, vol. 93, p. 262107, 2009.
- [24] "About the Ion Milling Process," Ion Beam Milling, Inc., [Online]. Available: http://www.ionbeammilling.com/about_the_ion_milling_process. [Accessed 11 2017].
- [25] K. H. Ang, G. Chong and Y. Li, "PID control system analysis, design, and technology," *IEEE Transactions on Control Systems technology*, vol. 13, no. 4, pp. 559-576, 2005.
- [26] S. A. Speakman, "Introduction to High Resolution X-Ray Diffraction of Epitaxial Thin Films," MIT Center for Materials Science and Engineering.
- [27] M. B. a. G. Andersson, "GenX: an extensible X-ray reflectivity refinement program utilizing differential evolution," *J. Appl. Cryst.*, vol. 40, pp. 1174-1178, 2007.
- [28] J. Bhattacharjee, "Atomic Force Microscope: Fundamental Principles," [Online]. [Accessed December 2017].
- [29] L. v. d. Pauw, "A method of measuring specific resistivity and Hall effect of discs of arbitrary shapes," *Philips research reports*, vol. 13, pp. 1-9, 1958.
- [30] Quantum Design, "Performing Van der Pauw Resistivity Measurements," March 2007. [Online]. Available: <https://www.qdusa.com/sitedocs/appNotes/ppms/1076-304.pdf>.
- [31] S. Keshavarz, J. Jones, A. Singh, T. Lovorn, A. Gupta, S. Sarker and P. LeClair, "Low-frequency Noise Spectroscopy of Vanadium Dioxide through its Metal-Insulator Transition," *Under Consideration*, 2017.
- [32] X. Zhong, "Semiconductor-Metal Transition in Epitaxial VO₂ Thin Films on TiO₂(100) Considering a Phase Equilibrium," *Doctoral thesis, University of Alabama*, 2013.
- [33] S. Keshavarz, "Synthesis and Characterization of Novel Electronic and Magnetic Systems," *Doctoral Thesis, University of Alabama*, 2015.
- [34] X. Zhang, "Magnetic, Electrical and Magnetotransport Properties of CrO₂ and VO₂-Based Thin Films and Geterostructures," *Doctoral Thesis, University of Alabama*, 2013.

- [35] Y. Muraoka and Z. Hiroi, "Metal–insulator transition of VO₂ thin films grown on TiO₂ 001 and 110 substrates," *Applied Physics Letters*, vol. 80, no. 4, pp. 583-585, 2002.
- [36] B. B. Maranville, J. Mallett, T. P. Moffat, R. D. McMichael, A. P. Chen and W. F. Egelhoff, "Effect of conformal roughness on ferromagnetic resonance linewidth in thin Permalloy films," *Journal of Applied Physics*, vol. 97, p. 10A721, 2005.
- [37] H. Paik and e. al, "Transport properties of ultra-thin VO₂ films on (001) TiO₂ grown by reactive molecular beam epitaxy," *Applied physics letters*, vol. 107, p. 163101, 2015.
- [38] J. Jeong, N. Aetukuri, T. Graf, T. D. Schladt, M. G. Samant and S. S. P. Parkin, "Suppression of Metal-Insulator Transition in VO₂ by Electric Field–Induced Oxygen Vacancy Formation," *Science*, vol. 339, no. 6126, pp. 1402-1405, 2013.
- [39] R. Xie, C. T. Bui, B. Varghese, Q. Zhang, C. H. Sow, B. Li and J. T. Thong, "An Electrically Tuned Solid-State Thermal Memory Based on Metal–Insulator Transition of Single-Crystalline VO₂ Nanobeams," *Advanced Functional Materials*, vol. 21, no. 9, pp. 1602-1607, 2011.
- [40] T. Driscoll, H. Kim, B. Chae, M. Ventra and D. Basov, "Phase-change driven memristive system," *Applied physics letters*, vol. 95, no. 043503, 2009.
- [41] M. Mitra, Y. Jung, D. Gianola and R. Agarwal, "Extremely low drift of resistance and threshold voltage in amorphous phase change nanowire devices," *Applied Physics Letters*, vol. 96, no. 222111, 2010.
- [42] J. Ramirez, A. Sharoni, Y. Dubi and M. G. I. Schuller, "First-order reversal curve measurements of the metal-insulator transition in VO₂: Signatures of persistent metallic domains," *Phys Rev B*, vol. 79, no. 235110, 2009.
- [43] J. Claassen, J. Lu, K. West and S. Wolf, "Relaxation dynamics of the metal-semiconductor transition in VO₂ thin films," *Appl Physics Lett*, vol. 96, no. 132102, 2010.
- [44] A. J. Hauser, E. Mikheev, N. E. Moreno, T. A. Cain, J. Hwang and S. S. Jack Y. Zhang, "Temperature-dependence of the Hall coefficient of NdNiO₃ thin films," *Applied Physics Letters*, vol. 103, no. 182105, 2013.
- [45] X. Zhong, P. LeClair, S. K. Sarkar and A. Gupta, "Metal-insulator transition in epitaxial VO₂ thin films on TiO₂ (100)," *Phys Rev B*, vol. 89, no. 9, p. 094114, 2012.
- [46] G. Markovich, C. P. Collier and J. R. Heath, "Reversible Metal-Insulator Transition in Ordered Metal Nanocrystal Monolayers Observed by Impedance Spectroscopy," *Phys. Rev. Lett.*, vol. 80, no. 3807, 1998.

- [47] F. Lisdat and D. Schafer, "The use of electrochemical impedance spectroscopy for biosensing," *Anal Bioanal Chem*, vol. 391, pp. 1555-1567, 2008.
- [48] T. Springer, T. Zawodzinski, M. Wilson and S. Gottesfeld, "Characterization of Polymer Electrolyte Fuel Cells Using AC Impedance Spectroscopy," *J. Electrochem. Soc.*, vol. 143, no. 2, 1996.
- [49] M. Adachi, M. Sakamoto, J. Jia, Y. Ogata and S. Isoda, "Determination of Parameters of Electron Transport in Dye-Sensitized Solar Cells Using," *J. Phys. Chem B*, vol. 110, pp. 13872-13880, 2006.
- [50] B. Ward, "A Numerical Resistor Network Model for the Determination of Electrical Properties of Nanocomposites, thesis," *Rice University*, 2011.
- [51] Keysight Technologies, "4284A Precision LCR Meter Operation Manual," 13 05 2002. [Online].
- [52] P. Agarwal, M. Orazem and L. H. Garcia-Rubio, "Measurement Models for Electrochemical Impedance Spectroscopy," *J. Electrochem. Soc.*, vol. 139, no. 7, pp. 1917-1927, 1992.
- [53] Hioki, "LCR Meters | Impedance Analyzers | Capacitance Meters How to Use," 2017. [Online]. Available: <https://www.hioki.com/en/products/listUse/?category=10>.
- [54] J. Ramírez, R. Schmidt, A. Sharoni, M. Gomez, I. Schuller and E. Patiño, "Ultra-thin filaments revealed by the dielectric response across the metal-insulator transition in VO₂," *Applied Physics Letter*, vol. 102, no. 6, p. 063110, 2013.
- [55] J. Ramírez, E. Patino, R. Schmidt, A. Sharoni, M. Gómez and I. Schuller, "Evidence for a capacitor network near the metal insulator transition in VO₂ thin films probed by in-plane impedance spectroscopy," *arXiv preprint*, vol. 1105, no. 4308, 2011.
- [56] "Role of activation energy in resistance drift of amorphous phase change materials," *frontiers in Physics*, vol. 2, no. 75, 2014.
- [57] D. Kumar, K. Rajeev, A. Kushwaha and R. Budhani, "Heterogeneous nucleation and metal-insulator transition in epitaxial films of NdNiO₃," *Journal of Applied Physics*, vol. 108, p. 063503, 2010.
- [58] D. Kumar, K. P. Rajeev, J. A. Alonso and M. J. Martínez-Lope, "Spin-canted magnetism and decoupling of charge and spin ordering in NdNiO₃," *Phys. Rev. B*, vol. 88, p. 014410, 2013.
- [59] B. Fisher, "Moving boundaries and travelling domains during switching of VO₂ single crystals," *Journal of Physics C*, vol. 8, no. 13, 1975.

- [60] W. Fan, J. Cao, J. Seidel, Y. Gu, J. Yim, C. Barrett, K. Yu, J. Ji, R. Ramesh, L. Chen and J. Wu, "Large kinetic asymmetry in the metal-insulator transition nucleated at localized and extended defects," *Physical Review B*, vol. 83, no. 235102, 2011.
- [61] Y. Ohnuma, H. Adachi, E. Saitoh and S. Maekawa, "Enhanced dc spin pumping into a fluctuating ferromagnet near T_c ," *Phys Rev B*, vol. 89, p. 174417, 2014.
- [62] B. Khodadadi, J. B. Mohammadi, C. Mewes, T. Mewes, M. Manno, C. Leighton and C. W. Miller, "Enhanced spin pumping near a magnetic ordering transition," *Phys. Rev B*, vol. 96, p. 054436, 2017.
- [63] B. Khodadadi, "Investigation of Magnetic Relaxation Mechanisms and Dynamic Magnetic Properties in Thin Films Using Ferromagnetic Resonance (FMR) Technique," *PhD Thesis, University of Alabama*, 2016.
- [64] Y. Tserkovnyak, A. Brataas and G. E. W. Bauer, "Spin pumping and magnetization dynamics in metallic multilayers," *Phys Rev B*, vol. 66, p. 224403, 2002.
- [65] Y. Tserkovnyak, A. Brataas, G. E. W. Bauer and B. I. Halperin, "Nonlocal magnetization dynamics in ferromagnetic heterostructures," *Reviews of Modern Physics*, vol. 77, 2005.
- [66] M. Lakshmanan, "The fascinating world of the Landau-Lifshitz-Gilbert equation: an overview," *Philosophical Transactions: Mathematical, Physical and Engineering Sciences*, vol. 369, no. 1939, pp. 1280-1300, 2011.
- [67] C. Kittel, "On the Theory of Ferromagnetic Resonance Absorption," *Phys Rev*, vol. 73, no. 155, 1948.
- [68] J. Smit and H. Beljers, *Philips Res. Rep*, vol. 10, no. 31, 1955.
- [69] M. Farle, "Ferromagnetic resonance of ultrathin metallic layers," *Rep. Prog. Phys*, vol. 61, pp. 755-826, 1998.
- [70] C.-R. Chang, "Spin Pumping: A fresh avenue to spin the new century," National Taiwan University, 2017. [Online]. Available: <http://host.cc.ntu.edu.tw/sec/enews/Effective%20circuit%20for%20spin%20pumping.htm>.
- [71] F. D. Czeschka, L. Dreher, M. S. Brandt, M. Weiler, M. Althammer, I.-M. Imort, G. Reiss, A. Thomas, W. Schoch, W. Limmer, H. Huebl, R. Gross and S. T. B. Goennenwein, "Scaling Behavior of the Spin Pumping Effect in Ferromagnet-Platinum Bilayers," *Phys Rev Lett*, vol. 107, p. 046601, 2011.

- [72] J. Bass and W. P. P. Jr, "Spin-Diffusion Lengths in Metals and Alloys, and Spin-Flipping at Metal/Metal Interfaces: an Experimentalist's Critical Review," *arXiv:cond-mat*, p. 0610085, 2007.
- [73] M. A. W. Schoen, J. M. Shaw, H. T. Nembach, M. Weiler and T. J. Silva, "Radiative damping in waveguide-based ferromagnetic resonance measured via analysis of perpendicular standing spin waves in sputtered permalloy films," *Phys. Rev. B*, vol. 92, p. 184417, 2015.
- [74] N. Behera, M. Singh, S. Chaudhary, D. Pandya and P. Muduli, "Effect of Ru thickness on spin pumping in Ru/Py bilayer," *Journal of Applied Physics*, vol. 117, no. 17, p. 17A714, 2015.
- [75] Y. Zhao, Q. Song, S.-H. Yang, T. Su, W. Yuan, S. S. Parkin, J. Shi and W. Han, "Experimental investigation of temperature-dependent Gilbert damping in permalloy thin films," *Scientific Reports*, vol. 6, p. 22890, 2016.
- [76] F. Hooge, "1/f noise sources," *IEEE Transactions on Electron Devices*, vol. 41, no. 11, pp. 1926-1935, 1994.
- [77] F. N. Hooge, T. G. M. Kleinpenning and L. K. J. Vandamme, "Experimental studies on 1/f noise," *Reports on Progress in Physics*, vol. 44, no. 5, 1981.
- [78] P. Bak, C. Tang and K. Wiesenfeld, "Self-organized criticality: An explanation of the 1/f noise," *Phys. Rev. Lett.*, vol. 59, no. 381, 1987.
- [79] H. T. Hardner, M. B. Weissman, M. B. Salamon and S. S. P. Parkin, "Fluctuation-dissipation relation for giant magnetoresistive 1/f noise," *Phys. Rev. B*, vol. 48, no. 16156, 1993.
- [80] M. J. Uren, D. J. Day and M. J. Kirton, "1/f and random telegraph noise in silicon metal-oxide-semiconductor field-effect transistors," *Appl. Phys. Lett.*, vol. 47, no. 1195, 1985.
- [81] R. Rammal, C. Tannous, P. Breton and A. -M. S. Tremblay, "Flicker (1/f) Noise in Percolation Networks: A New Hierarchy of Exponents," *Phys. Rev. Lett.*, vol. 54, no. 1718, 1985.
- [82] L. A. L. d. Almeida, G. S. Deep, A. M. N. Lima and H. Neff, "Thermal dynamics of VO₂ films within the metal-insulator transition: Evidence for chaos near percolation threshold," *Appl. Phys. Lett.*, vol. 77, no. 4365, 2000.
- [83] A. A. Velichko, G. B. Stefanovich, A. L. Pergament and P. P. Boriskov, "Deterministic noise in vanadium dioxide based structures," *Technical Physics Letters*, vol. 29, no. 5, pp. 435-437, 2003.

- [84] Z. Topalian, S. Li, G. Niklasson, C. Granqvist and L. Kish, " Resistance noise at the metal–insulator transition in thermochromic VO₂ films," *Journal of Applied Physics*, vol. 117, p. 025303, 2015.
- [85] X. Zhong, S. Keshavarz, J. Jones, C. Mewes and P. R. Leclair, "Cross-spectrum Analyzer for Low Frequency Noise Analysis," *arXiv*, p. 1408.2470v, 2014.
- [86] I. Noda, "Generalized Two-Dimensional Correlation Method Applicable to Infrared, Raman, and other Types of Spectroscopy," *Applied Spectroscopy*, vol. 47, no. 9, pp. 1329-1336, 1993.
- [87] D. Fu, K. Liu, T. Tao, K. Lo, C. Cheng, B. Liu, R. Zhang, H. A. Bechtel and J. Wu, "Comprehensive study of the metal-insulator transition in pulsed laser deposited epitaxial VO₂ thin films," *Journal of Applied Physics*, vol. 113, p. 043707, 2013.
- [88] G. A. Garfunkel and M. Weissman, "Noise Scaling in Continuum Percolating Films," *Physical Review Letters*, vol. 55, no. 3, p. 296, 1985.
- [89] R. Voss and J. Clarke, "Flicker noise: Equilibrium temperature and resistance fluctuations," *Physical Review B*, vol. 13, p. 556, 1976.
- [90] X. Zhong, X. Zhang, A. Gupta and P. LeClair, "Avalanche breakdown in microscale VO₂ structures," *Journal of Applied Physics*, vol. 110, p. 084516, 2011.
- [91] A. Zimmers, L. Aigouy, M. Mortier, A. Sharoni, S. Wang, K. G. West, J. G. Ramirez and I. K. Schuller, "Role of Thermal Heating on the Voltage Induced Insulator-Metal Transition in VO₂," *Phys Rev Lett*, vol. 110, p. 056601, 2013.
- [92] M. M. Qazilbash, K. S. Burch, D. Whisler, D. Shrekenhamer, B. G. Chae, H. T. Kim and D. N. Basov, "Correlated metallic state of vanadium dioxide," *Physical Review B*, vol. 74, p. 205118, 2006.
- [93] S. Hartnoll, "Theory of universal incoherent metallic transport," *Nature Physics*, vol. 11, pp. 54-61, 2015.
- [94] F. J. Morin, "Oxides Which Show a Metal-to-Insulator Transition at the Neel Temperature," *Phys. Rev. Lett.*, vol. 3, no. 34, 1959.

APPENDIX

Below is a copy of the United States patent “Magnetic Reader Having a Nonmagnetic Insertion Layer for the Pinning Layer” filed on June 26, 2015 and granted December 12, 2017 [22]. This describes a TMR magnetic reader stack modification that was designed and characterized while working as an intern at the Western Digital Corporation in Fremont, CA within their Reader Design group. The reader stacks were characterized on a home-built CPW based FMR system (similar in design to the system utilized in Chapter 5) for which I wrote both the controller software and MATLAB based analysis tools.



(12) **United States Patent**
Jones et al.

(10) **Patent No.:** **US 9,842,615 B1**
(45) **Date of Patent:** **Dec. 12, 2017**

(54) **MAGNETIC READER HAVING A
NONMAGNETIC INSERTION LAYER FOR
THE PINNING LAYER**

- (71) Applicant: **Western Digital (Fremont), LLC**,
Fremont, CA (US)
- (72) Inventors: **Joshua Jones**, Hoover, AL (US);
Christian Kaiser, San Jose, CA (US);
Yuankai Zheng, Fremont, CA (US);
Qunwen Leng, Palo Alto, CA (US)
- (73) Assignee: **Western Digital (Fremont), LLC**,
Fremont, CA (US)
- (*) Notice: Subject to any disclaimer, the term of this
patent is extended or adjusted under 35
U.S.C. 154(b) by 0 days.

(21) Appl. No.: **14/752,659**
(22) Filed: **Jun. 26, 2015**

(51) **Int. Cl.**
G11B 5/39 (2006.01)
G11B 5/60 (2006.01)
G11B 5/31 (2006.01)
G11B 5/00 (2006.01)

(52) **U.S. Cl.**
CPC **G11B 5/3912** (2013.01); **G11B 5/31**
(2013.01); **G11B 5/3903** (2013.01); **G11B**
5/3906 (2013.01); **G11B 5/3932** (2013.01);
G11B 5/6082 (2013.01); **G11B 2005/0008**
(2013.01); **G11B 2005/3996** (2013.01)

(58) **Field of Classification Search**
CPC G11B 5/39; G11B 5/3903; G11B 5/3906;
G11B 2005/3996
USPC 360/324.11
See application file for complete search history.

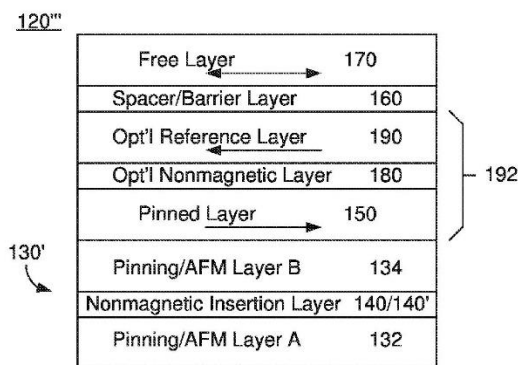
(56) **References Cited**
U.S. PATENT DOCUMENTS

6,016,290	A	1/2000	Chen et al.
6,018,441	A	1/2000	Wu et al.
6,025,978	A	2/2000	Hoshi et al.
6,025,988	A	2/2000	Yan
6,032,353	A	3/2000	Ifiner et al.
6,033,532	A	3/2000	Minami
6,034,851	A	3/2000	Zarouri et al.
6,043,959	A	3/2000	Cruc et al.
6,046,885	A	4/2000	Aimonetti et al.
6,049,650	A	4/2000	Jerman et al.
6,055,138	A	4/2000	Shi
6,058,094	A	5/2000	Davis et al.
6,073,338	A	6/2000	Liu et al.
6,078,479	A	6/2000	Nepela et al.
6,081,499	A	6/2000	Berger et al.
6,094,803	A	8/2000	Carlson et al.
6,099,362	A	8/2000	Viches et al.
6,103,073	A	8/2000	Thayamballi
6,108,166	A	8/2000	Lederman
6,118,629	A	9/2000	Huai et al.
6,118,638	A	9/2000	Knapp et al.
6,125,018	A	9/2000	Takagishi et al.
6,130,779	A	10/2000	Carlson et al.
6,134,089	A	10/2000	Barr et al.
6,136,166	A	10/2000	Shen et al.
6,137,661	A	10/2000	Shi et al.

(Continued)
Primary Examiner — Jefferson Evans
(74) Attorney, Agent, or Firm — Foley & Lardner LLP

(57) **ABSTRACT**
A method and system provide a magnetic read apparatus. The magnetic read apparatus includes a read sensor. The read sensor includes a pinning layer, a nonmagnetic insertion layer and a pinned layer. The nonmagnetic insertion layer has a location selected from a first location and a second location. The first location is between the pinned layer and the pinning layer. The second location is within the pinning layer.

28 Claims, 5 Drawing Sheets



(56)	References Cited						
U.S. PATENT DOCUMENTS							
6,137,662	A	10/2000	Huai et al.	6,417,998	B1	7/2002	Crue, Jr. et al.
6,160,684	A	12/2000	Heist et al.	6,417,999	B1	7/2002	Knapp et al.
6,163,426	A	12/2000	Nepela et al.	6,418,000	B1	7/2002	Gibbons et al.
6,166,891	A	12/2000	Lederman et al.	6,418,048	B1	7/2002	Sin et al.
6,173,486	B1	1/2001	Hsiao et al.	6,421,211	B1	7/2002	Hawwa et al.
6,175,476	B1	1/2001	Huai et al.	6,421,212	B1	7/2002	Gibbons et al.
6,178,066	B1	1/2001	Barr	6,424,505	B1	7/2002	Lam et al.
6,178,070	B1	1/2001	Hong et al.	6,424,507	B1	7/2002	Lederman et al.
6,178,150	B1	1/2001	Davis	6,430,009	B1	8/2002	Komaki et al.
6,181,485	B1	1/2001	He	6,430,806	B1	8/2002	Chen et al.
6,181,525	B1	1/2001	Carlson	6,433,965	B1	8/2002	Gopinathan et al.
6,185,051	B1	2/2001	Chen et al.	6,433,968	B1	8/2002	Shi et al.
6,185,077	B1	2/2001	Tong et al.	6,433,970	B1	8/2002	Knapp et al.
6,185,081	B1	2/2001	Simion et al.	6,437,945	B1	8/2002	Hawwa et al.
6,188,549	B1	2/2001	Wiitala	6,445,536	B1	9/2002	Rudy et al.
6,190,764	B1	2/2001	Shi et al.	6,445,542	B1	9/2002	Levi et al.
6,193,584	B1	2/2001	Rudy et al.	6,445,553	B2	9/2002	Barr et al.
6,195,229	B1	2/2001	Shen et al.	6,445,554	B1	9/2002	Dong et al.
6,198,608	B1	3/2001	Hong et al.	6,447,935	B1	9/2002	Zhang et al.
6,198,609	B1	3/2001	Barr et al.	6,448,765	B1	9/2002	Chen et al.
6,201,673	B1	3/2001	Rottmayer et al.	6,451,514	B1	9/2002	Iitsuka
6,204,998	B1	3/2001	Katz	6,452,742	B1	9/2002	Crue et al.
6,204,999	B1	3/2001	Crue et al.	6,452,765	B1	9/2002	Mahvan et al.
6,212,153	B1	4/2001	Chen et al.	6,456,465	B1	9/2002	Louis et al.
6,215,625	B1	4/2001	Carlson	6,459,552	B1	10/2002	Liu et al.
6,219,205	B1	4/2001	Yuan et al.	6,462,920	B1	10/2002	Karimi
6,221,218	B1	4/2001	Shi et al.	6,466,401	B1	10/2002	Hong et al.
6,222,707	B1	4/2001	Huai et al.	6,466,402	B1	10/2002	Crue, Jr. et al.
6,229,782	B1	5/2001	Wang et al.	6,466,404	B1	10/2002	Crue, Jr. et al.
6,230,959	B1	5/2001	Heist et al.	6,468,436	B1	10/2002	Shi et al.
6,233,116	B1	5/2001	Chen et al.	6,469,877	B1	10/2002	Knapp et al.
6,233,125	B1	5/2001	Knapp et al.	6,477,019	B2	11/2002	Matono et al.
6,237,215	B1	5/2001	Hunsaker et al.	6,479,096	B1	11/2002	Shi et al.
6,252,743	B1	6/2001	Bozorgi	6,483,662	B1	11/2002	Thomas et al.
6,255,721	B1	7/2001	Roberts	6,487,040	B1	11/2002	Hsiao et al.
6,258,468	B1	7/2001	Mahvan et al.	6,487,056	B1	11/2002	Gibbons et al.
6,266,216	B1	7/2001	Hikami et al.	6,490,125	B1	12/2002	Barr
6,271,604	B1	8/2001	Frank, Jr. et al.	6,496,330	B1	12/2002	Crue, Jr. et al.
6,275,354	B1	8/2001	Huai et al.	6,496,334	B1	12/2002	Pang et al.
6,277,505	B1	8/2001	Shi et al.	6,504,676	B1	1/2003	Hiner et al.
6,282,056	B1	8/2001	Feng et al.	6,512,657	B2	1/2003	Heist et al.
6,296,955	B1	10/2001	Hossain et al.	6,512,659	B1	1/2003	Hawwa et al.
6,297,955	B1	10/2001	Frank, Jr. et al.	6,512,661	B1	1/2003	Louis
6,304,414	B1	10/2001	Crue, Jr. et al.	6,512,690	B1	1/2003	Qi et al.
6,307,715	B1	10/2001	Berding et al.	6,515,573	B1	2/2003	Dong et al.
6,310,746	B1	10/2001	Hawwa et al.	6,515,791	B1	2/2003	Hawwa et al.
6,310,750	B1	10/2001	Hawwa et al.	6,532,823	B1	3/2003	Knapp et al.
6,317,290	B1	11/2001	Wang et al.	6,535,363	B1	3/2003	Hosomi et al.
6,317,297	B1	11/2001	Tong et al.	6,552,874	B1	4/2003	Chen et al.
6,322,911	B1	11/2001	Fukagawa et al.	6,552,928	B1	4/2003	Qi et al.
6,330,136	B1	12/2001	Wang et al.	6,577,470	B1	6/2003	Rumpler
6,330,137	B1	12/2001	Knapp et al.	6,583,961	B2	6/2003	Levi et al.
6,333,830	B2	12/2001	Rose et al.	6,583,968	B1	6/2003	Scura et al.
6,340,533	B1	1/2002	Ueno et al.	6,597,548	B1	7/2003	Yamanaka et al.
6,349,014	B1	2/2002	Crue, Jr. et al.	6,611,398	B1	8/2003	Rumpler et al.
6,351,355	B1	2/2002	Min et al.	6,618,223	B1	9/2003	Chen et al.
6,353,318	B1	3/2002	Sin et al.	6,629,357	B1	10/2003	Akoh
6,353,511	B1	3/2002	Shi et al.	6,633,464	B2	10/2003	Lai et al.
6,356,412	B1	3/2002	Levi et al.	6,636,394	B1	10/2003	Fukagawa et al.
6,359,779	B1	3/2002	Frank, Jr. et al.	6,639,291	B1	10/2003	Sin et al.
6,369,983	B1	4/2002	Hong	6,650,503	B1	11/2003	Chen et al.
6,376,964	B1	4/2002	Young et al.	6,650,506	B1	11/2003	Risse
6,377,535	B1	4/2002	Chen et al.	6,654,195	B1	11/2003	Frank, Jr. et al.
6,381,095	B1	4/2002	Sin et al.	6,657,816	B1	12/2003	Barr et al.
6,381,105	B1	4/2002	Huai et al.	6,661,621	B1	12/2003	Iitsuka
6,389,499	B1	5/2002	Frank, Jr. et al.	6,661,625	B1	12/2003	Sin et al.
6,392,850	B1	5/2002	Tong et al.	6,674,610	B1	1/2004	Thomas et al.
6,396,660	B1	5/2002	Jensen et al.	6,680,863	B1	1/2004	Shi et al.
6,399,179	B1	6/2002	Hanrahan et al.	6,683,763	B1	1/2004	Hiner et al.
6,400,526	B2	6/2002	Crue, Jr. et al.	6,687,098	B1	2/2004	Huai
6,404,600	B1	6/2002	Hawwa et al.	6,687,178	B1	2/2004	Qi et al.
6,404,601	B1	6/2002	Rottmayer et al.	6,687,977	B2	2/2004	Knapp et al.
6,404,706	B1	6/2002	Stovall et al.	6,691,226	B1	2/2004	Frank, Jr. et al.
6,410,170	B1	6/2002	Chen et al.	6,697,294	B1	2/2004	Qi et al.
6,411,522	B1	6/2002	Frank, Jr. et al.	6,700,738	B1	3/2004	Sin et al.
				6,700,759	B1	3/2004	Knapp et al.
				6,704,158	B2	3/2004	Hawwa et al.
				6,707,083	B1	3/2004	Hiner et al.
				6,713,801	B1	3/2004	Sin et al.

(56)

References Cited

U.S. PATENT DOCUMENTS

6,721,138	B1	4/2004	Chen et al.	7,027,274	B1	4/2006	Sin et al.
6,721,149	B1	4/2004	Shi et al.	7,035,046	B1	4/2006	Young et al.
6,721,203	B1	4/2004	Qi et al.	7,041,985	B1	5/2006	Wang et al.
6,724,569	B1	4/2004	Chen et al.	7,046,490	B1	5/2006	Ueno et al.
6,724,572	B1	4/2004	Stoev et al.	7,054,113	B1	5/2006	Seagle et al.
6,729,015	B2	5/2004	Matono et al.	7,057,857	B1	6/2006	Niu et al.
6,735,850	B1	5/2004	Gibbons et al.	7,059,868	B1	6/2006	Yan
6,737,281	B1	5/2004	Dang et al.	7,092,195	B1	8/2006	Liu et al.
6,744,608	B1	6/2004	Sin et al.	7,110,289	B1	9/2006	Sin et al.
6,747,301	B1	6/2004	Hiner et al.	7,111,382	B1	9/2006	Knapp et al.
6,751,055	B1	6/2004	Alfoqaha et al.	7,113,366	B1	9/2006	Wang et al.
6,754,049	B1	6/2004	Seagle et al.	7,114,241	B2	10/2006	Kubota et al.
6,756,071	B1	6/2004	Shi et al.	7,116,517	B1	10/2006	He et al.
6,757,140	B1	6/2004	Hawwa	7,124,654	B1	10/2006	Davies et al.
6,760,196	B1	7/2004	Niu et al.	7,126,788	B1	10/2006	Liu et al.
6,762,910	B1	7/2004	Knapp et al.	7,126,790	B1	10/2006	Liu et al.
6,765,756	B1	7/2004	Hong et al.	7,131,346	B1	11/2006	Buttar et al.
6,775,902	B1	8/2004	Huai et al.	7,133,253	B1	11/2006	Seagle et al.
6,778,358	B1	8/2004	Jiang et al.	7,134,185	B1	11/2006	Knapp et al.
6,781,927	B1	8/2004	Hcanuc et al.	7,154,715	B2	12/2006	Yamanaka et al.
6,785,955	B1	9/2004	Chen et al.	7,170,725	B1	1/2007	Zhou et al.
6,791,793	B1	9/2004	Chen et al.	7,177,117	B1	2/2007	Jiang et al.
6,791,807	B1	9/2004	Hikami et al.	7,193,815	B1	3/2007	Stoev et al.
6,798,616	B1	9/2004	Seagle et al.	7,196,880	B1	3/2007	Anderson et al.
6,798,625	B1	9/2004	Ueno et al.	7,199,974	B1	4/2007	Alfoqaha
6,801,408	B1	10/2004	Chen et al.	7,199,975	B1	4/2007	Pan
6,801,411	B1	10/2004	Lederman et al.	7,211,339	B1	5/2007	Seagle et al.
6,803,615	B1	10/2004	Sin et al.	7,212,384	B1	5/2007	Stoev et al.
6,806,035	B1	10/2004	Atireklapvarodom et al.	7,238,292	B1	7/2007	He et al.
6,807,030	B1	10/2004	Hawwa et al.	7,239,478	B1	7/2007	Sin et al.
6,807,332	B1	10/2004	Hawwa	7,248,431	B1	7/2007	Liu et al.
6,809,899	B1	10/2004	Chen et al.	7,248,433	B1	7/2007	Stoev et al.
6,816,345	B1	11/2004	Knapp et al.	7,248,449	B1	7/2007	Seagle
6,828,897	B1	12/2004	Nepela	7,266,012	B2	9/2007	Saito et al.
6,829,160	B1	12/2004	Qi et al.	7,280,325	B1	10/2007	Pan
6,829,819	B1	12/2004	Crue, Jr. et al.	7,283,327	B1	10/2007	Liu et al.
6,833,979	B1	12/2004	Knapp et al.	7,284,316	B1	10/2007	Huai et al.
6,834,010	B1	12/2004	Qi et al.	7,286,329	B1	10/2007	Chen et al.
6,859,343	B1	2/2005	Alfoqaha et al.	7,289,303	B1	10/2007	Sin et al.
6,859,997	B1	3/2005	Tong et al.	7,292,409	B1	11/2007	Stoev et al.
6,861,937	B1	3/2005	Feng et al.	7,296,339	B1	11/2007	Yang et al.
6,870,712	B2	3/2005	Chen et al.	7,307,814	B1	12/2007	Seagle et al.
6,873,494	B2	3/2005	Chen et al.	7,307,818	B1	12/2007	Park et al.
6,873,547	B1	3/2005	Shi et al.	7,310,204	B1	12/2007	Stoev et al.
6,879,464	B2	4/2005	Sun et al.	7,318,947	B1	1/2008	Park et al.
6,888,184	B1	5/2005	Shi et al.	7,333,295	B1	2/2008	Medina et al.
6,888,704	B1	5/2005	Diao et al.	7,337,530	B1	3/2008	Stoev et al.
6,891,702	B1	5/2005	Tang	7,342,752	B1	3/2008	Zhang et al.
6,894,871	B2	5/2005	Alfoqaha et al.	7,349,170	B1	3/2008	Rudman et al.
6,894,877	B1	5/2005	Crue, Jr. et al.	7,349,179	B1	3/2008	He et al.
6,906,894	B2	6/2005	Chen et al.	7,354,664	B1	4/2008	Jiang et al.
6,909,578	B1	6/2005	Missell et al.	7,363,697	B1	4/2008	Dunn et al.
6,912,106	B1	6/2005	Chen et al.	7,371,152	B1	5/2008	Newman
6,934,113	B1	8/2005	Chen	7,372,665	B1	5/2008	Stoev et al.
6,934,129	B1	8/2005	Zhang et al.	7,375,926	B1	5/2008	Stoev et al.
6,940,688	B2	9/2005	Jiang et al.	7,379,269	B1	5/2008	Krounbi et al.
6,942,824	B1	9/2005	Li	7,386,933	B1	6/2008	Krounbi et al.
6,943,993	B2	9/2005	Chang et al.	7,389,577	B1	6/2008	Shang et al.
6,944,938	B1	9/2005	Crue, Jr. et al.	7,417,832	B1	8/2008	Erickson et al.
6,947,258	B1	9/2005	Li	7,419,891	B1	9/2008	Chen et al.
6,950,266	B1	9/2005	McCaslin et al.	7,428,124	B1	9/2008	Song et al.
6,954,332	B1	10/2005	Hong et al.	7,430,098	B1	9/2008	Song et al.
6,958,885	B1	10/2005	Chen et al.	7,436,620	B1	10/2008	Kang et al.
6,961,221	B1	11/2005	Niu et al.	7,436,638	B1	10/2008	Pan
6,969,989	B1	11/2005	Mei	7,440,220	B1	10/2008	Kang et al.
6,975,486	B2	12/2005	Chen et al.	7,443,632	B1	10/2008	Stoev et al.
6,987,643	B1	1/2006	Seagle	7,444,740	B1	11/2008	Chung et al.
6,989,962	B1	1/2006	Dong et al.	7,493,688	B1	2/2009	Wang et al.
6,989,972	B1	1/2006	Stoev et al.	7,508,627	B1	3/2009	Zhang et al.
7,006,327	B2	2/2006	Krounbi et al.	7,522,377	B1	4/2009	Jiang et al.
7,007,372	B1	3/2006	Chen et al.	7,522,379	B1	4/2009	Krounbi et al.
7,012,832	B1	3/2006	Sin et al.	7,522,382	B1	4/2009	Pan
7,023,658	B1	4/2006	Knapp et al.	7,542,246	B1	6/2009	Song et al.
7,026,063	B2	4/2006	Ueno et al.	7,551,406	B1	6/2009	Thomas et al.
7,027,268	B1	4/2006	Zhu et al.	7,552,523	B1	6/2009	He et al.
				7,554,767	B1	6/2009	Hu et al.
				7,564,658	B2	7/2009	Zhang et al.
				7,583,466	B2	9/2009	Kermiche et al.
				7,583,481	B2	9/2009	Zhang et al.

(56)

References Cited

U.S. PATENT DOCUMENTS

7,595,967 B1	9/2009	Moon et al.	8,196,285 B1	6/2012	Zhang et al.
7,639,457 B1	12/2009	Chen et al.	8,200,054 B1	6/2012	Li et al.
7,660,080 B1	2/2010	Liu et al.	8,203,800 B2	6/2012	Li et al.
7,672,080 B1	3/2010	Tang et al.	8,208,350 B1	6/2012	Hu et al.
7,672,086 B1	3/2010	Jiang	8,220,140 B1	7/2012	Wang et al.
7,684,160 B1	3/2010	Erickson et al.	8,222,599 B1	7/2012	Chien
7,688,546 B1	3/2010	Bai et al.	8,225,488 B1	7/2012	Zhang et al.
7,691,434 B1	4/2010	Zhang et al.	8,227,023 B1	7/2012	Liu et al.
7,695,761 B1	4/2010	Shen et al.	8,228,633 B1	7/2012	Tran et al.
7,719,795 B2	5/2010	Hu et al.	8,231,796 B1	7/2012	Li et al.
7,726,009 B1	6/2010	Liu et al.	8,233,248 B1	7/2012	Li et al.
7,729,086 B1	6/2010	Song et al.	8,248,896 B1	8/2012	Yuan et al.
7,729,087 B1	6/2010	Stoev et al.	8,254,060 B1	8/2012	Shi et al.
7,736,823 B1	6/2010	Wang et al.	8,257,597 B1	9/2012	Guan et al.
7,785,666 B1	8/2010	Sun et al.	8,259,410 B1	9/2012	Bai et al.
7,796,356 B1	9/2010	Fowler et al.	8,259,539 B1	9/2012	Hu et al.
7,800,858 B1	9/2010	Bajikar et al.	8,262,918 B1	9/2012	Li et al.
7,819,979 B1	10/2010	Chen et al.	8,262,919 B1	9/2012	Luo et al.
7,829,264 B1	11/2010	Wang et al.	8,264,797 B2	9/2012	Emley
7,846,643 B1	12/2010	Sun et al.	8,264,798 B1	9/2012	Guan et al.
7,855,854 B2	12/2010	Hu et al.	8,270,126 B1	9/2012	Roy et al.
7,869,160 B1	1/2011	Pan et al.	8,276,258 B1	10/2012	Tran et al.
7,872,824 B1	1/2011	Macchioni et al.	8,277,669 B1	10/2012	Chen et al.
7,872,833 B2	1/2011	Hu et al.	8,279,719 B1	10/2012	Hu et al.
7,910,267 B1	3/2011	Zeng et al.	8,284,517 B1	10/2012	Sun et al.
7,911,735 B1	3/2011	Sin et al.	8,288,204 B1	10/2012	Wang et al.
7,911,737 B1	3/2011	Jiang et al.	8,289,821 B1	10/2012	Huber
7,916,426 B2	3/2011	Hu et al.	8,291,743 B1	10/2012	Shi et al.
7,918,013 B1	4/2011	Dunn et al.	8,307,539 B1	11/2012	Rudy et al.
7,968,219 B1	6/2011	Jiang et al.	8,307,540 B1	11/2012	Tran et al.
7,973,349 B2	7/2011	Huai et al.	8,308,921 B1	11/2012	Hiner et al.
7,978,439 B2	7/2011	Zhang et al.	8,310,785 B1	11/2012	Zhang et al.
7,982,989 B1	7/2011	Shi et al.	8,310,901 B1	11/2012	Batra et al.
8,008,912 B1	8/2011	Shang	8,315,019 B1	11/2012	Mao et al.
8,012,316 B2	9/2011	Zhang et al.	8,316,527 B2	11/2012	Hong et al.
8,012,804 B1	9/2011	Wang et al.	8,320,076 B1	11/2012	Shen et al.
8,015,692 B1	9/2011	Zhang et al.	8,320,077 B1	11/2012	Tang et al.
8,018,677 B1	9/2011	Chung et al.	8,320,219 B1	11/2012	Wolf et al.
8,018,678 B1	9/2011	Zhang et al.	8,320,220 B1	11/2012	Yuan et al.
8,024,748 B1	9/2011	Moravcc et al.	8,320,722 B1	11/2012	Yuan et al.
8,072,705 B1	12/2011	Wang et al.	8,322,022 B1	12/2012	Yi et al.
8,074,345 B1	12/2011	Anguelouch et al.	8,322,023 B1	12/2012	Zeng et al.
8,077,418 B1	12/2011	Hu et al.	8,325,569 B1	12/2012	Shi et al.
8,077,434 B1	12/2011	Shen et al.	8,333,008 B1	12/2012	Sin et al.
8,077,435 B1	12/2011	Liu et al.	8,334,093 B2	12/2012	Zhang et al.
8,077,557 B1	12/2011	Hu et al.	8,336,194 B2	12/2012	Yuan et al.
8,079,135 B1	12/2011	Shen et al.	8,339,738 B1	12/2012	Tran et al.
8,081,403 B1	12/2011	Chen et al.	8,339,754 B2	12/2012	Zhang et al.
8,091,210 B1	1/2012	Sasaki et al.	8,341,826 B1	1/2013	Jiang et al.
8,097,846 B1	1/2012	Anguelouch et al.	8,343,319 B1	1/2013	Li et al.
8,104,166 B1	1/2012	Zhang et al.	8,343,364 B1	1/2013	Gao et al.
8,116,043 B2	2/2012	Leng et al.	8,349,195 B1	1/2013	Si et al.
8,116,171 B1	2/2012	Lee	8,351,307 B1	1/2013	Wolf et al.
8,125,856 B1	2/2012	Li et al.	8,357,244 B1	1/2013	Zhao et al.
8,134,794 B1	3/2012	Wang	8,373,945 B1	2/2013	Luo et al.
8,136,224 B1	3/2012	Sun et al.	8,375,564 B1	2/2013	Luo et al.
8,136,225 B1	3/2012	Zhang et al.	8,375,565 B2	2/2013	Hu et al.
8,136,805 B1	3/2012	Lee	8,379,351 B2*	2/2013	Fuji B82Y 10:00 360/324.1
8,141,235 B1	3/2012	Zhang	8,381,391 B2	2/2013	Park et al.
8,146,236 B1	4/2012	Luo et al.	8,385,027 B2	2/2013	Zhao et al.
8,149,536 B1	4/2012	Yang et al.	8,385,157 B1	2/2013	Champion et al.
8,151,441 B1	4/2012	Rudy et al.	8,385,158 B1	2/2013	Hu et al.
8,163,185 B1	4/2012	Sun et al.	8,394,280 B1	3/2013	Wan et al.
8,164,760 B2	4/2012	Willis	8,400,731 B1	3/2013	Li et al.
8,164,855 B1	4/2012	Gibbons et al.	8,404,128 B1	3/2013	Zhang et al.
8,164,864 B2	4/2012	Kaiser et al.	8,404,129 B1	3/2013	Luo et al.
8,165,709 B1	4/2012	Rudy	8,405,930 B1	3/2013	Li et al.
8,166,631 B1	5/2012	Tran et al.	8,409,453 B1	4/2013	Jiang et al.
8,166,632 B1	5/2012	Zhang et al.	8,413,317 B1	4/2013	Wan et al.
8,169,473 B1	5/2012	Yu et al.	8,416,540 B1	4/2013	Li et al.
8,171,618 B1	5/2012	Wang et al.	8,419,953 B1	4/2013	Su et al.
8,179,636 B1	5/2012	Bai et al.	8,419,954 B1	4/2013	Chen et al.
8,191,237 B1	6/2012	Luo et al.	8,422,176 B1	4/2013	Leng et al.
8,194,365 B1	6/2012	Leng et al.	8,422,342 B1	4/2013	Lee
8,194,366 B1	6/2012	Li et al.	8,422,841 B1	4/2013	Shi et al.
			8,424,192 B1	4/2013	Yang et al.
			8,441,756 B1	5/2013	Sun et al.
			8,443,510 B1	5/2013	Shi et al.

(56)		References Cited			
U.S. PATENT DOCUMENTS					
8,444,866	B1	5/2013	Guan et al.	8,665,561	B1
8,449,948	B2	5/2013	Medina et al.	8,670,211	B1
8,451,556	B1	5/2013	Wang et al.	8,670,213	B1
8,451,563	B1	5/2013	Zhang et al.	8,670,214	B1
8,454,846	B1	6/2013	Zhou et al.	8,670,294	B1
8,455,119	B1	6/2013	Jiang et al.	8,670,295	B1
8,456,961	B1	6/2013	Wang et al.	8,675,316	B2*
8,456,963	B1	6/2013	Hu et al.		
8,456,964	B1	6/2013	Yuan et al.	8,675,318	B1
8,456,966	B1	6/2013	Shi et al.	8,675,455	B1
8,456,967	B1	6/2013	Mallary	8,681,594	B1
8,458,892	B2	6/2013	Si et al.	8,689,430	B1
8,462,592	B1	6/2013	Wolf et al.	8,693,141	B1
8,468,682	B1	6/2013	Zhang	8,703,397	B1
8,472,288	B1	6/2013	Wolf et al.	8,705,205	B1
8,480,911	B1	7/2013	Osugi et al.	8,711,518	B1
8,486,285	B2	7/2013	Zhou et al.	8,711,528	B1
8,486,286	B1	7/2013	Gao et al.	8,717,709	B1
8,488,272	B1	7/2013	Tran et al.	8,720,044	B1
8,491,801	B1	7/2013	Tanner et al.	8,721,902	B1
8,491,802	B1	7/2013	Gao et al.	8,724,259	B1
8,493,693	B1	7/2013	Zheng et al.	8,749,790	B1
8,493,695	B1	7/2013	Kaiser et al.	8,749,920	B1
8,495,813	B1	7/2013	Hu et al.	8,753,903	B1
8,498,084	B1	7/2013	Leng et al.	8,755,152	B1*
8,506,828	B1	8/2013	Osugi et al.		
8,514,517	B1	8/2013	Batra et al.	8,760,807	B1
8,518,279	B1	8/2013	Wang et al.	8,760,818	B1
8,518,832	B1	8/2013	Yang et al.	8,760,819	B1
8,520,336	B1	8/2013	Liu et al.	8,760,822	B1
8,520,337	B1	8/2013	Liu et al.	8,760,823	B1
8,524,068	B2	9/2013	Medina et al.	8,763,235	B1
8,526,275	B1	9/2013	Yuan et al.	8,780,498	B1
8,531,801	B1	9/2013	Xiao et al.	8,780,505	B1
8,532,450	B1	9/2013	Wang et al.	8,786,983	B1
8,533,937	B1	9/2013	Wang et al.	8,790,524	B1
8,537,494	B1	9/2013	Pan et al.	8,790,527	B1
8,537,495	B1	9/2013	Luo et al.	8,792,208	B1
8,537,502	B1	9/2013	Park et al.	8,792,312	B1
8,545,999	B1	10/2013	Leng et al.	8,793,866	B1
8,547,659	B1	10/2013	Bai et al.	8,797,680	B1
8,547,667	B1	10/2013	Roy et al.	8,797,684	B1
8,547,730	B1	10/2013	Shen et al.	8,797,686	B1
8,555,486	B1	10/2013	Medina et al.	8,797,692	B1
8,559,141	B1	10/2013	Pakala et al.	8,813,324	B2
8,563,146	B1	10/2013	Zhang et al.	9,121,886	B2*
8,565,049	B1	10/2013	Tanner et al.	2002/0131215	A1*
8,570,691	B2*	10/2013	Sato	2003/0168673	A1*
				2006/0061915	A1*
8,576,517	B1	11/2013	Tran et al.	2007/0076331	A1*
8,578,594	B2	11/2013	Jiang et al.	2008/0316657	A1*
8,582,238	B1	11/2013	Liu et al.	2009/0168270	A1*
8,582,241	B1	11/2013	Yu et al.	2009/0213503	A1*
8,582,253	B1	11/2013	Zheng et al.	2009/0257152	A1*
8,588,039	B1	11/2013	Shi et al.	2010/0290157	A1
8,593,914	B2	11/2013	Wang et al.	2011/0086240	A1
8,597,528	B1	12/2013	Roy et al.	2012/0111826	A1
8,599,520	B1	12/2013	Liu et al.	2012/0216378	A1
8,599,657	B1	12/2013	Lee	2012/0237878	A1
8,603,593	B1	12/2013	Roy et al.	2012/0257298	A1*
8,607,438	B1	12/2013	Gao et al.		
8,607,439	B1	12/2013	Wang et al.	2012/0298621	A1
8,611,035	B1	12/2013	Bajikar et al.	2013/0216702	A1
8,611,054	B1	12/2013	Shang et al.	2013/0216863	A1
8,611,055	B1	12/2013	Pakala et al.	2013/0257421	A1
8,614,864	B1	12/2013	Hong et al.	2014/0154529	A1
8,619,512	B1	12/2013	Yuan et al.	2014/0175050	A1
8,625,233	B1	1/2014	Ji et al.		
8,625,941	B1	1/2014	Shi et al.		
8,628,672	B1	1/2014	Si et al.		
8,630,068	B1	1/2014	Mauri et al.		
8,634,280	B1	1/2014	Wang et al.		
8,638,529	B1	1/2014	Leng et al.		
8,643,980	B1	2/2014	Fowler et al.		
8,649,123	B1	2/2014	Zhang et al.		
				3/2014	Knutson et al.
				3/2014	Sun et al.
				3/2014	Zeng et al.
				3/2014	Knutson et al.
				3/2014	Shi et al.
				3/2014	Hu et al.
				3/2014	Lee
					B82Y 10/00
					360/324.11
				3/2014	Ito et al.
				3/2014	Krichevsky et al.
				3/2014	Shi et al.
				4/2014	Chen et al.
				4/2014	Elliott et al.
				4/2014	Zeng et al.
				4/2014	Li et al.
				4/2014	Zeng et al.
				4/2014	Xiao et al.
				5/2014	Shi et al.
				5/2014	Tran et al.
				5/2014	Wang et al.
				5/2014	Liu et al.
				6/2014	Tanner et al.
				6/2014	Knutson et al.
				6/2014	Tanner et al.
				6/2014	Park
					G01R 33/093
					360/319
				6/2014	Zhang et al.
				6/2014	Diao et al.
				6/2014	Liu et al.
				6/2014	Li et al.
				6/2014	Chen et al.
				7/2014	Wang et al.
				7/2014	Jiang et al.
				7/2014	Xiao
				7/2014	Liu et al.
				7/2014	Luo et al.
				7/2014	Luo et al.
				7/2014	Liu et al.
				7/2014	Wang et al.
				8/2014	Zhang et al.
				8/2014	Luo et al.
				8/2014	Tran et al.
				8/2014	Bai et al.
				8/2014	Guo et al.
				8/2014	Emley et al.
				9/2015	Singleton
					G01R 33/09
				9/2002	Beach
					B82Y 10/00
					360/324.2
				9/2003	Yuasa
					B82Y 10/00
					257/200
				3/2006	Zhang
					B82Y 10/00
					360/324.11
				4/2007	Pinarbasi
					B82Y 10/00
					360/324.11
				12/2008	Zhang
					B82Y 10/00
					360/324.11
				7/2009	Takahashi
					B82Y 25/00
					360/324.11
				8/2009	Sun
					B82Y 10/00
					360/324.2
				10/2009	Lee
					B82Y 10/00
					360/324.11
				11/2010	Zhang et al.
				4/2011	Xiang et al.
				5/2012	Chen et al.
				8/2012	Emley et al.
				9/2012	Zeng et al.
				10/2012	Sato
					G11B 5/3909
					360/75
				11/2012	Gao
				8/2013	Kaiser et al.
				8/2013	Li et al.
				10/2013	Shang et al.
				6/2014	Yang et al.
				6/2014	Zhang et al.

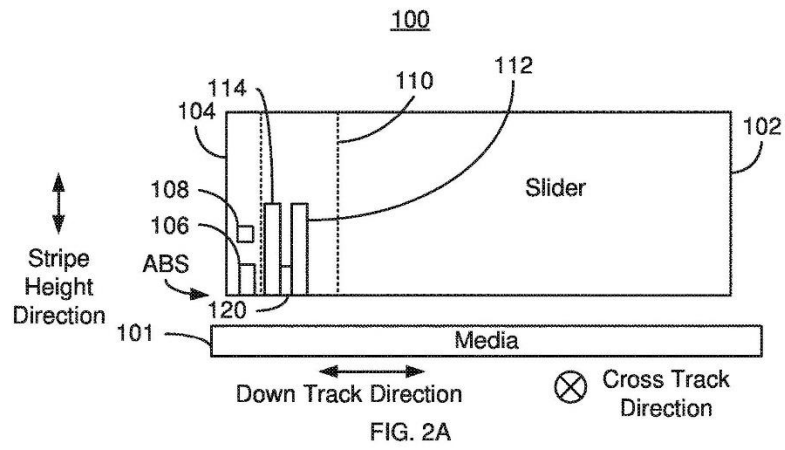
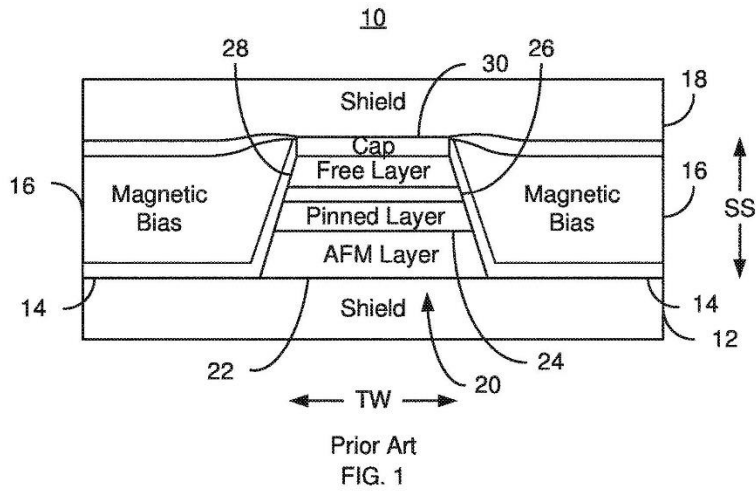
(56)

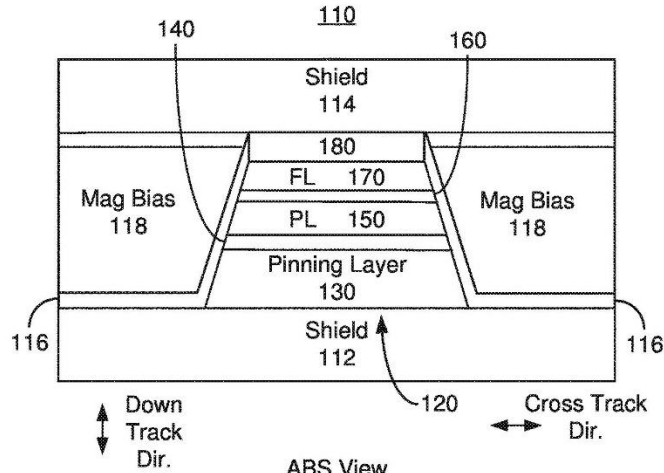
References Cited

U.S. PATENT DOCUMENTS

2014/0334032	A1*	11/2014	Nishioka	G11B 5/127
					360/75
2015/0332714	A1*	11/2015	Singleton	G01R 33/09
					360/319
2016/0197146	A1*	7/2016	Augusto	H01L 29/68
					257/22

* cited by examiner





ABS View
FIG. 2B

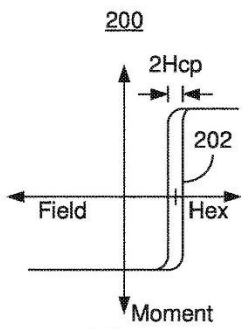


FIG. 3A

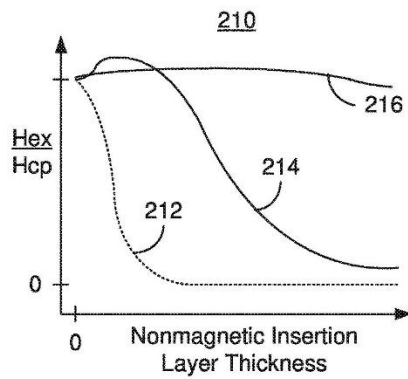


FIG. 3B

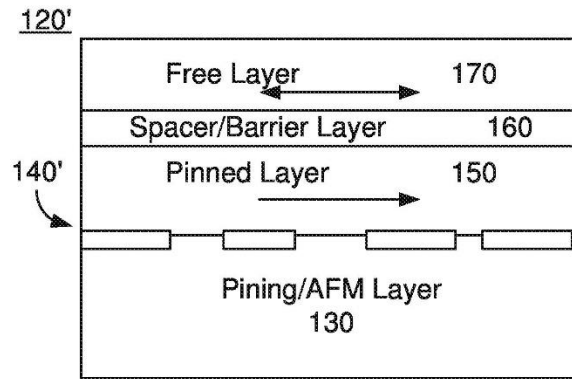


FIG. 4

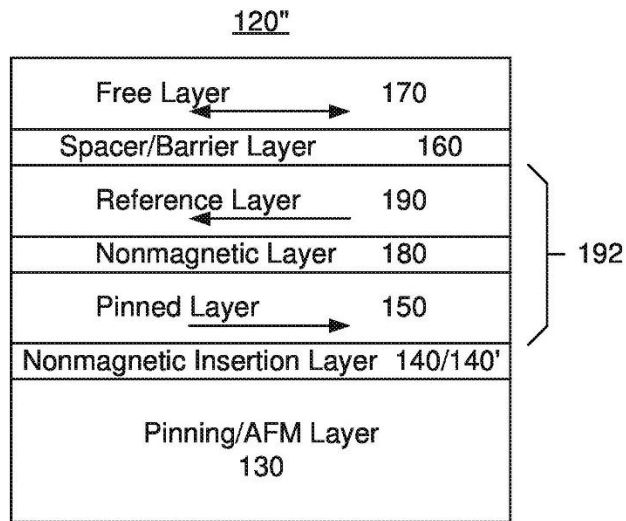


FIG. 5

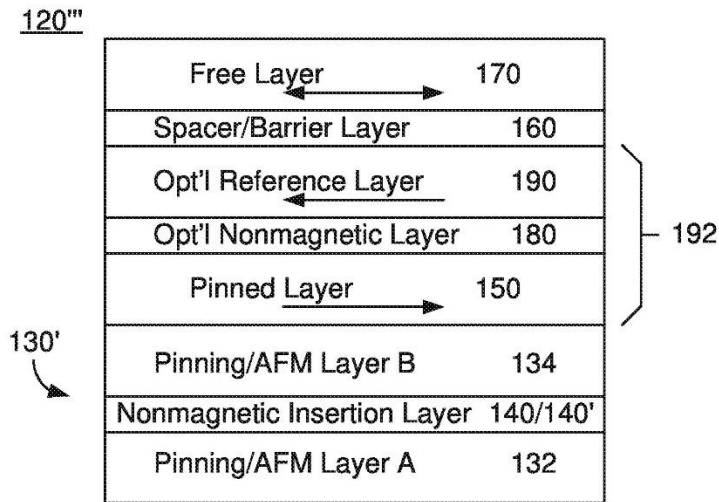


FIG. 6

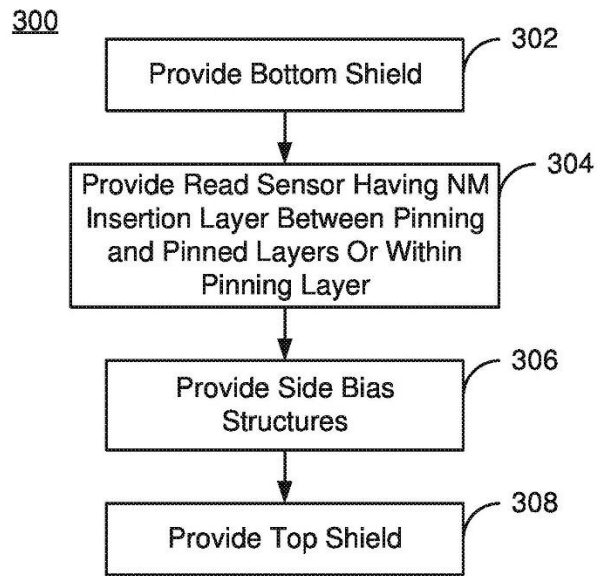


FIG. 7

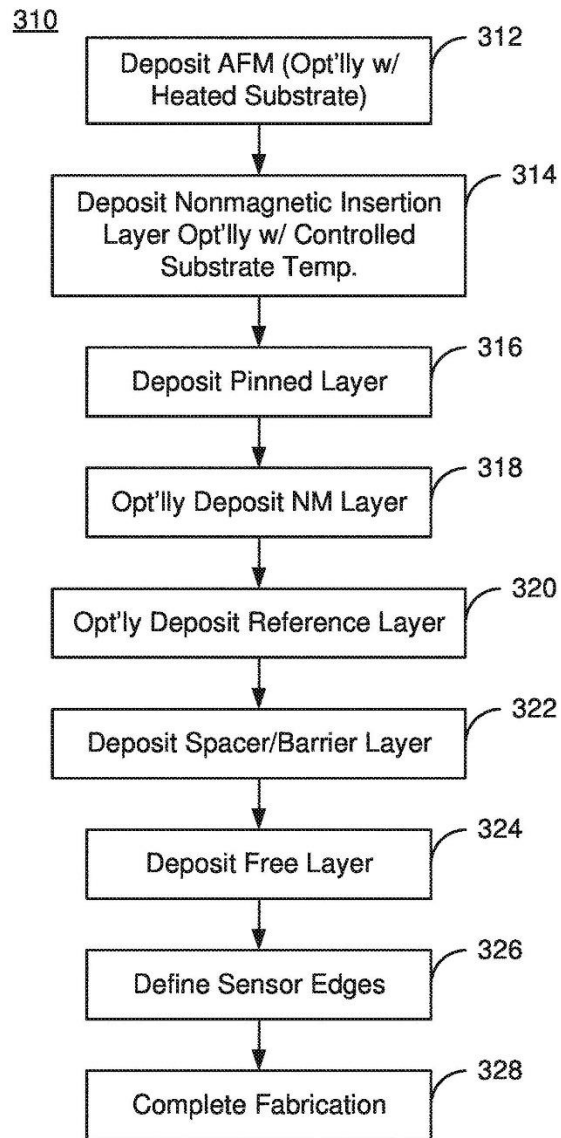


FIG. 8

1
**MAGNETIC READER HAVING A
 NONMAGNETIC INSERTION LAYER FOR
 THE PINNING LAYER**

BACKGROUND

FIG. 1 depicts an air-bearing surface (ABS) view of a conventional read transducer used in magnetic recording technology applications. The conventional read transducer 10 includes shields 12 and 18, insulator 14, magnetic bias structures 16, and sensor 20. The read sensor 20 is typically a giant magnetoresistive (GMR) sensor or tunneling magnetoresistive (TMR) sensor. The read sensor 20 includes an antiferromagnetic (AFM) layer 22, a pinned layer 24, a nonmagnetic spacer layer 26, and a free layer 28. Also shown is a capping layer 30. In addition, seed layer(s) may be used. The free layer 28 has a magnetization sensitive to an external magnetic field. Thus, the free layer 28 functions as a sensor layer for the magnetoresistive sensor 20. If the sensor 20 is to be used in a current perpendicular to plane (CPP) configuration, then current is driven in a direction substantially perpendicular to the plane of the layers 22, 24, 26, and 28. Conversely, in a current-in-plane (CIP) configuration, then current is driven in a direction parallel to the plane of the layers 22, 24, 26, and 28. The magnetic bias structures 16 are used to magnetically bias the free layer 28. The pinned layer 26 adjoins, or shares an interface, with the AFM layer 22. This allows for the pinned layer 26 magnetic moment to be exchange coupled with the magnetic moments AFM layer 22. Consequently, the pinned layer magnetic moment is fixed, or pinned, using the AFM layer 22.

Although the conventional transducer 10 functions, there are drawbacks. In particular, the read sensor 20 may be subject to noise. For example, there may be instabilities in the orientation of the pinned layer magnetic moment with respect to the free layer magnetic moment. The conventional read sensor 20 may not thus adequately read high density media.

BRIEF DESCRIPTION OF SEVERAL VIEWS OF
 THE DRAWINGS

FIG. 1 depicts an ABS view of a conventional magnetic recording read transducer.

FIGS. 2A-2B depict side and ABS views of an exemplary embodiment of a portion of a magnetic read apparatus.

FIG. 3A-3B are graphs depicting the magnetic moment versus field and the ratio of the exchange field to the coercivity of the pinned layer versus thickness of the magnetic insertion layer.

FIG. 4 depicts another exemplary embodiment of a portion of a magnetic read sensor.

FIG. 5 depicts another exemplary embodiment of a portion of a magnetic read sensor.

FIG. 6 depicts another exemplary embodiment of a portion of a magnetic read sensor.

FIG. 7 is flow chart depicting an exemplary embodiment of a method for providing a magnetic recording read apparatus.

FIG. 8 is flow chart depicting another exemplary embodiment of a method for providing a magnetic recording read transducer.

DETAILED DESCRIPTION OF THE
 PREFERRED EMBODIMENTS

FIGS. 2A-2B depict side and ABS views of an exemplary embodiment of a portion of a magnetic recording apparatus

2

100. For clarity, FIGS. 2A-2B are not to scale. Further, only a portion of the components of the magnetic apparatus 100 are depicted. The magnetic recording apparatus 100 depicted is a disk drive including media 101 and a slider 102 having a writer 104 and a read transducer 110 fabricated thereon. The write transducer 104 includes at least a write pole 106 and coil(s) 108 for energizing the pole 106. The write transducer 104 may be a perpendicular magnetic recording (PMR) writer, a heat assisted magnetic recording (HAMR) writer or another writer. In other embodiments, the write transducer 104 might be omitted.

The read transducer 110 includes a read sensor 120 and may include soft magnetic shields 112 and 114. The shields 112 and 114 may be formed of NiFe or another soft magnetic material. The read transducer 110 may also include insulating layer 116 and magnetic bias structures 118. The insulating layer 116 separates the magnetic bias structures 118 from the read sensor 120 and, in the embodiment shown, from the shield 112. The magnetic bias structures 118 may be soft magnetic bias structures, hard magnetic bias structures and/or other magnetic bias structures. In other embodiments, other structures may be included and/or structures 112, 114, 116 and/or 118 may be omitted.

The read sensor 120 includes at least a pinning layer 130, a nonmagnetic insertion layer 140 and a pinned layer 150. In the embodiment shown, the read sensor 120 also includes a nonmagnetic spacer layer 160 and a free layer 170. The nonmagnetic spacer layer may be a conductor, such as Cu, or an insulating tunneling barrier layer, such as crystalline MgO. Thus, the sensor 120 may be a GMR sensor or a TMR sensor.

The pinning layer 130 is used to fix, or pin, the magnetic moment of the pinned layer 150. The pinning layer 130 may thus be an antiferromagnetic (AFM) layer 130. For example, the pinning layer 130 might be an IrMn layer, a PtMn layer, an FeMn layer or an analogous structure. The pinned layer 150 is ferromagnetic and may include sublayers that are magnetic and/or nonmagnetic. Note that in some embodiments, a nonmagnetic layer (not shown) and a ferromagnetic layer (not shown) may be between the pinned layer 150 and the nonmagnetic spacer layer 160. In some such embodiments, the magnetic moments of the pinned layer 150 and the additional ferromagnetic layer may be antiferromagnetically coupled through the nonmagnetic layer. Thus, the pinned layer 150 may be part of a structure such as a synthetic antiferromagnetic (SAF) structure.

The nonmagnetic insertion layer 140 has a location selected from a first location and a second location. The first location, shown in the embodiment depicted in FIG. 2B, is between the pinning layer 130 and the pinned layer 150. In some embodiments, the nonmagnetic insertion layer 140 adjoins both the pinning layer 130 and the pinned layer 150. Thus, the nonmagnetic insertion layer 140 may share one interface with the pinning layer 130 and the opposite interface with the pinned layer 150. The second location is within the pinning layer 130. In an alternate embodiment, multiple nonmagnetic insertion layers could be included. In such an embodiment, one insertion layer would be in the first location (between the layers 130 and 150) and another insertion layer would be in the second location (within the layer 150). In some embodiments, the nonmagnetic insertion layer 140 includes at least one of Ag, Mg, Mn, Ir, Pt, Cr, Ti, Si, C, Al, Ru and Au. In some such embodiments, the nonmagnetic insertion layer 140 consists of Ag, Mg, Mn, Ir, Pt, Cr, Ti, Si, C, Al, Ru and/or Au. The nonmagnetic insertion layer 140 may also be desired to be thin. In some embodiments, therefore, the thickness of the nonmagnetic insertion layer

140 may be at least one Angstrom and not more than five Angstroms in some embodiments. For example, the thickness of the nonmagnetic insertion layer 140 may be at least one Angstroms and not more than three Angstroms. The nonmagnetic insertion layer 140 may thus be a dusting layer. In some embodiments, the nonmagnetic insertion layer 140 may be discontinuous.

The nonmagnetic insertion layer 140 is configured to affect the magnetic coupling between the pinning layer 130 and the pinned layer 150. This effect may be seen in FIGS. 3A-3B. FIGS. 3A and 3B are graphs 200 and 210, respectively, depicting the magnetic moment versus field for the pinned layer 150 and the ratio of the exchange field to the coercivity versus the thickness of the insertion layer 140. FIGS. 3A-3B are not to scale and are for explanatory purposes only. Thus, actual data is not meant to be represented in the graphs 200 and 210.

As can be seen in FIG. 3A, the magnetic moment of the pinned layer 150 exhibits a hysteresis loop 202 with respect to magnetic field. The hysteresis loop 202 is shifted from being centered at a zero applied magnetic field because of the magnetic coupling between the pinning layer 130 and the pinned layer 150. The shift in the center of the hysteresis loop is the exchange field, Hex, due to the coupling between the pinning layer 130 and the pinned layer 150. The coercivity, Hcp, relates to the applied field which will cause the magnetic moment of the pinned layer 150 to go to zero as part of a transition from a positive moment to a negative moment or vice versa. Because the hysteresis loop is shifted, the coercivity is based on the width of the loop ($2^{\circ}H_{cp}$ =width of loop). The coercivity is a measure of the fraction of unstable grains in the pinning layer 130.

The ratio of the exchange field to the coercivity (Hex/Hcp) may be considered both a measure of the strength and stability of the magnetic coupling between the pinning layer 130 and the pinned layer 150 and a measure of the fraction of unstable grains in the pinning layer 130. As can be seen in the graph 210 of FIG. 3B, the use of the nonmagnetic insertion layer 140 changes this ratio. Curves 212, 214 and 216 depict the ratio Hex/Hcp versus insertion layer thickness for various materials. Note that a zero thickness for the nonmagnetic insertion layer 140 means that no nonmagnetic insertion material is present. Thus, the curves 212, 214 and 216 meet at a zero insertion layer thickness. Curve 212 is the generally expected result of adding the nonmagnetic insertion layer 140, particularly between the pinned layer 150 and the pinning layer 130. For the material corresponding to the curve 212, the presence of any nonmagnetic material reduces the exchange coupling. Such a curve is typical for the insertion of a nonmagnetic material between the layers 130 and 150. Thus, for most materials, the relationship between insertion layer thickness and Hex/Hcp would follow the curve 212. Curves 214 and 216, in contrast, indicate that the ratio of Hex to Hcp may actually increase for small thicknesses of certain materials. For some such materials, the exchange field may increase for small thicknesses (e.g. less than ten Angstroms) while the coercivity decreases or remains constant. Alternatively, the coercivity may decrease and the exchange field may be constant for the small thicknesses. Other combinations of possibilities result in a maximum in Hex/Hcp that occurs at a nonzero thickness of the nonmagnetic insertion layer 140. Thus, for appropriate selection of materials and location, Hex/Hcp increases or remains constant for nonzero insertion layer thicknesses. Materials such as Ag, Mg, Mn, Ir, Pt, Cr, Ti, Si, C, Al, Ru and/or Au used as the insertion layer allow for an increase (or constant) Hex/Hcp for the pinned layer 150 and pinning

layer 130 at small thicknesses of nonmagnetic insertion layer. For larger thicknesses of the nonmagnetic insertion layer 140, the magnetic coupling between the layers 130 and 150 decreases. Thus, the nonmagnetic insertion layer 140 is configured such that the Hex/Hcp for the pinned layer 150 has a maximum for a nonzero thickness of the insertion layer 140. Stated differently, the nonmagnetic insertion layer 140 is configured such that Hex/Hcp increases or remains constant for some small thicknesses of the nonmagnetic insertion layer 140.

It is believed that the nonmagnetic insertion layer 140 operates in the following manner. However, the benefits and use of the magnetic devices described herein are independent of a particular physical mechanism. Because the nonmagnetic insertion layer 140 is thin and may be made of particular materials, it is believed that the materials in the nonmagnetic insertion layer 140 migrate to the grain boundaries of the grains of the pinning layer 140 during fabrication. Thus, although depicted as a single layer, the nonmagnetic insertion layer 140 may be discontinuous or reside only in certain areas (e.g. grain boundaries at and near the interface of the pinning layer 130. The presence of the nonmagnetic insertion layer 140 at the grain boundaries of smaller, less stable grains may decouple these grains from the pinned layer 150. Thus, if the magnetic moment of the pinned layer 150 switches direction, the less stable grains of the pinning layer 130 may be less likely to change direction. Thus, these less stable grains are thus less likely to provide a magnetic bias in a direction opposite to the desired direction of magnetization. The pinned layer 150 magnetic moment may more readily return to the desired direction. The coercivity of the pinned layer 150 may thus be reduced. The stability of the magnetic moment of the pinned layer 150 may be enhanced. Stated differently, the coupling between the pinning layer 130 and the pinned layer 150 that pins the magnetic moment of the pinned layer 150 in the desired direction may be improved.

Regardless of the physical mechanism, the ratio of the exchange field and the coercivity may be improved. Consequently, the stability of the coupling between the pinned layer 150 and the pinning layer 130 may be enhanced. Noise due to instabilities in the magnetic moment of the pinned layer 130 may thus be removed. Performance of the magnetic device may thereby be improved.

FIG. 4 depicts another embodiment of a magnetic read sensor 120'. For clarity, FIG. 4 is not to scale. The read sensor 120' may be part of a read transducer and/or magnetic recording apparatus such as the read transducer 110 and magnetic recording apparatus 100. The transducer of which the read sensor 120' may be a part is part of a disk drive having a media, a slider and the head coupled with the slider. The read sensor 120' corresponds to the read sensor 120. Consequently, analogous components are labeled similarly. For example, the read sensor 120' includes a pinning/AFM layer 130, a nonmagnetic insertion layer 140', a pinned layer 150, a nonmagnetic spacer or tunneling barrier layer 160 and a free layer 170 that are analogous to the a pinning/AFM layer 130, the nonmagnetic insertion layer 140, the pinned layer 150, the nonmagnetic spacer or tunneling barrier layer 160 and the free layer 170 that are part of the read sensor 120 and thus part of the magnetic recording apparatus 100. Thus, the components 120', 130, 140', 150, 160 and 170 have a similar structure and function to the components 120, 130, 140, 150, 160 and 170, respectively, depicted in FIGS. 2A-2B. Thus, the nonmagnetic insertion layer 140' is configured such that Hex/Hcp increases or remains constant for some small thicknesses of the nonmagnetic insertion layer

5

140'. In some embodiments, the nonmagnetic insertion layer 140' includes at least one of Ag, Mg, Mn, Ir, Pt, Cr, Ti, Si, C, Al, Ru and Au. In some such embodiments, the nonmagnetic insertion layer 140' consists of Ag, Mg, Mn, Ir, Pt, Cr, Ti, Si, C, Al, Ru and/or Au. The nonmagnetic insertion layer 140' may also be desired to be thin. The nonmagnetic insertion layer 140' may have a thickness of not more than five Angstroms. In some such embodiments, the thickness of the nonmagnetic insertion layer 140' may be not more than three Angstroms. The nonmagnetic insertion layer 140' may also have a thickness of at least one Angstrom.

In the embodiment shown in FIG. 4, the nonmagnetic insertion layer 140' is explicitly discontinuous. In some embodiments, the nonmagnetic insertion layer 140' is at least one Angstrom thick. Other thicknesses are, however, possible. In the embodiment shown, the nonmagnetic insertion layer 140' is in the first location: between the pinned layer 150 and the pinning layer 130. Also in the embodiment shown, the nonmagnetic insertion layer 140' shares interfaces with the pinning layer 130 and an opposite interface with the pinned layer 150. Note that in some embodiments, the nonmagnetic insertion layer 140' may reside at the grain boundaries of the pinning layer 130. Thus, the top surface of the nonmagnetic insertion layer 140' may be substantially coplanar with the top surface of the pinning layer 130. The nonmagnetic insertion layer 140' is, however, still considered to be at the first location: between the pinned layer 150 and the pinning layer 130. In another embodiment, the nonmagnetic insertion layer 140' might be located within the pinning layer 130.

The read sensor 120' shares the benefits of the read sensor 120. The use of the nonmagnetic insertion layer 140' may allow for a maximum in the Hex/Hcp for nonzero thicknesses of the nonmagnetic insertion layer 140'. Thus, the coupling between the pinning layer 130 and pinned layer 150 may be improved. The improved stability in the coupling between the pinned layer 150 and the pinning layer 130 may reduce noise during operation of the read sensor 120'.

FIG. 5 depicts another embodiment of a magnetic read sensor 120". For clarity, FIG. 5 is not to scale. The read sensor 120" may be part of a read transducer and/or magnetic recording apparatus such as the read transducer 110 and magnetic recording apparatus 100. The transducer of which the read sensor 120" may be a part is part of a disk drive having a media, a slider and the head coupled with the slider. The read sensor 120" corresponds to the read sensor(s) 120 and/or 120'. Consequently, analogous components are labeled similarly. For example, the read sensor 120" includes a pinning/AFM layer 130, a nonmagnetic insertion layer 140/140', a pinned layer 150, a nonmagnetic spacer or tunneling barrier layer 160 and a free layer 170 that are analogous to the pinning/AFM layer 130, the nonmagnetic insertion layer 140/140', the pinned layer 150, the nonmagnetic spacer or tunneling barrier layer 160 and the free layer 170 that are part of the read sensor 120 and thus part of the magnetic recording apparatus 100. Thus, the components 120", 130, 140/140', 150, 160 and 170 have a similar structure and function to the components 120, 130, 140/140', 150, 160 and 170, respectively, depicted in FIGS. 2A-2B and 4. Thus, the nonmagnetic insertion layer 140/140' is configured such that Hex/Hcp increases or remains constant for some small thicknesses of the nonmagnetic insertion layer 140/140'. In some embodiments, the nonmagnetic insertion layer 140/140' includes at least one of Ag, Mg, Mn, Ir, Pt, Cr, Ti, Si, C, Al, Ru and Au. In some such embodiments, the nonmagnetic insertion layer 140/140' con-

6

sists of Ag, Mg, Mn, Ir, Pt, Cr, Ti, Si, C, Al, Ru and/or Au. The nonmagnetic insertion layer 140/140' may also be desired to be thin. The nonmagnetic insertion layer 140/140' may have a thickness of not more than five Angstroms. In some such embodiments, the thickness of the nonmagnetic insertion layer 140/140' may be not more than three Angstroms. The nonmagnetic insertion layer 140/140' may also have a thickness of at least one Angstrom.

In the embodiment shown in FIG. 5, the read sensor 120" includes a nonmagnetic layer 180 and a reference layer 190. The nonmagnetic layer 180 is conductive and may include a material such as Ru. The reference layer 190 is ferromagnetic and may include sublayers. The reference layer 190 and the pinned layer 150 are coupled through the nonmagnetic layer 180. For example, the coupling may be an RKKY coupling. Thus, the layers 150, 180 and 190 form a synthetic antiferromagnet (SAF).

The read sensor 120" shares the benefits of the read sensor(s) 120/120'. The use of the nonmagnetic insertion layer 140/140' may allow for a maximum in the Hex/Hcp for nonzero thicknesses of the nonmagnetic insertion layer 140/140'. Thus, the coupling between the pinning layer 130 and pinned layer 150 may be improved. The improved stability in the coupling between the pinned layer 150 and the pinning layer 130 may reduce noise during operation of the read sensor 120".

FIG. 6 depicts another embodiment of a magnetic read sensor 120". For clarity, FIG. 6 is not to scale. The read sensor 120" may be part of a read transducer and/or magnetic recording apparatus such as the read transducer 110 and magnetic recording apparatus 100. The transducer of which the read sensor 120" may be a part is part of a disk drive having a media, a slider and the head coupled with the slider. The read sensor 120" corresponds to the read sensor(s) 120, 120' and/or 120". Consequently, analogous components are labeled similarly. For example, the read sensor 120" includes a pinning/AFM layer 130', a nonmagnetic insertion layer 140/140', a pinned layer 150, a nonmagnetic spacer or tunneling barrier layer 160 and a free layer 170 that are analogous to the pinning/AFM layer 130, the nonmagnetic insertion layer 140/140', the pinned layer 150, the nonmagnetic spacer or tunneling barrier layer 160 and the free layer 170 that are part of the read sensor 120 and thus part of the magnetic recording apparatus 100. The read sensor 120" also may include optional reference layer 190 and optional nonmagnetic layer 180. The pinned layer 150', optional nonmagnetic spacer layer 180 and optional reference layer 190' may form an optional SAF 192.

Thus, the components 120", 130', 140/140', 150, 160, 170, 180, and 190 have a similar structure and function to the components 120/120'/120", 130, 140/140', 150, 160 and 170, respectively, depicted in FIGS. 2A-2B and 4. Thus, the nonmagnetic insertion layer 140/140' is configured such that Hex/Hcp increases or remains constant for some small thicknesses of the nonmagnetic insertion layer 140/140'. In some embodiments, the nonmagnetic insertion layer 140/140' includes at least one of Ag, Mg, Mn, Ir, Pt, Cr, Ti, Si, C, Al, Ru and/or Au. The nonmagnetic insertion layer 140/140' may also be desired to be thin. The nonmagnetic insertion layer 140/140' may have a thickness of not more than five Angstroms. In some such embodiments, the thickness of the nonmagnetic insertion layer 140/140' may be not more than three Angstroms. The nonmagnetic insertion layer 140/140' may also have a thickness of at least one Angstrom.

In the embodiment shown in FIG. 6, the nonmagnetic insertion layer 140/140' is explicitly within the pinning layer 130'. Thus the pinning layer 130' includes a pinning layer A 132 and a pinning layer 134 between which is the nonmagnetic insertion layer 140/140'. Although depicted as midway through the pinning layer 130', the nonmagnetic insertion layer 140/140' may reside elsewhere. For example, the nonmagnetic insertion layer 140/140' may be closer to the interface between the layers 130' and 150' than to the bottom surface of the pinning layer 130'. Further, even if the nonmagnetic insertion layer 140/140' is deposited in the middle of the AFM layer 130' as shown, the nonmagnetic insertion layer 140/140' may migrate during fabrication of the read sensor 120^m. Thus, the nonmagnetic insertion layer 140/140' may be closer to the pinned layer 150 and may or may not be continuous.

The read sensor 120^m shares the benefits of the read sensor(s) 120/120'/120'. The use of the nonmagnetic insertion layer 140/140' may allow for a maximum in the Hex/Hcp for nonzero thicknesses of the nonmagnetic insertion layer 140/140'. Thus, the coupling between the pinning layer 130' and pinned layer 150 may be improved. The improved stability in the coupling between the pinned layer 150 and the pinning layer 130' may reduce noise during operation of the read sensor 120^m.

The read sensors 120, 120', 120" and 120^m have been shown in various configurations to highlight particular features, such as differences in geometries. One of ordinary skill in the art will readily recognize that two or more of these features may be combined in various manners consistent with the method and system described herein that are not explicitly depicted in the drawings.

FIG. 7 is an exemplary embodiment of a method 300 for providing a read transducer. For simplicity, some steps may be omitted, interleaved, combined, have multiple substeps and/or performed in another order unless otherwise specified. The method 300 is described in the context of providing a magnetic recording apparatus 100, transducer 110 and read sensor 100. However, the method 300 may be used in fabricating the read sensor 120, 120', 120" and/or 120^m. The method 300 may be used to fabricate multiple magnetic read heads at substantially the same time. The method 300 may also be used to fabricate other magnetic recording transducers. The method 300 is also described in the context of particular layers. A particular layer may include multiple materials and/or multiple sub-layers. The method 300 is described in the context of a disk drive. However, the method may be used in other applications employing a magnetoresistive and bias structures. The method 300 also may start after formation of other portions of the magnetic recording transducer.

The bottom shield 112 is provided, via step 302. Step 302 may include depositing a magnetic material, such as NiFe and patterning the shield.

The read sensor 120 is provided, via step 304. Step 304 may include depositing a stack of layers for the read sensor 120 and defining the read sensor in the cross-track and stripe height directions. Further, the nonmagnetic insertion layer 140 is provided in the first or second location. Thus, the nonmagnetic insertion layer 140 may be placed between the pinned layer 150 and the pinning layer 140 or may be placed within the AFM. Thus, the read sensor 120, 120', 120" or 120^m may be provided.

The side bias structures 118 are provided, via step 306. Step 306 is performed after the read sensor 120 is defined in the cross-track direction. Thus, at least part of step 304 is performed before step 306. Step 306 may include depositing

the insulating layer 116, depositing the material(s) for the magnetic bias structures 118 and depositing a top nonmagnetic layer. A mill step and planarization, such as a chemical mechanical planarization (CMP) may also be performed.

The top shield 114 is provided, via step 308. Step 208 may include depositing, planarizing and patterning soft magnetic layer, such as a NiFe layer.

Using the method 300, the transducer 110 and the read sensor 120, 120', 120" and/or 120^m may be fabricated. Thus, the benefits of one or more of the read sensor 120, 120', 120" and/or 120^m may be achieved. Consequently, performance of the magnetic recording apparatus may be improved.

FIG. 8 is an exemplary embodiment of a method 310 for providing a read sensor such as the read sensor 120, 120', 120" and/or 120^m. For simplicity, some steps may be omitted, interleaved, combined, have multiple substeps and/or performed in another order unless otherwise specified. The method 310 is described in the context of providing a magnetic recording disk drive 100 and transducer 110. However, the method 310 may be used in fabricating another magnetic recording device. The method 310 may be used to fabricate multiple magnetic read sensors at substantially the same time. The method 310 is also described in the context of particular layers. A particular layer may include multiple materials and/or multiple sub-layers.

The pinning layer 130/130' is deposited, via step 312. Step 312 may include heating the substrate such that the materials for the pinning layer are deposited above the ambient temperature. For example, the IrMn or other AFM used for the pinning layer 130/130' may be deposited above room temperature.

The nonmagnetic insertion layer 140/140' is provided via step 314. Step 314 may include controlling the temperature of the substrate. Thus, the substrate may be heated such that the material(s) for the nonmagnetic insertion layer are deposited at a temperature above the ambient temperature. For example, the nonmagnetic insertion layer 140/140' may be sputtered above room temperature. In such embodiments, the atoms for the nonmagnetic insertion layer 140/140' may be more mobile. These atoms may more readily migrate, for example to grain boundaries of the pinning layer 130/130'. In other embodiments, step 314 may include cooling the substrate such that the nonmagnetic insertion layer 140/140' is deposited at temperatures below the ambient temperature. For example, the substrate may be cooled (e.g. via water cooling, liquid nitrogen cooling or physical connection to another heat sink) below the ambient temperature during deposition. For example, the material(s) for the nonmagnetic insertion layer 140/140' may be sputtered below room temperature. In such embodiments, the atoms for the nonmagnetic insertion layer may be less likely to migrate. In other embodiments, no attempt may be made to control the temperature of the substrate during deposition. Further, if the pinning layer 130' is used, then steps 312 and 314 are interleaved such that the nonmagnetic insertion layer 140/140' is deposited within the pinning layer 130'.

The pinned layer 150 is deposited, via step 316. Step 316 may include depositing multiple ferromagnetic layers. Nonmagnetic layer(s) may also be provided within the pinned layer. In some embodiments, the nonmagnetic layer 180 and reference layer 190 are deposited in steps 320 and 322, respectively.

The nonmagnetic spacer layer 160 is deposited, via step 322. For example, a conductive layer or tunneling barrier layer may be provided in step 322. The free layer 170 is deposited, via step 324. Step 324 may include depositing

9

multiple ferromagnetic layers. Nonmagnetic layer(s) may also be provided within the free layer 170.

The edges of the read sensor 120, 120', 120" and/or 120''' are defined, via step 324. Step 324 may include providing a mask on the read sensor stack deposited in the previous steps and ion milling the exposed regions. The read sensor 120, 120', 120" and/or 120''' may be defined in the cross-track and stripe height (perpendicular to the ABS) directions. Fabrication of the read sensor may then be completed. For example, anneals, capping layer depositing, and/or other processing steps may be performed.

Using the method 310, the read sensor(s) 120, 120', 120" and/or 120''' may be fabricated. Thus, the benefits of one or more of the read sensor(s) 120, 120', 120" and/or 120''' may be achieved.

We claim:

1. A magnetic apparatus comprising:
 - an element comprising a pinning layer, a nonmagnetic insertion layer, and a pinned layer, a location of the nonmagnetic insertion layer selected from a first location between the pinned layer and the pinning layer and a second location within the pinning layer, wherein, in the first location, a top surface of the nonmagnetic insertion layer is substantially coplanar with a top surface of the pinning layer, and wherein the nonmagnetic insertion layer adjoins the pinned layer and the pinning layer, the pinning layer being an antiferromagnetic (AFM) layer.
2. The magnetic apparatus of claim 1 wherein the element further comprises a nonmagnetic spacer layer and a free layer, the nonmagnetic spacer layer residing between the free layer and the pinned layer, the pinned layer being between the free layer and the pinning layer such that the free layer, the nonmagnetic spacer layer, the pinned layer and the pinning layer form a stack.
3. The magnetic apparatus of claim 1 wherein the nonmagnetic insertion layer comprises at least one of Ag, Mg, Mn, Ir, Pt, Cr, Ti, Si, C, Al, Ru and Au.
4. The magnetic apparatus of claim 1 wherein the nonmagnetic insertion layer has a thickness of not more than five Angstroms.
5. The magnetic apparatus of claim 4 wherein the nonmagnetic insertion layer has the thickness of not more than three Angstroms.
6. The magnetic apparatus of claim 4 wherein the nonmagnetic insertion layer has the thickness of at least one Angstrom.
7. The magnetic apparatus of claim 1 further comprising:
 - a bottom shield;
 - a top shield, the element residing between the bottom shield and the top shield; and
 - a side bias structure adjacent to at least one side surface of the element.
8. The magnetic apparatus of claim 1 wherein the nonmagnetic insertion layer is at the first location.
9. The magnetic apparatus of claim 8 wherein the nonmagnetic insertion layer adjoins the pinning layer and the pinned layer adjoins the nonmagnetic insertion layer.
10. The magnetic apparatus of claim 1 wherein the nonmagnetic insertion layer is configured such that a ratio of an exchange field to a coercivity for the pinned layer has a maximum at a nonzero thickness of the nonmagnetic insertion layer.
11. The magnetic apparatus of claim 1 wherein the nonmagnetic insertion layer excludes Mg and Al.

10

12. A magnetic apparatus comprising:
 - an element comprising a pinning layer, a nonmagnetic insertion layer, and a pinned layer, a location of the nonmagnetic insertion layer selected from a first location between the pinned layer and the pinning layer and a second location within the pinning layer, wherein the nonmagnetic insertion layer is a discontinuous layer.
13. A magnetic apparatus comprising:
 - an element comprising a pinning layer, a nonmagnetic insertion layer, and a pinned layer, the nonmagnetic insertion layer located between the pinned layer and the pinning layer, wherein a top surface of the nonmagnetic insertion layer is substantially coplanar with a top surface of the pinning layer, and wherein the nonmagnetic insertion layer adjoins the pinned layer and the pinning layer;
 - wherein the element further comprises a nonmagnetic layer and a reference layer, the nonmagnetic layer residing between the reference layer and the pinned layer, the reference layer having a reference layer magnetic moment, the pinned layer having a pinned layer magnetic moment, the reference layer magnetic moment being antiferromagnetically coupled with the pinned layer magnetic moment.
14. A disk drive comprising:
 - at least one disk;
 - at least one slider including at least one magnetic transducer comprising a bottom shield, a top shield, and an element between the bottom shield and the top shield, the element comprising an antiferromagnetic (AFM) layer, a nonmagnetic insertion layer, a pinned layer, a nonmagnetic layer, and a free layer, the nonmagnetic layer being between the pinned layer and the free layer, the nonmagnetic insertion layer having a location selected from a first location between the pinned layer and the pinning layer and a second location within the pinning layer, wherein the nonmagnetic insertion layer is a discontinuous layer.
15. The disk drive of claim 14 wherein the nonmagnetic insertion layer excludes Mg and Al.
16. A method for providing a magnetic apparatus comprising:
 - providing an element, wherein providing the element further comprises:
 - providing a pinning layer;
 - providing a nonmagnetic insertion layer; and
 - providing a pinned layer on the nonmagnetic insertion layer, wherein the nonmagnetic insertion layer is located between the pinned layer and the pinning layer such that a top surface of the nonmagnetic insertion layer is substantially coplanar with a top surface of the pinning layer and, wherein the nonmagnetic insertion layer adjoins the pinned layer and the pinning layer, the pinning layer being an antiferromagnetic (AFM) layer.
17. The method of claim 16 wherein the step of providing the element further comprises:
 - providing a nonmagnetic spacer layer; and
 - providing a free layer, the nonmagnetic spacer layer residing between the free layer and the pinned layer, the pinned layer being between the free layer and the pinning layer such that the free layer, the nonmagnetic spacer layer, the pinned layer and the pinning layer form a stack.

11

- 18. The method of claim 16 wherein the nonmagnetic insertion layer comprises at least one of Ag, Mg, Mn, Ir, Pt, Cr, Ti, Si, C, Al, Ru and Au.
- 19. The method of claim 16 wherein the nonmagnetic insertion layer has a thickness of at least one Angstrom.
- 20. The method of claim 16 wherein the step of providing the nonmagnetic insertion layer comprises:
depositing the nonmagnetic insertion layer on a heated substrate.
- 21. The method of claim 16 wherein the step of providing the nonmagnetic insertion layer comprises:
depositing the nonmagnetic insertion layer on a cooled substrate.
- 22. The method of claim 16 wherein the step of providing the pinning layer comprises:
depositing the pinning layer on a heated substrate.
- 23. The method of claim 16 wherein the step of providing the nonmagnetic insertion layer comprises:
depositing the nonmagnetic insertion layer directly on the pinning layer; and
wherein providing the pinned layer further comprises depositing the pinned layer directly on the nonmagnetic insertion layer.
- 24. The method of claim 16 wherein the nonmagnetic insertion layer is configured such that a ratio of an exchange field to a coercivity for the pinned layer has a maximum at a nonzero thickness of the nonmagnetic insertion layer.

12

- 25. The method of claim 16 wherein the nonmagnetic insertion layer excludes Mg and Al.
- 26. A magnetic apparatus comprising:
an element comprising a pinning layer, a nonmagnetic insertion layer, and a pinned layer, wherein the nonmagnetic insertion layer is located within the pinning layer.
- 27. A disk drive comprising:
at least one disk;
at least one slider comprising at least one magnetic transducer comprising a bottom shield, a top shield, and an element between the bottom shield and the top shield, the element comprising an antiferromagnetic (AFM) layer, a nonmagnetic insertion layer, a pinned layer, a nonmagnetic layer, and a free layer, the nonmagnetic insertion layer having a location within the pinning layer.
- 28. A method for providing a magnetic apparatus comprising:
providing an element, wherein providing the element further comprises:
providing a pinning layer;
providing a nonmagnetic insertion layer within the pinning layer; and
providing a pinned layer on the pinning layer.

* * * * *